

U.S. EPR Fuel Assembly - Faulted Condition Analysis

ANP-10325NP
Revision 0

Technical Report

May 2013

AREVA NP Inc.

(c) 2013 AREVA NP Inc.

Copyright © 2013

**AREVA NP Inc.
All Rights Reserved**

Nature of Changes

Item	Section(s) or Page(s)	Description and Justification
------	--------------------------	-------------------------------

Table of Contents

	<u>Page</u>
1.0 INTRODUCTION AND SUMMARY	1-1
2.0 U.S. EPR FUEL ASSEMBLY FEATURES, FUNCTIONAL REQUIREMENTS, AND ACCEPTANCE CRITERIA UNDER SEISMIC AND LOCA LOADS	2-1
2.1 U.S. EPR Fuel Assembly Features	2-1
2.2 U.S. EPR Fuel Assembly General Design Requirements	2-2
2.3 U.S. EPR Fuel Assembly Acceptance Criteria Under Seismic and LOCA Loads	2-4
2.3.1 Spacer Grid Acceptance Criteria	2-4
2.3.2 Non-Grid Structural Component Acceptance Criteria	2-5
3.0 U.S. EPR FUEL ASSEMBLY SEISMIC AND LOCA BOUNDARY CONDITIONS	3-1
3.1 U.S. EPR Seismic and LOCA Model Hierarchy	3-1
3.2 U.S. EPR Seismic and LOCA Loads	3-2
4.0 U.S. EPR FUEL ASSEMBLY METHODOLOGY FOR EVALUATION OF DYNAMIC RESPONSE, COMPONENT LOADS, AND STRESS ANALYSIS UNDER SEISMIC AND LOCA CONDITIONS	4-1
4.1 U.S. EPR Fuel Assembly Lateral Seismic and LOCA Methodology	4-2
4.1.1 U.S. EPR Fuel Assembly Lateral Model – Single Fuel Assembly in Free Vibration in Ambient Air	4-4
4.1.2 U.S. EPR Fuel Assembly Lateral Model – Hydrodynamic Coupling	4-39
4.1.3 U.S. EPR Fuel Assembly Lateral Model – Damping	4-42
4.1.4 U.S. EPR Fuel Assembly Lateral Model – Spacer Grid Dynamic Characteristics and Allowable Crushing Load	4-59
4.1.5 U.S. EPR Fuel Assembly Row Model – Seismic and LOCA Response Analysis Process	4-105
4.1.6 Analysis Software – The CASAC Code	4-116
4.2 U.S. EPR Vertical Seismic and LOCA Methodology	4-123
4.2.1 U.S. EPR Vertical Seismic and LOCA Model Architecture	4-125
4.2.2 U.S. EPR Vertical Model Design Verification Testing and Benchmarking	4-129

Table of Contents
(continued)

	<u>Page</u>
4.2.3 U.S. EPR Vertical Model – Augmentation and Conversion for Seismic and LOCA Analysis	4-135
4.3 U.S. EPR Seismic and LOCA Load Combination and Non-Grid Component Stress Analysis Methodology.....	4-137
4.3.1 Non-Linear 3D U.S. EPR Fuel Assembly Finite Element Model	4-139
4.3.2 U.S. EPR Fuel Assembly Load Combination Methodology	4-149
4.3.3 U.S. EPR Fuel Assembly Non-Grid Components Acceptance Criteria	4-153
5.0 INPUTS, FUEL ASSEMBLY RESPONSE, AND SPACER GRID IMPACTS FOR SEISMIC AND LOCA LATERAL LOADING	5-1
5.1 U.S. EPR Fuel Assembly Lateral Seismic and LOCA Analysis Inputs.....	5-1
5.2 U.S. EPR Fuel Assembly Lateral Seismic and LOCA Analysis – Results Summary	5-2
5.3 U.S. EPR Fuel Assembly Lateral Seismic and LOCA Analysis – Core Gap Sensitivity	5-7
6.0 INPUTS, FUEL ASSEMBLY RESPONSE, AND COMPONENT LOADS FOR SEISMIC AND LOCA VERTICAL LOADING	6-1
6.1 U.S. EPR Fuel Assembly Vertical Seismic and LOCA Analysis Inputs.....	6-1
6.2 U.S. EPR Fuel Assembly Vertical Seismic and LOCA Analysis – Results Summary	6-3
7.0 COMPONENT STRESS ANALYSIS UNDER COMBINED LOADING	7-1
7.1 U.S. EPR Guide Tube Faulted Loading Analysis	7-1
7.2 U.S. EPR Guide Tube Upper and Lower Connection Faulted Loading Analysis.....	7-3
7.3 U.S. EPR Guide Tube to Spacer Grid Connection Faulted Loading Analysis.....	7-4
7.4 U.S. EPR Top and Bottom Nozzle Faulted Loading Analysis	7-4
7.5 U.S. EPR Fuel Rod Faulted Loading Analysis	7-6
7.6 U.S. EPR Fuel Assembly Component Load Core Gap Sensitivity.....	7-8

Table of Contents

(continued)

	<u>Page</u>
8.0 REFERENCES	8-1
APPENDIX A : U.S. EPR SPACER GRID CHARACTERIZATION – DETAILED INFORMATION	A-1
APPENDIX B : U.S. EPR SEISMIC AND LOCA LOADS – LATERAL DISPLACEMENT INPUT TIME HISTORIES	B-1

List of Tables

	<u>Page</u>
Table 1-1—U.S. EPR Spacer Grid Impact Load Margins – All Frequency Sweep Cases.....	1-4
1-4	
Table 1-2—U.S. EPR Spacer Grid Limiting Impact Load Margins	1-4
Table 1-3—Frequency Sweep Cases w. Permanent Deformation over Manufacturing Tolerance	1-5
1-5	
Table 1-4—Non-Grid Component Strength Margins	1-5
Table 4-1—U.S. EPR Lateral Model Benchmark	4-24
Table 4-2—HTP-LX Features.....	4-25
Table 4-3—U.S. EPR Features	4-26
Table 4-4—Fuel Assembly Damping Sources.....	4-43
Table 4-5—M5 [®] Yield Strength Comparison	4-81
Table 4-6—U.S. EPR Spacer Grid Allowable Crushing Load Summary	4-93
Table 4-7—U.S. EPR Fuel Assembly Model - Hydrodynamic Coupling Matrix Terms.....	4-111
Table 4-8—U.S. EPR Fuel Assembly Model – Rayleigh Damping Coefficients	4-111
Table 4-9—U.S. EPR Rotational Spacer Grid Stiffness – Operating Temperature – All Frequency Sweep Cases	4-111
Table 4-10—U.S. EPR Fuel Assembly Frequencies (Hz) – Operating Temperature – All Frequency Sweep Cases	4-112
Table 4-11—U.S. EPR Grid Stiffness and Damping – Operating Temperature	4-115
Table 4-12—Comparison of CASAC Model and Test Impact Loads (in water)	4-123
Table 4-13—Model and Actual Fuel Weights	4-132
Table 4-14—Guide Tube and Fuel Rod Properties	4-132
Table 4-15—Gap Element Properties	4-133
Table 4-16—Top and Bottom Nozzle Properties	4-133
Table 4-17—Spacer Grid Properties	4-133
Table 4-18—Drop Test Benchmarking Summary.....	4-134
Table 4-19—Hold-down Spring Properties.....	4-136
Table 4-20—Young’s Modulus Values	4-136

List of Tables
(continued)

	<u>Page</u>
Table 4-21—Displaced Water Mass.....	4-136
Table 4-22—Added and Coupling Masses on Guide Tube and Fuel Rod Nodes	4-137
Table 4-23—HTP-LX Model Structural Parameters	4-146
Table 4-24—U.S. EPR Model Structural Parameters.....	4-147
Table 4-25—Limiting Cases of Seismic and LOCA Loading – Unirradiated Condition.....	4-151
Table 4-26—Limiting Cases of Seismic and LOCA Loading – Irradiated Condition .	4-152
Table 5-1—U.S. EPR Spacer Grid Impact Load Margins – All Frequency Sweep Cases.....	5-3
5-3	
Table 5-2—U.S. EPR Spacer Grid Limiting Impact Load Margins	5-3
Table 5-3—U.S. EPR End Fitting Limiting Bending Moments	5-4
Table 5-4—Frequency Sweep Cases with Permanent Deformation over Manufacturing Tolerance	5-5
Table 5-5—Gap Sensitivity Study Results.....	5-8
Table 6-1—Component Load Summary.....	6-4
Table 7-1—Guide Tube Faulted Operation Stress Margins	7-2
Table 7-2—U.S. EPR Top Nozzle Faulted Stress Analysis.....	7-5
Table 7-3—U.S. EPR Fuel Rod Cladding Faulted Stresses.....	7-7
Table 7-4—Unirradiated Normalized SSE Top Nozzle Moments	7-9
Table 7-5—Unirradiated Normalized SSE Bottom Nozzle Moments.....	7-9
Table 7-6—Irradiated Normalized SSE Top Nozzle Moments	7-10
Table 7-7—Irradiated Normalized SSE Bottom Nozzle Moments	7-10
Table A-1—Guide Tube Displacements - Spacer B30121	A-35
Table A-2—Guide Tube Displacements - Spacer B30122	A-36

List of Figures

	<u>Page</u>
Figure 1-1—U.S. EPR Fuel Assembly Seismic and LOCA Analysis Flowchart.....	1-2
Figure 2-1—U.S.EPR Fuel Assembly Original Design Arrangement (2007)	2-7
Figure 2-2—U.S.EPR Fuel Assembly Optimized Design Arrangement (2012)	2-8
Figure 2-3—Weld Nugget Feature and Orientation of Size Dimension	2-9
Figure 4-1—U.S. EPR Single Beam Column Model Schematic	4-7
Figure 4-2—Lateral Stiffness Test Arrangement	4-11
Figure 4-3—U.S. EPR Lateral Frequency Forced Vibration Test Schematic	4-14
Figure 4-4—U.S. EPR Lateral Frequency Forced Vibration Test Arrangement	4-15
Figure 4-5—U.S. EPR Lateral Natural Frequency Test – Free Vibration	4-17
Figure 4-6—U.S. EPR Lateral Natural Frequency Test – Pulling System	4-18
Figure 4-7—U.S. EPR Lateral Fuel Assembly Loading Curves.....	4-20
Figure 4-8—U.S. EPR Lateral Fuel Assembly Lateral Frequency Tests	4-22
Figure 4-9—HTP-LX Model Schematic	4-27
Figure 4-10—Maximum Deflection versus Maximum Impact Configuration	4-29
Figure 4-11—HTP Fuel Designs – Frequency versus Amplitude	4-31
Figure 4-12—Frequency Percent Delta from BOL to BOL Benchmark at []	4-32
Figure 4-13—Frequency Percent Drop from BOL Benchmark at [] to EOL.....	4-33
Figure 4-14—HTP Design Family Dynamic Similarity	4-35
Figure 4-15—U.S. EPR BOL Lateral Loading Curve versus Frequency Sweep Models	4-37
Figure 4-16—U.S. EPR EOL Lateral Loading Curve versus Frequency Sweep Models	4-38
Figure 4-17—U.S. EPR Hydrodynamic Coupling Elements – Schematic.....	4-41
Figure 4-18—HTP Fuel Assembly Structural Damping versus Amplitude.....	4-44
Figure 4-19—Unirradiated Damping Ratio Measurements.....	4-48
Figure 4-20—Effect of Temperature on Fuel Assembly Damping	4-50
Figure 4-21—1-DOF System – Motion Decay Envelope	4-54
Figure 4-22—Simulated Irradiated Damping Ratio Measurements	4-56
Figure 4-23—Sample HTP Spacer Grid Loading Curve.....	4-66

List of Figures
(continued)

	<u>Page</u>
Figure 4-24—Spacer Grid Allowable Load Definition	4-67
Figure 4-25—Spacer Grid Allowable Load Definition	4-71
Figure 4-26—U.S.EPR HTP [] Strip Grid – BOL Test Data.....	4-73
Figure 4-27—Control Rod to Guide Tube Clearance Schematic.....	4-75
Figure 4-28—HTP Grid [15 mil] Strip - Control Rod Gauge.....	4-75
Figure 4-29—17x17 HTP [] Strip Grid – BOL Test Data	4-78
Figure 4-30—Comparison of Rate of Strength and Relaxation versus Fluence	4-82
Figure 4-31—17x17 HTP [] Grid – EOL Test Data	4-84
Figure 4-32—Comparison of Irradiated Hot versus Ambient Temperature Grid Strength Tests	4-87
Figure 4-33 Strip Parallel to Standard Direction of Impact	4-91
Figure 4-34 Strip Parallel to Non Standard Direction of Impact.....	4-92
Figure 4-35—17x17 HTP [] Grid Strength – BOL versus EOL.....	4-94
Figure 4-36—17x17 HTP [] Grid Strength – BOL versus EOL.....	4-95
Figure 4-37—Spacer Grid Test and Element Schematic.....	4-97
Figure 4-38—Impact Behavior of a Linear Visco-Elastic Element.....	4-99
Figure 4-39—Impact Test of HTP [] grid 10HP2790 – Energy Storage and Dissipation	4-101
Figure 4-40—Impact Test of HTP [] grid B30125 – Energy Storage and Dissipation	4-102
Figure 4-41—U.S. EPR Core Row Model Schematic.....	4-106
Figure 4-42—U.S. EPR FA-FA Gapped Spring-Damper Connecting Elements	4-108
Figure 4-43—U.S. EPR Rotational Spring Arrangement for Core Row Models	4-110
Figure 4-44—U.S. EPR Fuel Assembly Impact Test Model	4-113
Figure 4-45—U.S. EPR Fuel Assembly Impact Test – Detailed Spring Arrangement.....	4-114
Figure 4-46—Comparison of CASAC Model and Test – Free Vibration (in air).....	4-122
Figure 4-47—Comparison of CASAC Model and Test - Displacements (in air)	4-122
Figure 4-48—Comparison of CASAC Model and Test Impact Loads (in water).....	4-123
Figure 4-49—U.S. EPR Vertical Seismic and LOCA Model	4-128

List of Figures (continued)

	<u>Page</u>
Figure 4-50—U.S. EPR Vertical Stiffness Test Arrangement.....	4-131
Figure 4-51—Axial Stiffness - Model & Test.....	4-134
Figure 4-52—Axial Sliding Element at Fuel Rod to Spacer Grid Interface	4-142
Figure 4-53—Non-Linear Rotational Spring at Fuel Rod to Spacer Grid Interface ...	4-143
Figure 4-54—U.S. EPR Non-Linear Finite Element Model Arrangement	4-144
Figure 4-55—Irradiated and Unirradiated Model Benchmark	4-148
Figure 4-56—Guide Tube to Top Nozzle Connection Joint	4-156
Figure 4-57—Guide Tube to Top Nozzle Connection Joint	4-157
Figure 5-1—U.S. EPR Core Spacer Grid Locations [] under Combined Seismic and LOCA Loads – Eight Independent Scenarios	5-6
Figure 6-1—U.S. EPR Vertical LOCA Force Time Histories per FA.....	6-2
Figure 6-2—U.S. EPR Vertical SSE Displacement Time Histories.....	6-3
Figure A-1—Ultimate Elongation for Zirconium Alloy Guide Tube Specimens	A-3
Figure A-2—Tensile Strength for Irradiated and Unirradiated Zirconium Alloy Guide Tube Specimens	A-4
Figure A-3—Irradiated M5 [®] Yield Strength versus Fluence	A-6
Figure A-4—Total Elongation versus Fluence for M5 [®]	A-7
Figure A-5—Irradiation Stress Relaxation for Zirconium Alloys.....	A-8
Figure A-6—Grid Buckling Load versus Cladding Insertion Force	A-11
Figure A-7—Irradiated Grid Failure Mode	A-12
Figure A-8—Variation of Grid Buckling Load with Axial Grid Position	A-13
Figure A-9—Grid Buckling Load versus Oxide Layer Thickness.....	A-15
Figure A-10—Spacer Grid Impact Testing Schematic.....	A-17
Figure A-11—Spacer Grid Testing Bench	A-18
Figure A-12—Spacer Grid Pre-Test Inspection.....	A-19
Figure A-13—Spacer Grid Pre-Test Insertion Load Measurement.....	A-20
Figure A-14—Spacer Grid Control Rod Test Gauge	A-21
Figure A-15—Example of a Buckled U.S. EPR HTP Spacer Grid.....	A-22
Figure A-16—Detail of a Buckled U.S. EPR HTP Spacer Grid.....	A-23

List of Figures
(continued)

	<u>Page</u>
Figure B-9—Lateral BOL LOCA Loading – Case HELB-0HL	B-9
Figure B-10—Lateral BOL LOCA Loading – Case HELB-100CL	B-10
Figure B-11—Lateral EOL Seismic Loading – Soil Case 1n2u	B-11
Figure B-12—Lateral EOL Seismic Loading – Soil Case 1n5a	B-12
Figure B-13—Lateral EOL Seismic Loading – Soil Case 2sn4u.....	B-13
Figure B-14—Lateral EOL Seismic Loading – Soil Case 4u	B-14
Figure B-15—Lateral EOL Seismic Loading – Soil Case 5a	B-15
Figure B-16—Lateral EOL Seismic Loading – Soil Case bblb.....	B-16
Figure B-17—Lateral EOL Seismic Loading – Soil Case bbub	B-17
Figure B-18—Lateral EOL Seismic Loading – Soil Case bbub-cr	B-18
Figure B-19—Lateral EOL LOCA Loading – Case HELB-0HL	B-19
Figure B-20—Lateral EOL LOCA Loading – Case HELB-100CL	B-20

Nomenclature

Acronym	Definition
1-DOF	One-degree-of-freedom
2D	Two-dimensional
3D	Three-dimensional
BN	Bottom Nozzle
BOL	Beginning of Life
CMM	Coordinate Measuring Machine
DOF	Degree of Freedom
EOL	End of Life
FA	Fuel Assembly
FEM	Finite Element Model
FR	Fuel Rods
GT	Guide Tube
HMP	High Mechanical Performance
HTP	High Thermal Performance
ISG	Intermediate Spacer Grid
LCP	Lower Core Plate
LEG	Lower End Grid
LOCA	Loss of Coolant Accident
LVDT	Linear Variable Differential Transducer
OBE	Operating Basis Earthquake
OD	Outside Diameter
RMS	Root Mean Square
SRSS	Square Root of Sum of Squares
SSC	Structures, Systems and Components
SSE	Safe Shutdown Earthquake
TN	Top Nozzle
UCP	Upper Core Plate
UEG	Upper End Grid

1.0 INTRODUCTION AND SUMMARY

This technical report contains a detailed account of the seismic and loss of coolant accident (LOCA) faulted condition evaluation of the U.S. Evolutionary Power Reactor (EPR) fuel assembly. It is intended to accompany and act as source reference for Topical Report ANP-10285P - U.S. EPR Fuel Assembly Mechanical Design Topical Report (Reference 1).

The report describes:

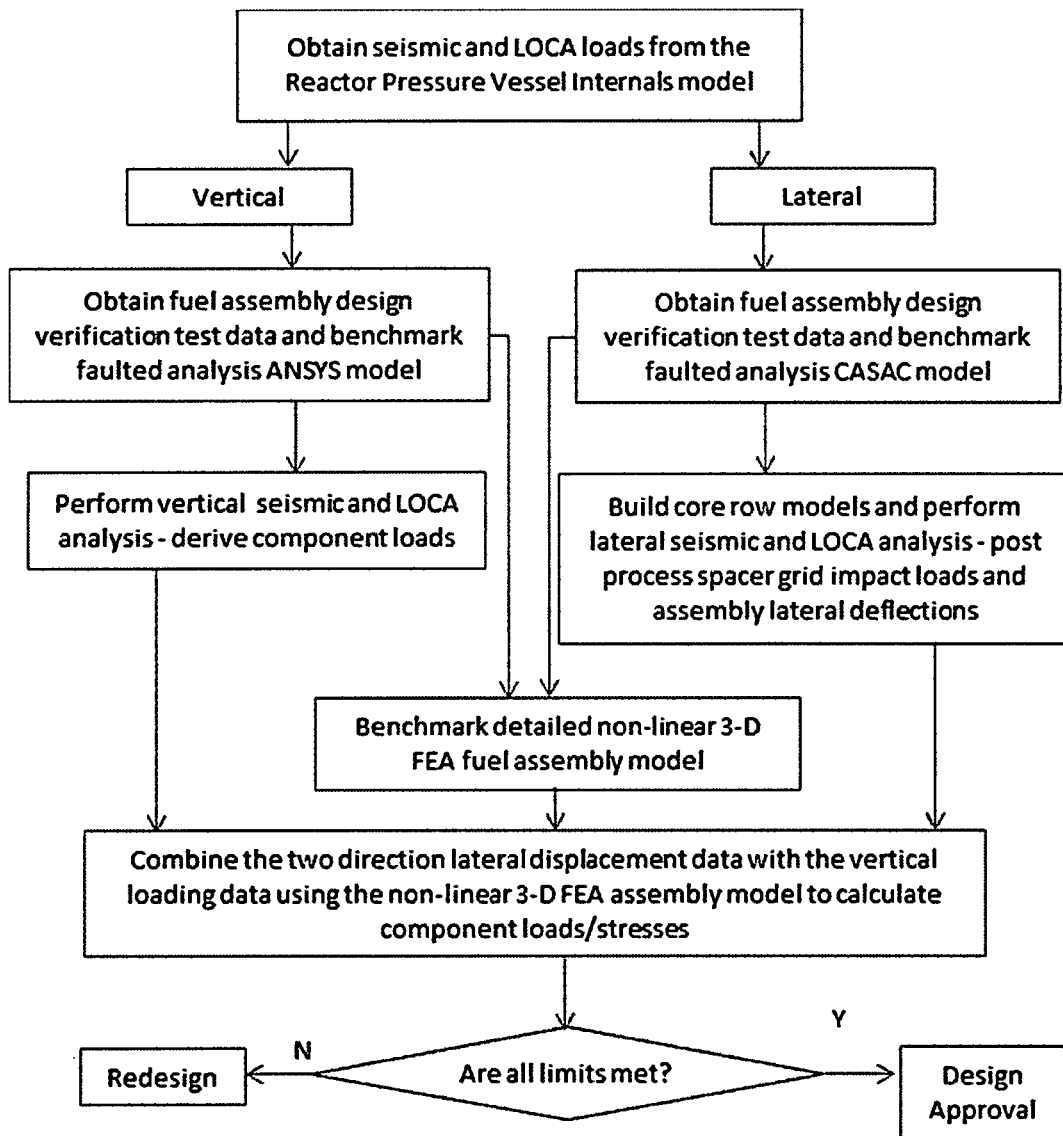
- The methodology used in this analysis.
- The design verification testing methodologies and results.
- The model construction and test benchmark.
- The results of the fuel assembly and component load analysis.

The methodology follows, generally, the established AREVA fuel assembly seismic and LOCA analysis faulted condition methodology described in Addenda 1 and 2 of BAW-10133PA (Reference 2). However, enhancements to the methodology were introduced in this report to allow the method to address the fuel assembly irradiated condition and refine the load combination process:

- Fuel assembly natural frequency and damping.
- Spacer grid allowable crushing load both in unirradiated and irradiated condition.
- Three-dimensional (3D) load combination using a detailed non-linear, 3D, finite element fuel assembly model, and component design limits.

The general flowchart of the analysis and design verification testing process is shown in Figure 1-1.

Figure 1-1—U.S. EPR Fuel Assembly Seismic and LOCA Analysis Flowchart



The analysis results for grid impact loads indicate that the U.S. EPR fuel assembly meets all design criteria. The maximum spacer grid impact loads separated by frequency sweep case, grid design, and irradiated versus unirradiated condition are presented in Table 1-1. The limiting spacer grid margins by grid design and irradiated versus unirradiated condition are summarized in Table 1-2. The data indicates that both

the irradiated and unirradiated condition margins are substantial []

The assessment of the maximum permanent deformation for the unirradiated spacer grids is summarized in Table 1-3. While the unirradiated condition spacer grids have a maximum allowable deformation of [], the bounding permanent deformation predicted conservatively from the standard grid test loading curves is [] for the entire U.S. EPR core. []

]

The assessment of the non-grid component strength was carried out on non-linear 3D finite element models representing the unirradiated and irradiated condition, and benchmarked to the corresponding fuel assembly lateral stiffness tests. The load combination method combines loads in all three directions in accordance with the requirements of Regulatory Guide 1.92 (Reference 3). As an added conservatism, the lateral load combination is performed without regard to time phasing. The results of the non-grid component strength assessment are presented in Table 1-4, and show substantial margins, especially when taking into account the conservatism included in the analysis and material stress limits, which are discussed in more detail in Section 4.3 and 7.0.

In view of the inherent conservatism in the analytical fuel assembly and spacer grid models as well as the conservatism of the test protocols for the spacer grid allowable load, control rod insertability and component strength, it can be concluded that the U.S. EPR fuel assembly spacer grids and non-grid components comply with all design criteria with significant margin.

**Table 1-1—U.S. EPR Spacer Grid Impact Load Margins – All
Frequency Sweep Cases**

Table 1-2—U.S. EPR Spacer Grid Limiting Impact Load Margins

**Table 1-3—Frequency Sweep Cases w. Permanent Deformation over
Manufacturing Tolerance**

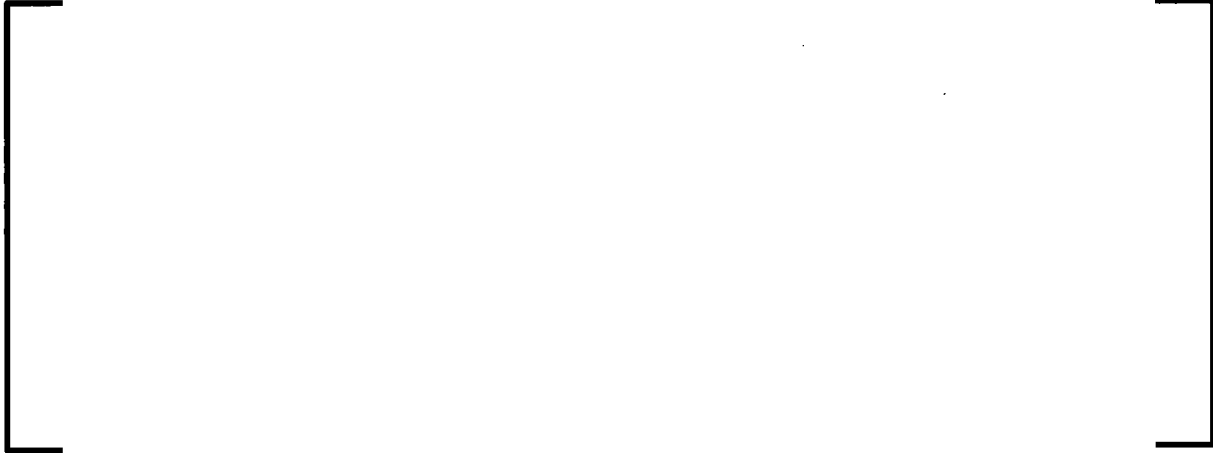


Table 1-4—Non-Grid Component Strength Margins



2.0 U.S. EPR FUEL ASSEMBLY FEATURES, FUNCTIONAL REQUIREMENTS, AND ACCEPTANCE CRITERIA UNDER SEISMIC AND LOCA LOADS

2.1 U.S. EPR Fuel Assembly Features

The original U.S. EPR fuel assembly arrangement is shown in Figure 2-1. This configuration is described in detail in ANP-10285P Reference 1, and was the basis for the first submittal of that topical report. Some of the major features were:

- 17x17-rod array, specifically developed for the U.S. EPR design.
- 265 fuel rods with M5[®] cladding material, with one extra fuel rod (FR) in the center of the array instead of the traditional instrument tube.
- Top and bottom end spacer grids that have a high mechanical performance (HMP) design with Alloy 718 strip material.
- Intermediate spacer grids that have high a thermal performance (HTP) design with M5[®] strip material, [] nominal weld nugget size (clarification of weld nugget parameter shown in Figure 2-3).
- 24 guide tubes with a MONOBLOC™ design using M5[®] alloy.
- The intermediate M5[®] HTP spacer grids are welded to each guide tube (GT).
- The Inconel HMP end grids are axially constrained by M5[®] alloy sleeves, welded directly to each guide tube above and below the corresponding grid positions.

In May 2012, during a public meeting with the Nuclear Regulatory Commission (NRC), AREVA presented a plan to close open questions regarding the U.S. EPR Fuel Assembly Design Topical Report. In an effort to improve design margins under seismic events, AREVA made a design change to the U.S. EPR fuel architecture, in which stronger HTP spacer grids are incorporated into critical elevations on the fuel assembly.

Relative to the original design discussed in the previous paragraphs, the optimized design incorporates the following changes:

particular. Of particular importance for the Fuel System Design are three requirements concerning SSE and associated applied loads:

- The nuclear power plant must be designed so that, if the Safe Shutdown Earthquake Ground Motion occurs, certain structures, systems, and components will remain functional and within applicable stress, strain, and deformation limits. In addition to seismic loads, applicable concurrent normal operating, functional, and accident-induced loads must be taken into account in the design of these safety-related structures, systems, and components.
- The required safety functions of structures, systems, and components must be assured during and after the vibratory ground motion associated with the Safe Shutdown Earthquake Ground Motion through design, testing, or qualification methods.
- It is permissible to design for strain limits in excess of yield strain in some of these safety-related structures, systems, and components during the Safe Shutdown Earthquake Ground Motion and under the postulated concurrent loads, provided the necessary safety functions are maintained.

The first requirement listed above establishes that for Faulted Operation, certain SSCs must be designed to a more stringent functional integrity requirement, as opposed to a more relaxed structural integrity requirement. Further, the functional integrity requirement must be met not only under SSE loads, but under combined SSE, Normal Operation, and functional and accident-induced loads.

The second requirement listed above establishes that the functional integrity requirement applies during and after the SSE plus accompanying normal and accident loads. This requirement has far reaching implications for the fuel assembly components under faulted conditions, and is expanded upon in the subsequent section, which discusses particular acceptance criteria for various fuel assembly components.

Finally, the third item in the list above clearly indicates that elastic operation is not required even for the safety-related structures during an SSE (acting either alone, or concurrently with the postulated loads) and allows the use of non-elastic limits for SSE and accompanying accident-induced loads, as long as the functional integrity requirement is met.

The regulation specifies that the OBE earthquake does not need to be evaluated if its severity is 1/3 or less of the SSE severity. The OBE earthquake severity for the U.S. EPR design is 1/3 of the severity of the SSE earthquake and therefore does not require a specific evaluation.

The design criteria used for the U.S. EPR Fuel Assembly have been formulated to meet all the general design requirements, and in some respects are stricter than the criteria formulated in current guidance and established industry practices, as discussed in the following section.

2.3 U.S. EPR Fuel Assembly Acceptance Criteria Under Seismic and LOCA Loads

This section addresses only the criteria with direct application to seismic and LOCA faulted conditions, as defined in Appendix A of Reference 1. The criteria are separate for spacer grid and non-grid components. The criteria for spacer grids are governed by tested loads according to a specific test protocol, while the non-grid components are governed by the limits defined in the American Society of Mechanical Engineers (ASME), Boiler and Pressure Vessel Code, Section III, "Rules for Construction of Nuclear Power Plant Components," (Reference 4).

2.3.1 Spacer Grid Acceptance Criteria

The spacer grid peak impact load is limited by the allowable grid crushing load, which is derived from impact test data (Section 4.1.4). The AREVA grid allowable crushing load definition distinguishes between the unirradiated and the irradiated grid condition.

For the unirradiated grid condition the following criteria apply:

- The allowable crushing load is defined as the load that produces a limited acceptable cumulative deformation under a [] impact test process (details in Section 4.1.4.1.4).
- An evaluation of the degree of deformation that occurs will be made. The degree of deformation will be less than that caused by the defined crushing load [] since all of the loads will be required to be less than this value. An evaluation of the impact of this calculated maximum deformation will be made to demonstrate that the limiting values for CHF and LOCA criteria are not impacted. It is expected that most fuel assemblies will experience deformations less than the manufacturing tolerance [] and thus can be concluded to not impact CHF or LOCA criteria. It is expected that only those fuel assemblies on the periphery will experience deformations greater than manufacturing tolerance and will require additional evaluation or disposition.
- The spacer grid at the limit deformation must provide an unencumbered path for the control rod insertion.

For the irradiated grid condition the following criteria apply:

- The allowable crushing load is defined as the buckling load under a [] impact test process (details in Section 4.1.4.1.6).
- Control rod insertion is ensured, and critical heat flux and LOCA are not impacted, since the deformation at the allowable crushing load is negligible.

2.3.2 Non-Grid Structural Component Acceptance Criteria

The non-grid structural components include the guide tubes, the top and bottom nozzle, the upper and lower connections, and the spacer grid to guide tube attachments (direct welds for the HTP grids, and welded sleeves for the HMP grids). With the exception of

guide tubes, the general limits for non-grid structural components are the Level D criteria for faulted operation in Appendix F of the ASME Code (Reference 4).

2.3.2.1 Guide Tube Faulted Operation Acceptance Criteria

The guide tubes include a special case because they must ensure the functional requirement of control rod insertability. To this end, the guide tube stresses are limited by the Level C criteria in the ASME Code, Subsection NG (Reference 4), and by critical buckling loads. Together, these two sets of limits ensure that the functional requirement of the guide tubes is maintained. The suitability of these design limits is further addressed in Section 7.0.

2.3.2.2 Top and Bottom Nozzle Faulted Operation Acceptance Criteria

The bottom nozzle (BN) is an intricate component that includes brazed sub-components, which makes it difficult to perform a stress analysis. Therefore, the Level D limits for the top nozzle are represented by the tested collapse load, as indicated in Appendix F-1321.6 of the ASME Code (Reference 4). The collapse load test, data processing, and conversion from room temperature to in-reactor operating temperature based on the material yield strength ratio are performed in accordance with Appendix II-1430 in the ASME Code (Reference 4).

The top nozzle Level D limits are based on linear stress analysis, and are the minimum of $2.4 S_m$ or $0.7 S_u$ for primary membrane, and 1.5 times this amount for primary membrane plus bending or local membrane.

2.3.2.3 Guide Tube Connections Acceptance Criteria

The design limits for the guide tube upper connection are consistent with Level C service limits in the ASME Code (Reference 4), and are based on tested ultimate collapse loads. The design limits for the grid to spacer grid connections and the guide tube lower connections are consistent with Level D service limits and are based on tested collapse loads (grid to guide tube connections), or stress analysis (for the guide tube lower connection).

Figure 2-1—U.S.EPR Fuel Assembly Original Design Arrangement (2007)

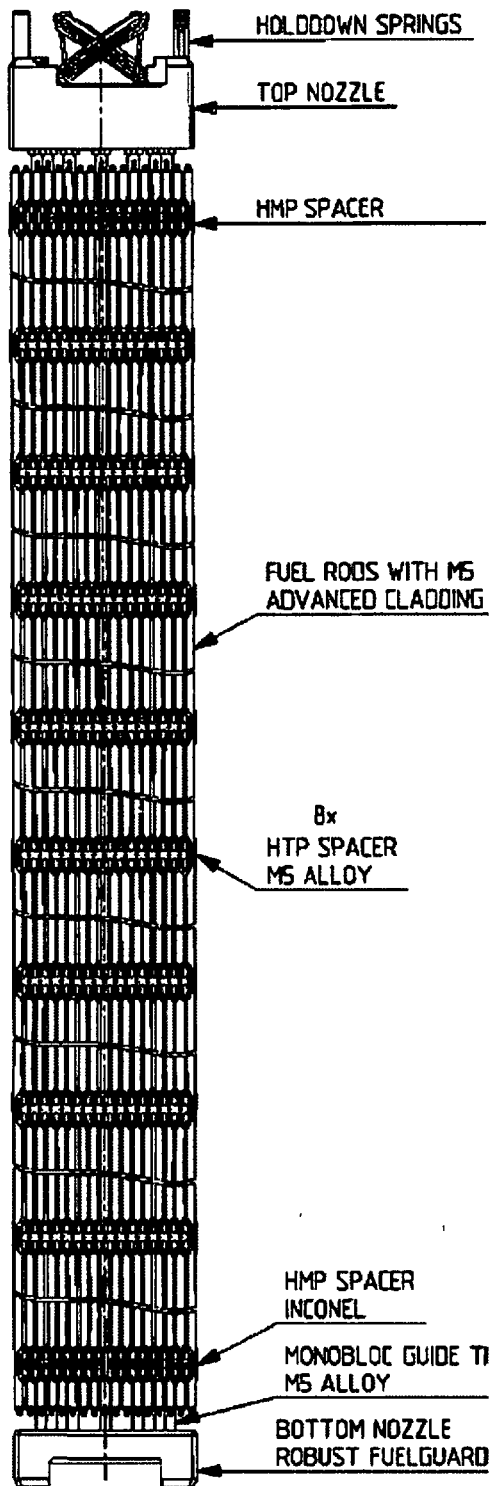


**Figure 2-2—U.S.EPR Fuel Assembly Optimized Design Arrangement
(2012)**

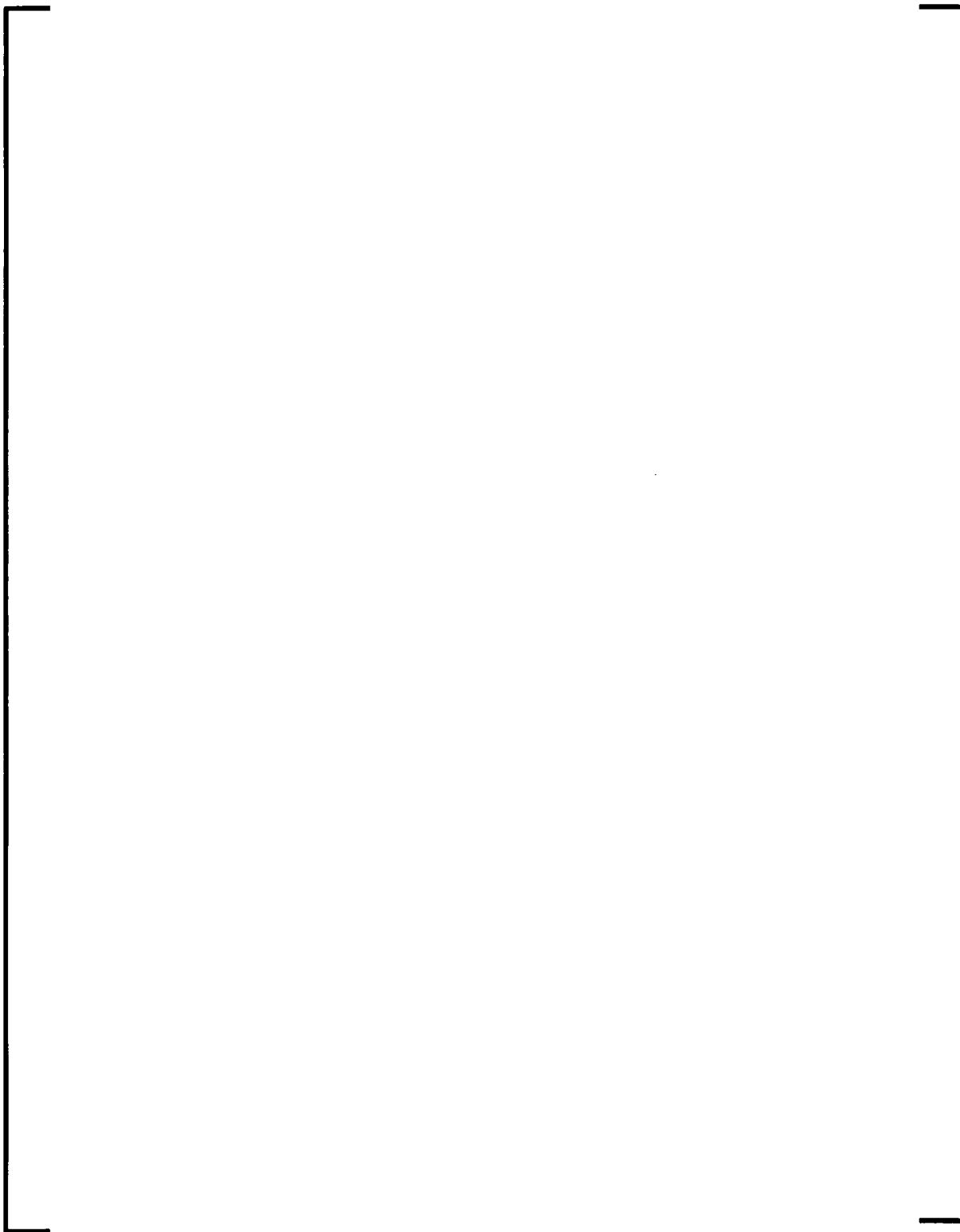


Figure 2-3—Weld Nugget Feature and Orientation of Size Dimension



3.0 U.S. EPR FUEL ASSEMBLY SEISMIC AND LOCA BOUNDARY CONDITIONS

The seismic and LOCA boundary conditions for the U.S. EPR consist of:

- Absolute coordinate system displacement time histories at the lower and upper core plate, and the top of the heavy reflector for lateral seismic and LOCA analysis.
- Absolute coordinate system displacement time histories for vertical seismic analysis, and fuel assembly hydraulic load time histories for vertical LOCA analysis.

This section contains a general overview of the process of deriving the U.S. EPR fuel assembly boundary conditions. The details are covered in U.S. EPR FSAR, Tier 2, Chapter 3 (Reference 5), and the subordinated references.

3.1 *U.S. EPR Seismic and LOCA Model Hierarchy*

The inputs for the U.S. EPR fuel assembly seismic and LOCA loading are derived from a reactor pressure vessel internals model, which is one level above the core row model in the dynamic analysis model hierarchy. The model is discussed in Chapter 3 of Reference 3. Each soil case has two associated time histories, which separately account for the fuel elements in an unirradiated and irradiated condition. The soil cases analyzed are described in detail in Chapter 3 of Reference 3. The inputs to the model consist of the basemat seismic acceleration time histories. The outputs consist of displacement time histories relative to the basemat. Displacement boundary conditions need to be expressed in the absolute coordinate system since the fuel analysis uses them. Therefore, the relative displacements output from the reactor vessel internals model are converted into absolute coordinate system displacements by adding the absolute coordinate system basemat displacements in the lateral and rocking motion.

3.2 U.S. EPR Seismic and LOCA Loads

The seismic SSE time histories cover the following nine governing soil cases:

- 1n2u,
- 1n5a,
- 2sn4u,
- 4u,
- 5a,
- BBLB,
- BBUB,
- BBBE,
- BBUB-CR.

The results summarized in this section do not include soil case BBBE (best estimate), but this case is bounded by the BBLB (lower bound) and BBUB (upper bound) cases. A set of seismic time histories consists of two lateral directions and one vertical direction at the three locations (lower core plate, upper core plate, and top end of the heavy reflector) where displacements are imposed.

The LOCA time histories selected for this analysis consist of the two limiting cases:

- The zero percent power condition case for the break on the Safety Injection System Line on the Hot Leg (HELB-0HL).
- The 100 percent power condition case for the break on the safety injection system line on the cold leg (HELB-100CL)

LOCA loads are applied as displacement conditions in the two lateral directions, and as hydraulic forces in the vertical direction. Seismic and LOCA loading time history and response spectra plots are provided in Appendix B.

4.0 U.S. EPR FUEL ASSEMBLY METHODOLOGY FOR EVALUATION OF DYNAMIC RESPONSE, COMPONENT LOADS, AND STRESS ANALYSIS UNDER SEISMIC AND LOCA CONDITIONS

This section describes the methodology employed to assess the U.S.EPR external accident loading response, and the component loads and stresses.

The seismic and LOCA external loading methodology includes a few important focus areas:

- Component, fuel assembly, and core modeling techniques and features,
- Design verification testing,
- Analysis techniques and load combination,
- Structural evaluation and acceptance criteria.

The acceptance criteria have been discussed at a higher level in Section 2.3, and will be discussed in more detail in this section, as they are applied to various components.

In practice, the models for lateral and vertical loading are different in terms of level of detail, architecture and features, and therefore, building a common model for these loading scenarios is impractical. Consequently, the evaluation is performed on distinct models for the lateral and vertical loading directions, respectively. The responses from these models are either used directly for comparison with allowable loads (as in the case of spacer grids), or are used as input on a more detailed 3D fuel assembly model in order to perform the load combination and component stress evaluation.

For the purpose of improving readability, the methodology discussion is separated into three sections in this document, concentrating on:

1. Lateral seismic and LOCA analysis (Section 4.1).
2. Vertical seismic and LOCA analysis (Section 4.2).
3. Load combination and component stress evaluation (Section 4.3).

Each section discusses the main focus areas of accident analysis, including design verification testing, analysis techniques, and applicable software, as they pertain to the particular model architecture suitable for each stage of the analysis.

4.1 U.S. EPR Fuel Assembly Lateral Seismic and LOCA Methodology

This section discusses the fuel assembly lateral seismic and LOCA loading analysis methodology. In principle, the lateral methodology used for the U.S. EPR follows the generic AREVA methodology of BAW-10133(PA) (Reference 2), with some refinements and additional steps, which will be highlighted in this technical report.

The methodology involves a hierarchical model structure:

1. The fuel assembly model is the primary building block. It consists of a single column modeled with beam elements, and concentrated rotational springs at grid elevations. This model is linear. There is a more detailed discussion on the validity of this modeling approach included in Section 4.1.1. Some of the parameters of this model are derived analytically from first principles, and some are adjusted to match tested behavior from the design verification tests.
2. The spacer grid impact model is the connecting element between fuel assemblies, and between fuel assemblies and the heavy reflector. This element is a combination of a non-linear gap element, and a linear visco-elastic element. The validity of this modeling approach is discussed in more detail in Section 4.1.4. All the parameters of the grid model are derived by benchmarking to dynamic impact test results and the gap size is derived from core geometry.
3. The core models consist of a two-dimensional (2D) grouping of a given number of fuel assemblies across a row (7, 11, 13, 15 or 17), and represent a complete cross-section through the core in one of the symmetry directions. The core model groups together the individual fuel assembly models by coupling them with the non-linear grid impact elements, and accounting for the fluid-structure-interaction effects. These effects are modeled in the form of hydrodynamic coupling elements

(Section 4.1.2) and reactor coolant flow induced damping (Section 4.1.3). The detailed discussion of core model structure is provided in Section 4.1.5.

The loading of the core models consists of displacement time-histories applied at the core plates and heavy reflector elevations. The response is post-processed to produce displacement time-histories at all elevations, reaction response at the end support points (i.e., top and bottom nozzles), and impact load time histories at the intermediate spacer grids.

The spacer grid impact maximum peak load is used in a direct comparison with the tested spacer grid allowable crushing load to demonstrate the suitability for service of the spacer grids. The lateral displacements are used as inputs on the detailed 3D finite element fuel assembly model to obtain the component loads and stresses. The individual components are qualified based on either stress allowable criteria or tested collapse load.

The core lateral model captures the response of one core row subjected to in-plane lateral support point motions, without concern for the likely interaction of the fuel assemblies in the row with fuel assemblies from other rows due to the three-dimensional nature of the excitation and response. The acceptability of this modeling technique is based on the inherent conservatism included in the analysis:

- The spacer grid allowable crushing load is tested in uni-directional impacts, which produces the most damaging loading. If the spacers were loaded simultaneously in two directions, each direction loading would serve as support for the other direction deformation, thus producing a higher spacer grid allowable load.
- Due to two-direction loading, the fuel assemblies from neighboring rows can interfere and disrupt the row configuration. This would reduce the maximum impact loads occurring on the core periphery compared to the 2D core row model predictions. In addition, because of this inter-row interference, the maximum

lateral deflection of the assemblies in the row would be reduced, and with it, the non-grid component stresses.

In view of the considerations listed above, it is concluded that when the 2D core row model is used to produce spacer grid peak impact loads and fuel assembly deflections, it is conservative in comparison with the actual 3D in-core behavior. In addition, the load combination technique where the maximum displacements on a given fuel assembly are computed from two independent orthogonal row models without regard to inter-row interference is conservative, and overpredicts component stresses.

The second critical aspect of the lateral seismic and LOCA methodology is the design verification testing, which is used to ensure that the models are benchmarked to actual test data, and that the analytical results are credible.

For the U.S. EPR program, a number of tests were performed on 14 ft HTP, 17x17 fuel assemblies in support of the lateral model development. The tests are listed as follows, and will be discussed in more detail within the relevant sections:

- Lateral stiffness test on an unirradiated fuel assembly (Section 4.1.1.2).
- Lateral modal analysis (forced vibration) test on an unirradiated fuel assembly (Section 4.1.1.2).
- Lateral pluck test with impacts on an unirradiated fuel assembly (Section 4.1.5.1).
- Lateral pluck test and modal analysis (forced vibration) test on a simulated irradiated condition fuel assembly (Section 4.1.1.2).
- Impact spacer grid tests (Section 4.1.4).

4.1.1 U.S. EPR Fuel Assembly Lateral Model – Single Fuel Assembly in Free Vibration in Ambient Air

4.1.1.1 Single Column Fuel Assembly Model Description

The building block of the lateral core model is the simplified fuel assembly single column model. The model consists of beam elements arranged in the vertical direction from the

top face of the bottom nozzle to the lower face of the top nozzle (TN). Additionally, the model includes rotational springs placed at each spacer grid elevation. These individual model elements are linear. The validity of this approach is discussed in more detail in Section 4.1.1.3. Each span between two spacer grids, or between spacer grids and the bottom nozzle /top nozzle are modeled by one element. The degrees of freedom at each node are lateral displacement and rotation. A schematic of the fuel assembly single beam column model and the correspondence with the U.S. EPR fuel assembly components and elevations are shown in Figure 4-1.

To account for the presence of the MONOBLOC™ guide tubes, the cross-sectional properties of the beam elements are different in the dashpot portion. The dashpot region is modeled as extending from the upper face of the lower tie plate to the HTP1 grid mid elevation. The approximation is valid, since the wall thickness transition in the guide tube is located within the HTP1 axial span. Although in the actual fuel assembly the fuel rods do not occupy the entire span between the bottom and top nozzles, the model assumes the bundle section properties extend all the way to the nozzles. The top and bottom nozzles are modeled as rigid, and therefore, they are not part of the model proper, but only impart on the guide tubes a fixed-end boundary condition. The lower end grid and the top end grid are not present in the model because of their close proximity to the nozzles and the fact that they cannot interact with the neighboring assembly during a seismic or LOCA event.

The inputs for the Euler-Bernoulli beam elements come in the form of direct geometric and material property data, calculated section properties, and equivalent density and elastic modulus. The direct inputs are discussed in detail in Section 4.1.1.2. The section area and moment of inertia are represented by the sum of the net section areas, or sectional inertia of all slender components in that particular span. No correction using the Parallel Axis Theorem is necessary (see Section 4.1.1.2), due to the fact that all guide tubes and fuel rods have the same displacement pattern, as defined by the common spacer grid interfaces and induced by the lateral translation-only motion of the top and bottom nozzles in the event of an earthquake or LOCA.

The second set of section properties includes the equivalent density and Young's modulus. The equivalent physical properties are necessary for the Fuel Assembly model, since the guide tubes and the fuel rods have different properties, but are lumped together in one element. The principle is to define the equivalent density so that the model fuel assembly mass per unit inch in every span, matches the combined mass per unit inch of the Guide Tubes, Instrument tube, and fuel rods. The equation is:

$$\rho_{eqv} = \frac{\rho_{GT} \cdot A_{GT} + \rho_{IT} \cdot A_{IT} + \rho_{FR} \cdot A_{FR}}{A_{GT} + A_{IT} + A_{FR}} \quad \text{Equation 4-1}$$

In Equation 4-1, A_{GT} , A_{IT} , and A_{FR} , represent the section areas of the guide tubes, instrument tubes, and fuel rods (cladding only). Similarly, ρ_{GT} , ρ_{IT} , and ρ_{FR} , represent the density of the guide tube, instrument tube and fuel rods, respectively. It must be mentioned that the fuel rod density is calculated as if the fuel rod mass were concentrated in the cladding.

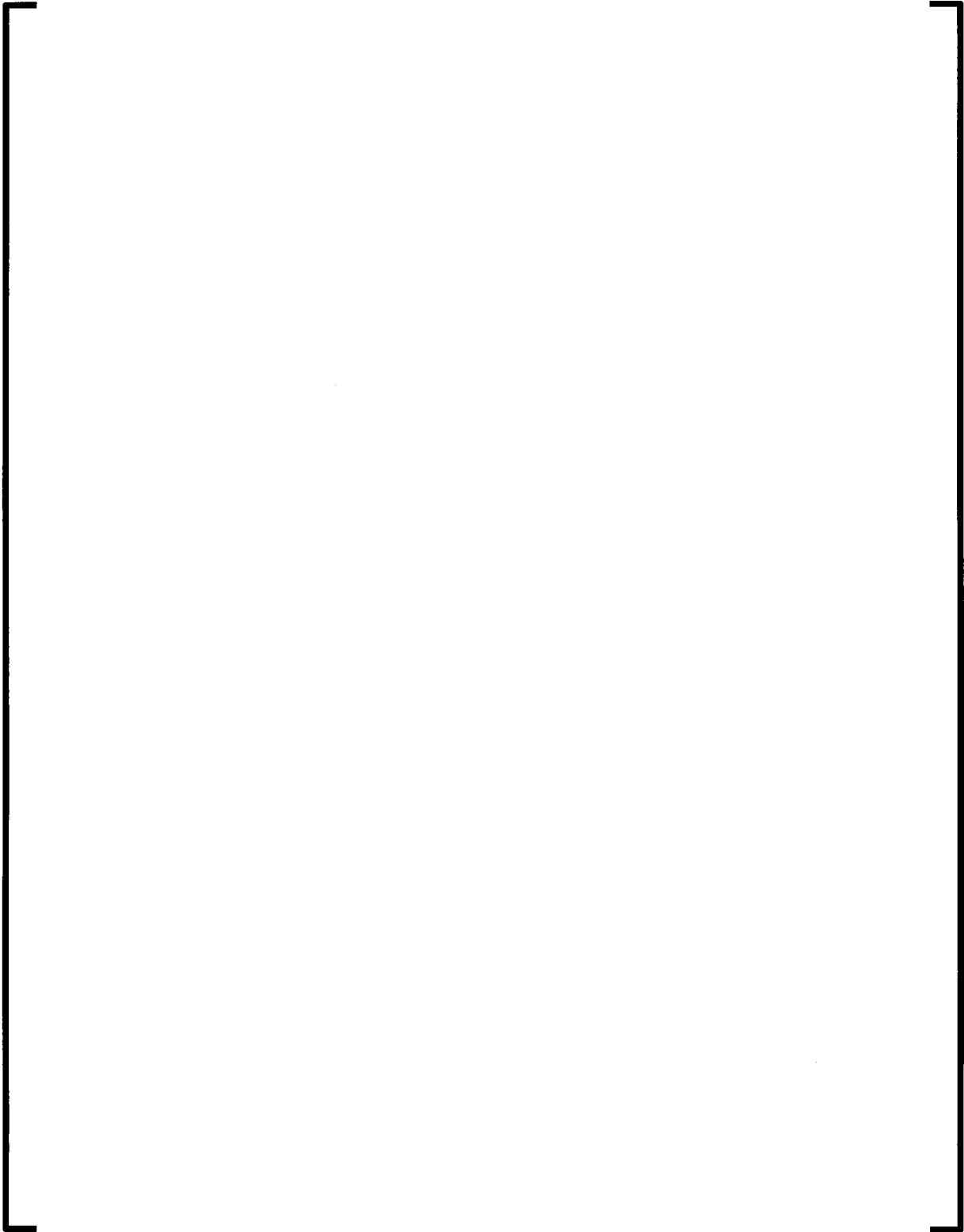
The equivalent Young's Modulus is calculated so that the bending stiffness of the unit length fuel assembly bundle element matches the sum of the bending stiffness of the guide tube, instrument tube, and fuel rods, per unit length. The equation is:

$$E_{eqv} = \frac{E_{GT} \cdot I_{GT} + E_{IT} \cdot I_{IT} + E_{FR} \cdot I_{FR}}{I_{GT} + I_{IT} + I_{FR}} \quad \text{Equation 4-2}$$

In Equation 4-2, I_{GT} , I_{IT} , and I_{FR} , represent the cross-sectional inertias of the guide tubes, instrument tubes, and fuel rods (cladding only). Similarly, E_{GT} , E_{IT} , and E_{FR} , represent the Young's Modulus of the guide tube, instrument tube and fuel rods (cladding only), respectively.

Also, it must be noted that Equation 4-1 and Equation 4-2 include the properties of the instrument tube. This is to account for the presence of an instrument tube in the center position of the tested assembly (HTP-LX), whereas this feature is not present in the U.S. EPR fuel. More detailed discussion is included in Section 4.1.1.2.

Figure 4-1—U.S. EPR Single Beam Column Model Schematic



The intermediate spacer grids (ISG) have a marked effect on the lateral stiffness of the fuel assembly, the most obvious of which is the stiffening effect, but the effect with the most implications for the model architecture is the effect on the ratio of Mode 3 and Mode 1 frequencies. It is known from Euler-Bernoulli beam theory found in "Principles and Techniques of Vibrations" (Reference 6) that a uniform column supported at the end points has a precisely specified ratio between the Mode 3 and Mode 1 frequencies, and this ratio ranges from 9:1 for the pinned-pinned case, to 5.4:1 for the clamped-clamped case. These two limits of the range correspond to zero and infinite rotational stiffness boundary conditions at the end points, respectively. For support conditions involving a finite rotational stiffness, the Mode 3 to Mode 1 frequency falls between these limits. From frequency tests performed on a large family of HTP fuel assemblies, including a representative U.S. EPR design, AREVA has demonstrated that the mode 3 to mode 1 frequency ratio is in a range centered around [], which is clearly outside the range for a uniform column with end boundary conditions only. The implication is that the spacer grids act as additional boundary conditions on the fuel assembly. The modeling approach is to represent the spacer grids as rotational springs with one end node on the fuel assembly column, and the other node fixed to ground. The rotational stiffness of all ISGs is assumed the same, and is determined through the test benchmarking process.

The single column fuel assembly model must be capable of representing the lateral dynamics of the fuel assembly over its entire service life. Given that the material elastic modulus does not change with irradiation, the only change to the model between the unirradiated and irradiated state is the spacer grid rotational stiffness. The change in rotational stiffness is justified by the spacer grid material stress relaxation (more detailed discussion included in Section 4.1.4), which reduces the grid to fuel rod coupling and in effect the fuel rod to spacer grid rotational stiffness under irradiation. The spacer grid rotational stiffness is determined by adjusting this parameter in the model for it to match the fuel assembly natural frequency for unirradiated and irradiated conditions (see Section 4.1.1.3).

4.1.1.2 U.S. EPR Fuel Assembly Single Column Model – Test Benchmark

The single column fuel assembly model uses information from two tests:

- The lateral stiffness test.
- The lateral natural frequency test – pluck test and forced vibration.

The lateral natural frequency test results are the basis for model benchmarking. These tests are briefly described in the following section.

4.1.1.2.1 Fuel Assembly Lateral Stiffness Test

Description:

The objective of this test is to determine the force/deflection curve of the fuel assembly under a lateral loading. The prototype is constrained at both nozzles. An axial load is applied to the hold-down springs of the test assembly during the test, to represent the interface loading at the end of life (EOL) condition. The axial preload has an insignificant effect on the results, but it ensures that the bottom nozzle is fully seated. The test is performed by laterally deflecting the center of the assembly up to a deflection of approximately one inch in one direction, without damaging the assembly. In the case of the U.S. EPR, there is no spacer grid at the assembly mid-span, so the deflection was applied at HTP 5, which is shown in Figure 4-2. The force required to deflect the assembly and the corresponding displacement are recorded continuously for the complete loading and unloading cycle. The test assembly is checked for straightness prior to the application of the preload. The measured deflection at the end of the test at zero force is the hysteresis. For repeatability, the loading/unloading cycle is enacted twice, with the load mechanism disconnected and the lateral offset in both directions removed after each cycle within a small variation of [].

End Product:

The plot of load versus displacement during fuel assembly loading and unloading is shown in Figure 4-7. The lateral set due to hysteresis of the fuel assembly is recorded after removal of the lateral load at the middle and end of each load cycle.

Instrumentation:

An inspection of the test assembly envelope and verticality must be performed before and after the test. The sensors used in a typical test are shown in Figure 4-2.

Figure 4-2—Lateral Stiffness Test Arrangement



For locations other than A and B, the LVDT arrangement consists of one LVDT measuring lateral displacement.

4.1.1.2.2 Fuel Assembly Lateral Natural Frequency Test

The lateral natural frequency of a fuel assembly can be determined in two distinct ways:

- Free vibration pluck test.
- Forced vibration modal analysis.

The results from these two tests can be used for different aspects of the model benchmarking process:

- The free vibration pluck test consists of pulling on the mid-span spacer grid a predefined amount, releasing, and recording the ensuing free vibration of the assembly at the spacer grids. The natural frequency and damping ratio are then determined from the damped natural frequency and the logarithmic decrement, which are calculated directly from the test data. This test presents the advantage that large amplitudes (one inch or higher) can be tested. Only the fundamental frequency and damping ratio as a function of amplitude can be determined from this test.
- The forced vibration modal analysis test consists of exciting the fuel assembly at one spacer grid elevation, recording the assembly response as a function of time at the intermediate grid elevations, and performing a modal identification to obtain the first five or six natural frequencies and modal damping ratios. This test allows a comparison of the higher mode natural frequencies to the fundamental frequency. The ratio between the mode 3 and mode 1 frequencies is used as a benchmarking target.

The following two sections describe the lateral natural frequency tests in more detail, and with direct reference to the U.S. EPR design.

4.1.1.2.2.1 U.S.EPR Lateral Natural Frequency Test – Forced Vibration Modal Analysis Test Description

Description:

This test is performed by using an electromagnetic shaker. The test fuel assembly prototype is supported at the top and bottom nozzle locations with prototypical fixtures for the in-reactor operation. The fuel assembly is excited with large spectrum signals and/or sinusoidal signals of constant energy and slowly varying frequency, by connecting the shaker coupling rod to one of the spacer grids, and recording the response at all grids in the assembly. The test arrangement is shown in Figure 4-4. The selection of the precise location where the shaker is to be connected on the test assembly is based on a preliminary modal analysis that produces the modal shapes. The shaker location must have a non-zero displacement in all desired modes, so that these modes can be driven from the excitation location. For the U.S. EPR, the best location to apply the excitation force is at the HTP2 grid, where all six mode shapes have non-zero displacements, as shown in Figure 4-3.

The test is conducted in two phases:

1. A large spectrum random excitation is applied to obtain all the modes of the structure in the frequency range of interest.
2. A more refined quantification of the modes of interest is performed either through the application of a constant energy slowly varying frequency harmonic signal, or a narrower band random excitation. For the harmonic signal technique, the natural frequency is detected by locating the minimum of the driving force frequency response function. For of the narrower band random excitation, the natural frequencies and damping ratios are found by a multi-modal rational fraction polynomial – Z method identification technique.

The common characteristic of the forced vibration methods is that the vibration amplitudes that can be attained are limited by the power of the shaker equipment. For

these reasons, these tests produce vibration amplitudes limited to [

]

Figure 4-3—U.S. EPR Lateral Frequency Forced Vibration Test Schematic

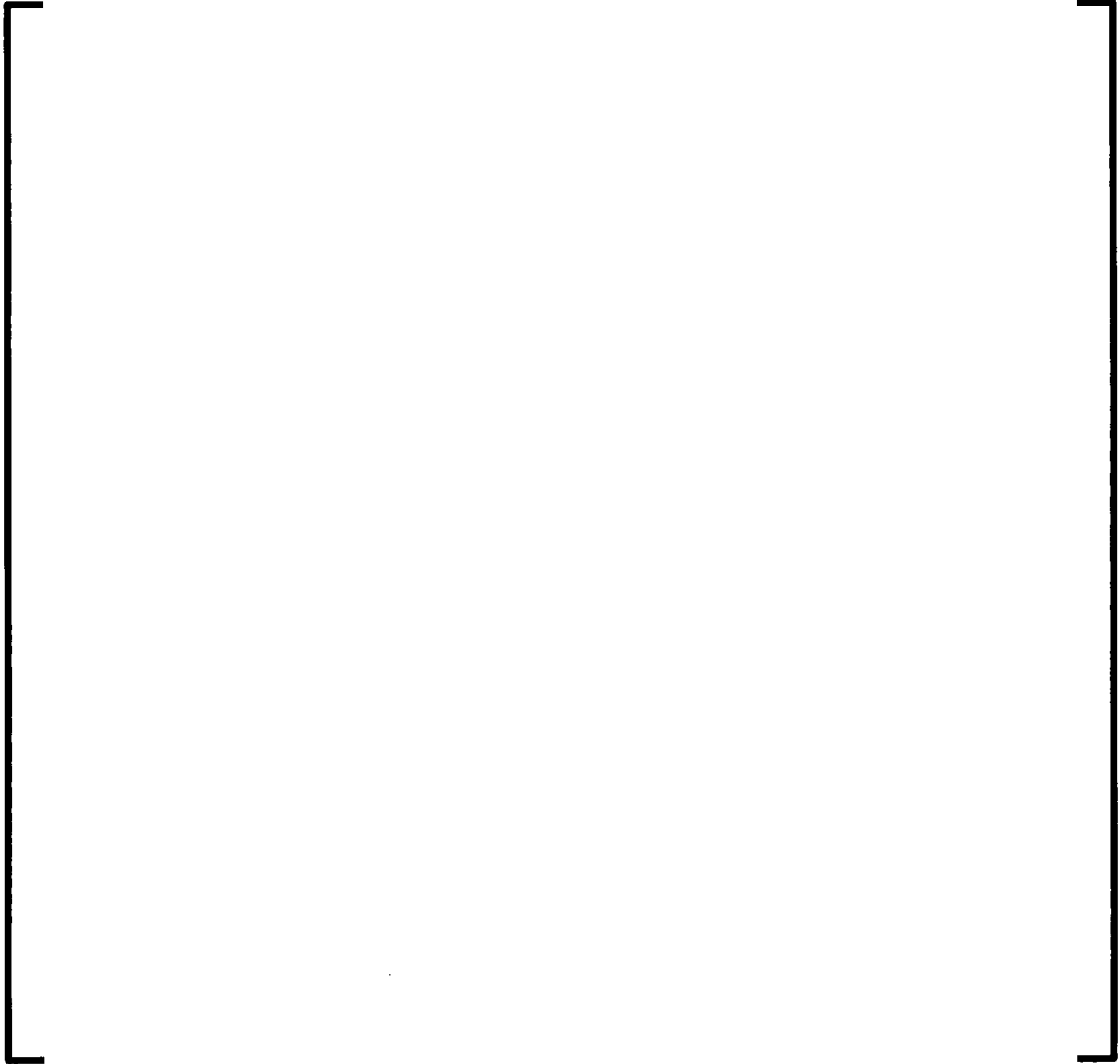


**Figure 4-4—U.S. EPR Lateral Frequency Forced Vibration Test
Arrangement**

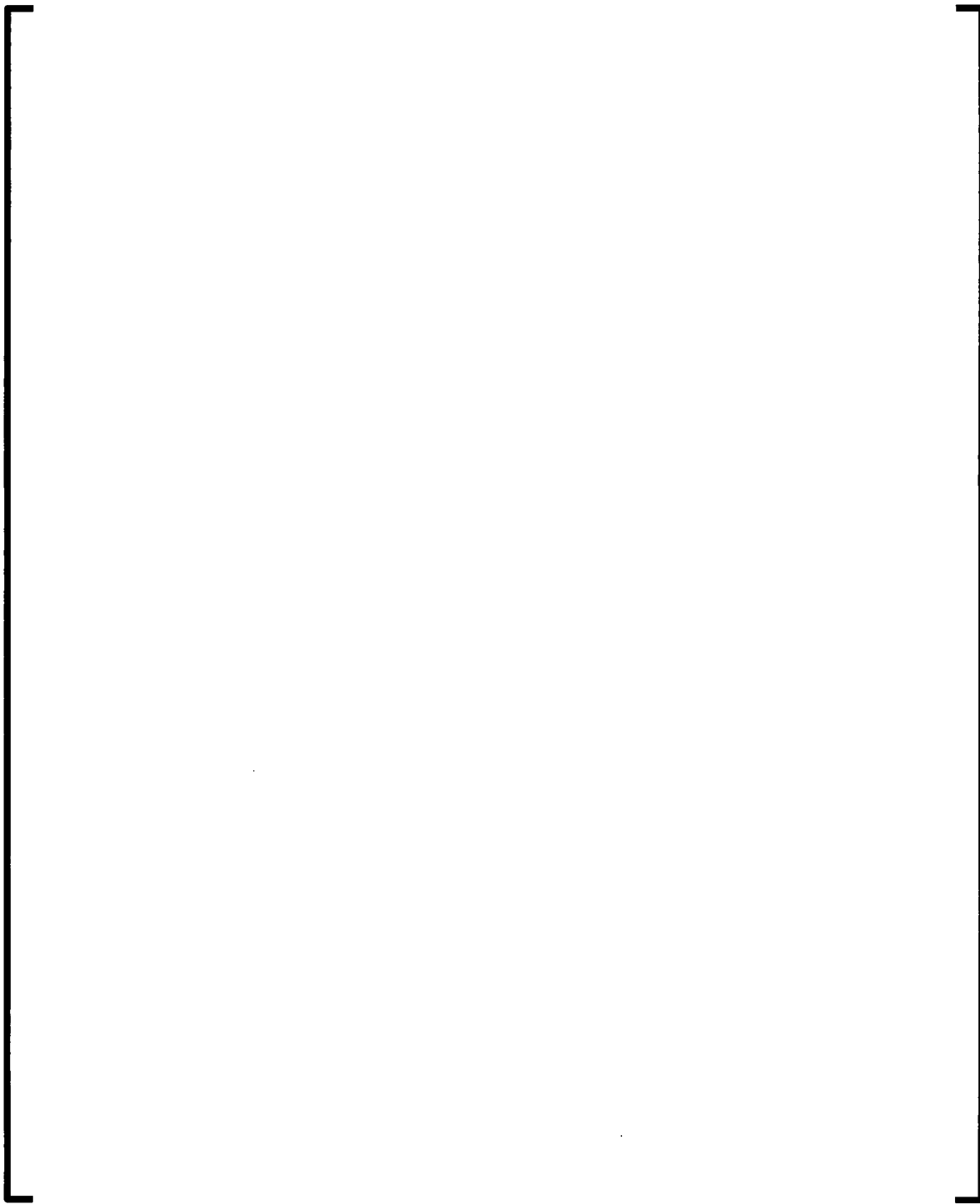


Figure 4-5—U.S. EPR Lateral Natural Frequency Test – Free Vibration

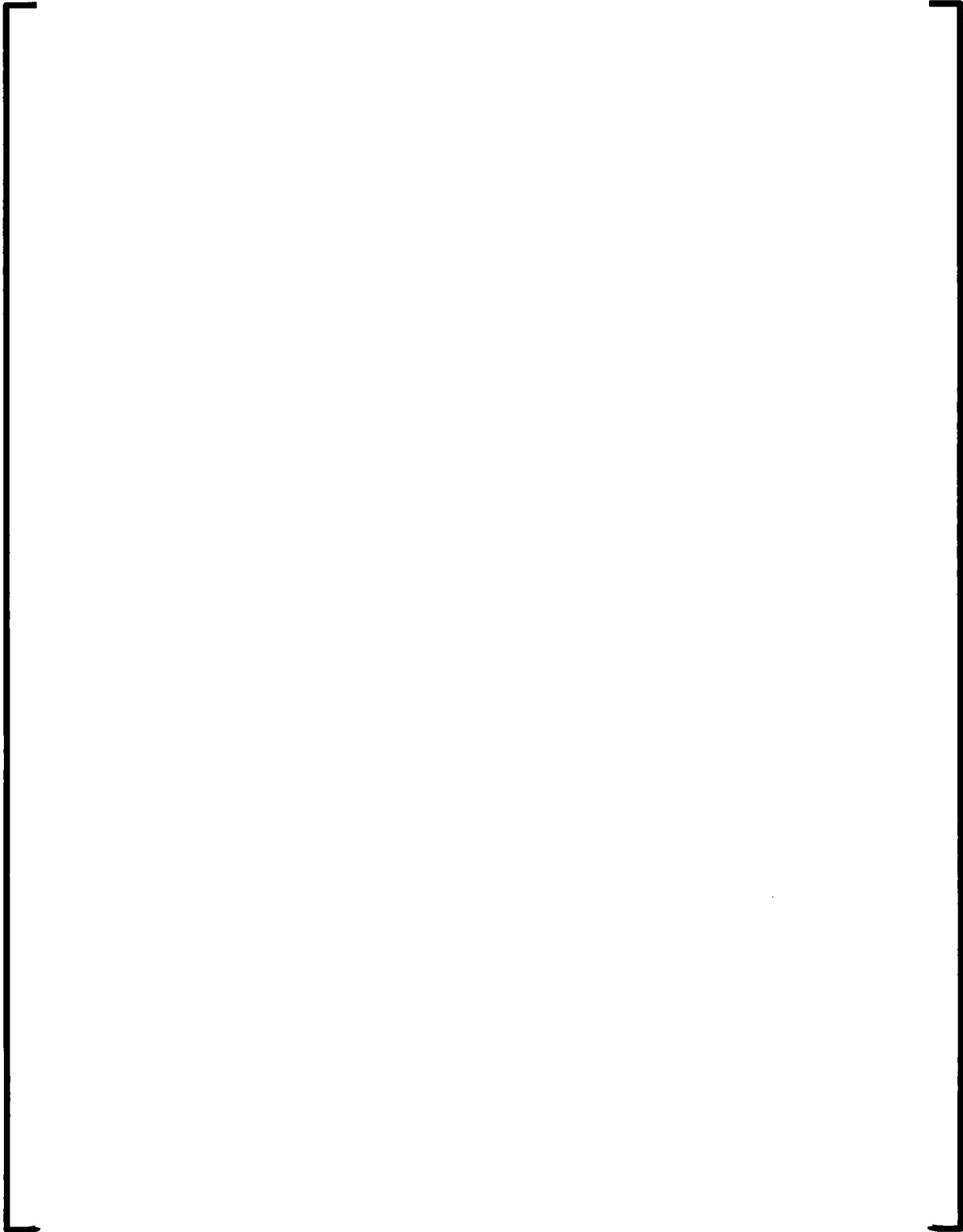


Figure 4-6—U.S. EPR Lateral Natural Frequency Test – Pulling System**4.1.1.2.3 U.S. EPR Fuel Assembly Lateral Dynamics Tests Summary**

Different tests were performed at various stages and on various test assemblies during the U.S. EPR development program, as indicated below:

- Beginning of Life (BOL) 2003 Lateral Stiffness Test – performed on an unirradiated 14 ft HTP fuel assembly. The assembly was a prototype called HTP-LX, and was close to the U.S. EPR configuration, but not exact. A comparison of the two designs is included in Table 4-2 and Table 4-3. The results were used primarily as a check on the validity of the model, and to validate the frequency sweep approach, which is described in more detail in Section 4.1.1.3.

- BOL 2003 Lateral Modal Analysis (forced vibration) – performed on an unirradiated 14 ft HTP fuel assembly. The test used the same HTP-LX assembly discussed in the previous paragraph. The forced vibration test was conducted using the constant energy, low varying frequency harmonic excitation, and the natural frequency was determined based on the minimum of the excitation force frequency response function.
- BOL 2003 Lateral Pluck Test with Impacts – performed on an unirradiated fuel assembly, the HTP-LX BOL prototype. The results are discussed in Section 4.1.5.1.
- EOL 2005 Lateral Stiffness Test – performed on an HTP-LX assembly in simulated irradiated condition.
- EOL 2012 Lateral Pluck Test and Modal Analysis (Forced Vibration) Test – performed on a simulated irradiated condition fuel assembly. The test assembly was a variation of the one used for the EOL 2005 lateral stiffness tests. The EOL 2012 tests were performed to demonstrate the equivalence between the pluck test and forced vibration lateral frequency results. These results will be used to justify the frequency sweep approach (Section 4.1.1.3).

The lateral stiffness test results for both the BOL 2003 and the EOL 2005 fuel assemblies are presented in Figure 4-7. From the loading/unloading curves presented, several conclusions can be formulated:

- [

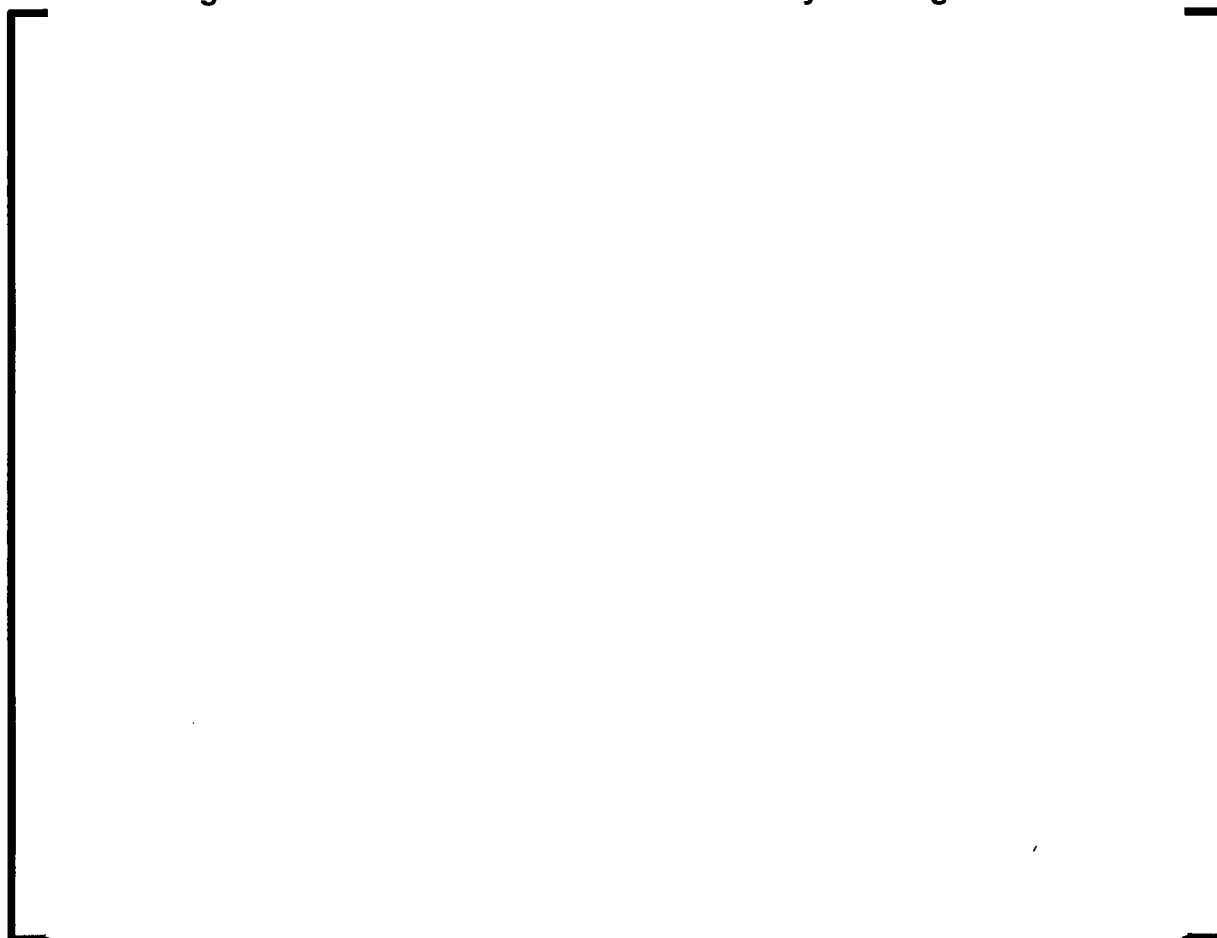
]

• []

[]

• []

Figure 4-7—U.S. EPR Lateral Fuel Assembly Loading Curves



The lateral frequency tests performed on the U.S. EPR fuel assemblies are summarized in Figure 4-8. The plot contains the BOL 2003 forced vibration data, and the EOL 2012 forced vibration, and pluck test data. The data support a few important conclusions and observations:

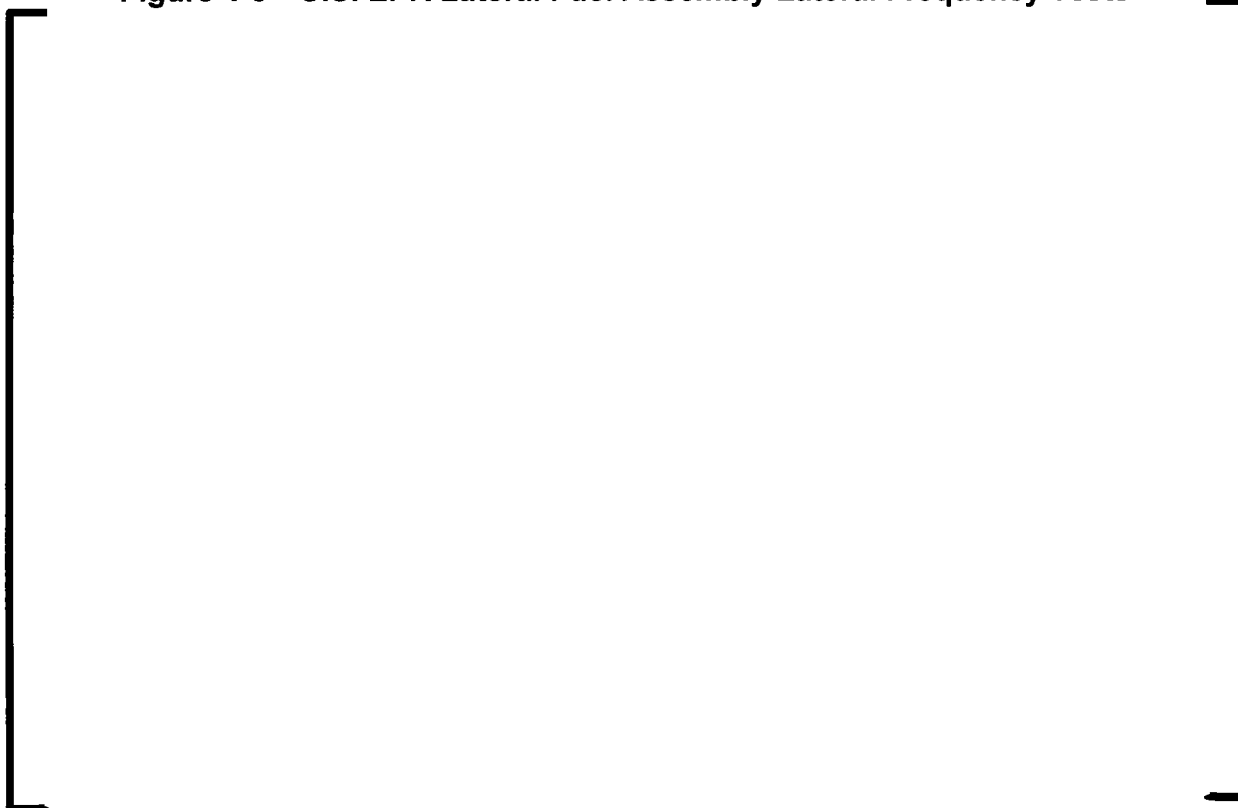
- As inferred from the lateral loading plots (Figure 4-7), the lateral natural frequency is a function of amplitude. In the case of the BOL 2003 assembly, this amplitude dependence is stronger than in the case of the EOL 2012 assembly. Also, the lateral frequencies of the unirradiated assembly (BOL 2003) are visibly higher than the frequencies of the simulated irradiated assembly (EOL 2012). For a vibration amplitude of [] the EOL 2012 natural frequency is [] than the BOL 2003 frequency, which is consistent with the extensive AREVA fuel assembly testing experience with HTP fuel assemblies (Section 4.1.1.3).
- To make the data directly comparable, the pluck vibration results were post-processed to produce the root mean square (RMS) of the displacement over the first pseudo-period, and then, the frequencies were reported for an RMS equivalent harmonic amplitude (obtained from the RMS by multiplication by $\sqrt{2}$). This is to account for the fact that the pluck test vibration is damped, and therefore, the oscillation never returns to the pluck amplitude. Consequently, reporting the frequencies at the pluck amplitude next to the forced vibration data would be inconsistent.
- Given the absence of a pluck test for the BOL 2003 fuel assembly, the EOL 2012 test helps establish the fact that the forced vibration and the pluck test data are equivalent, with the forced vibration data located inside a [] band from the pluck test data. Therefore, it is appropriate to use the forced vibration data from

the BOL 2003 test as the benchmark target for the U.S. EPR fuel assembly lateral model.

- Given that the BOL 2003 forced vibration data cover a restricted range of amplitudes, an analytical technique was implemented for the U.S. EPR seismic and LOCA analysis to account for the lateral frequency variability with amplitude. The technique involves sweeping the entire expected range of frequency variation with a set of linear fuel assembly models adjusted to various frequencies in the range, and using the limiting loads from this frequency sweep as final results (details discussed in Section 4.1.1.3).

The U.S. EPR lateral fuel assembly model benchmarking process and results are described in Section 4.1.1.2.4.

Figure 4-8—U.S. EPR Lateral Fuel Assembly Lateral Frequency Tests



4.1.1.2.4 U.S. EPR Fuel Assembly Lateral Model Test Benchmark

The U.S. EPR fuel assembly lateral single column model benchmarking process relies primarily on the test data obtained in the BOL 2003 test campaign (Section 4.1.1.2.3). However, those tests were performed on the HTP-LX, which is a slightly different fuel assembly, and has a few different features:

- Zirc-4 spacer grids, fuel rods and guide tubes, as opposed to M5[®] in U.S. EPR design.
- Presence of a central instrument tube instead of a fuel rod as in the U.S. EPR design.
- [] Trapper-type bottom nozzle instead of a [] FUELGUARD in the U.S. EPR design.
- Minor differences in grid span lengths, as can be seen by comparing the elevations in Figure 4-1 with the elevations in Figure 4-9.
- The two spacer grids closest to mid-span (labeled HTP 4 and HTP 5 in Figure 4-2) were of the same design as the rest of the grids in the assembly, as opposed to the final U.S. EPR design, where these grids have [] (Section 2.1).

The approach is to first construct the analytical model of the HTP-LX fuel assembly according to the detailed data presented in Table 4-2, by adjusting the intermediate spacer grid rotational stiffness, and then, keeping the grid rotational stiffness constant, to modify the model by changing the beam column properties according to the U.S. EPR detailed data presented in Table 4-3. The U.S. EPR two middle grids having a [] are located in the center of the fuel assembly, in a low rotation region, and therefore, the assumption of constant grid rotational stiffness is acceptable. The target frequency for mode 1 is measured at [] lateral deflection, according to the standard AREVA benchmarking procedure (Reference 2). The target frequency for

mode 3 was obtained by [

]

The results are summarized in Table 4-1.

Table 4-1—U.S. EPR Lateral Model Benchmark

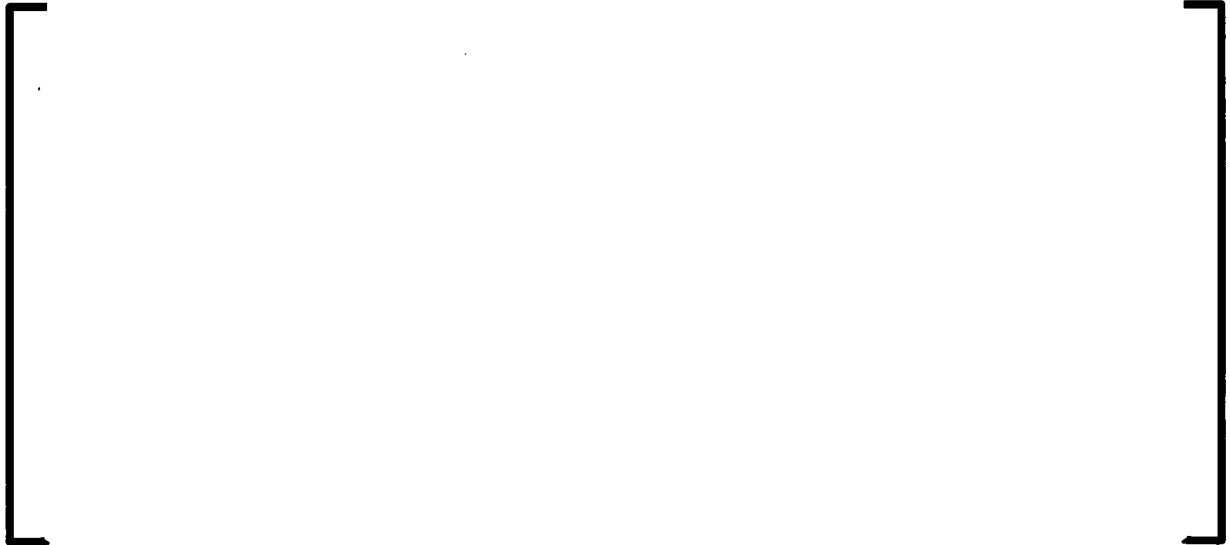
A large, empty rectangular frame with thick black lines, positioned centrally on the page. It is intended to contain the content of Table 4-1, but the table itself is not visible in this image.

Table 4-2—HTP-LX Features

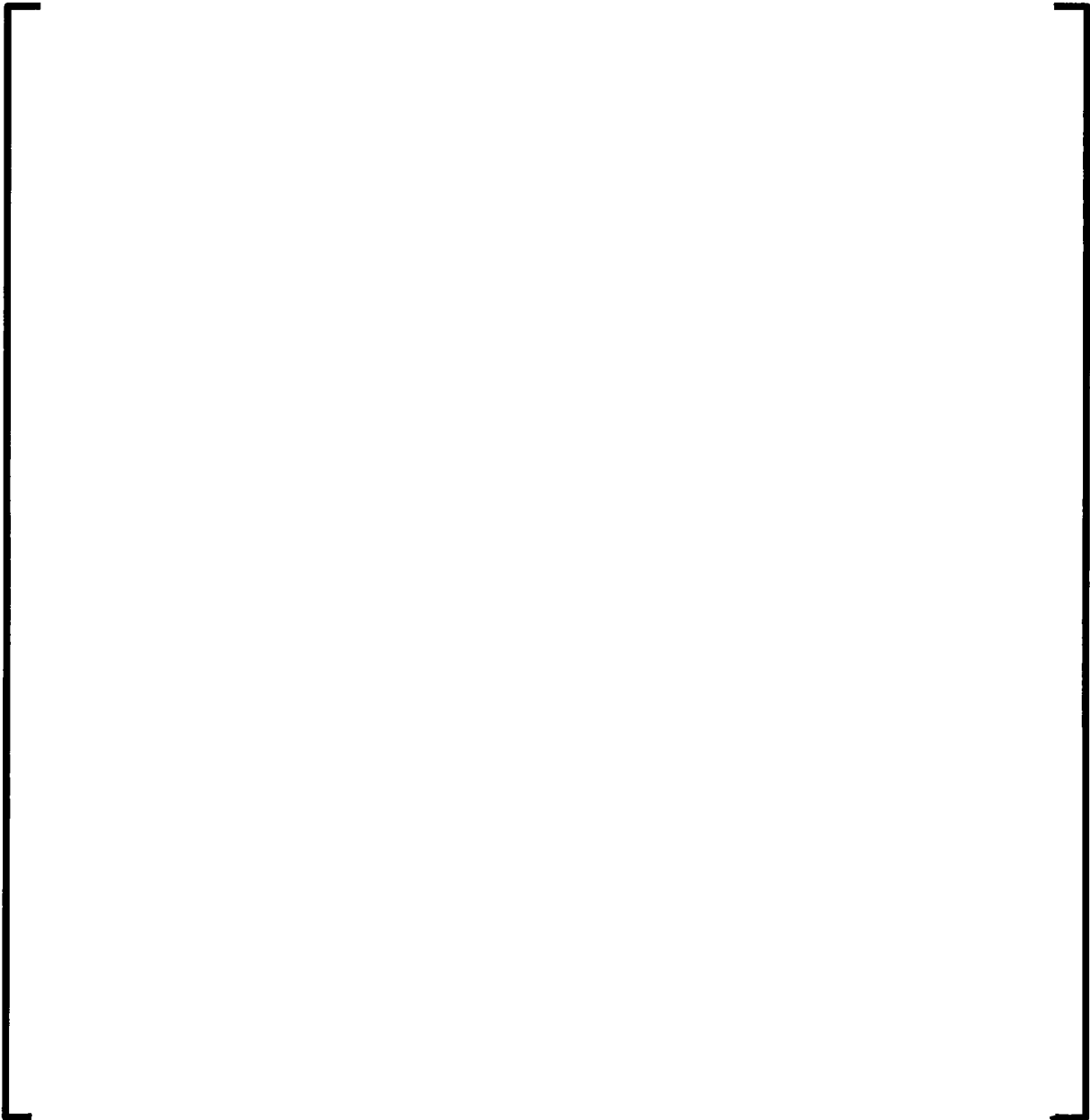
A large, empty rectangular frame with a thick black border, centered on the page. It is intended to contain the content of Table 4-2, but the content is currently blank.

Table 4-3—U.S. EPR Features

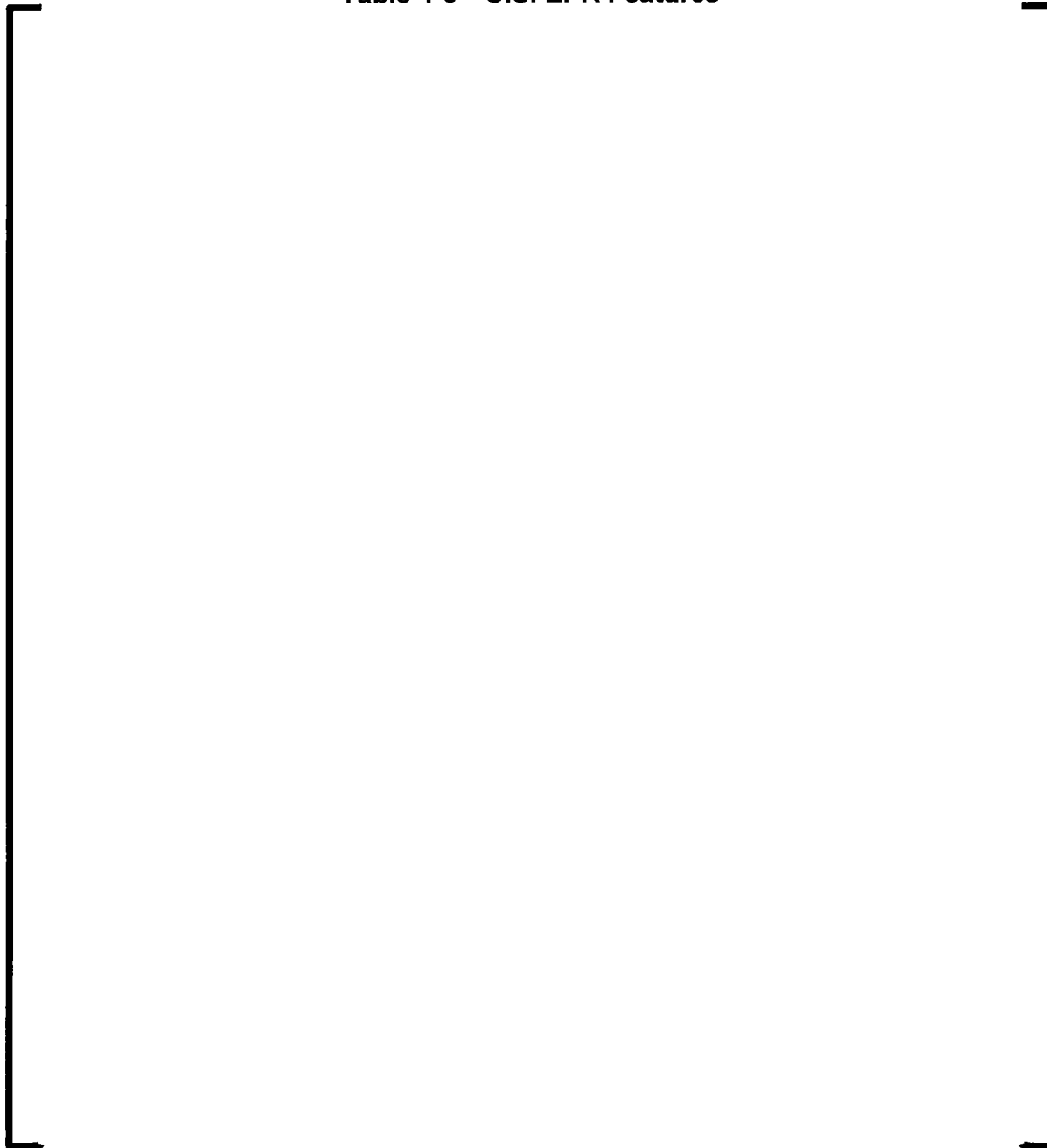
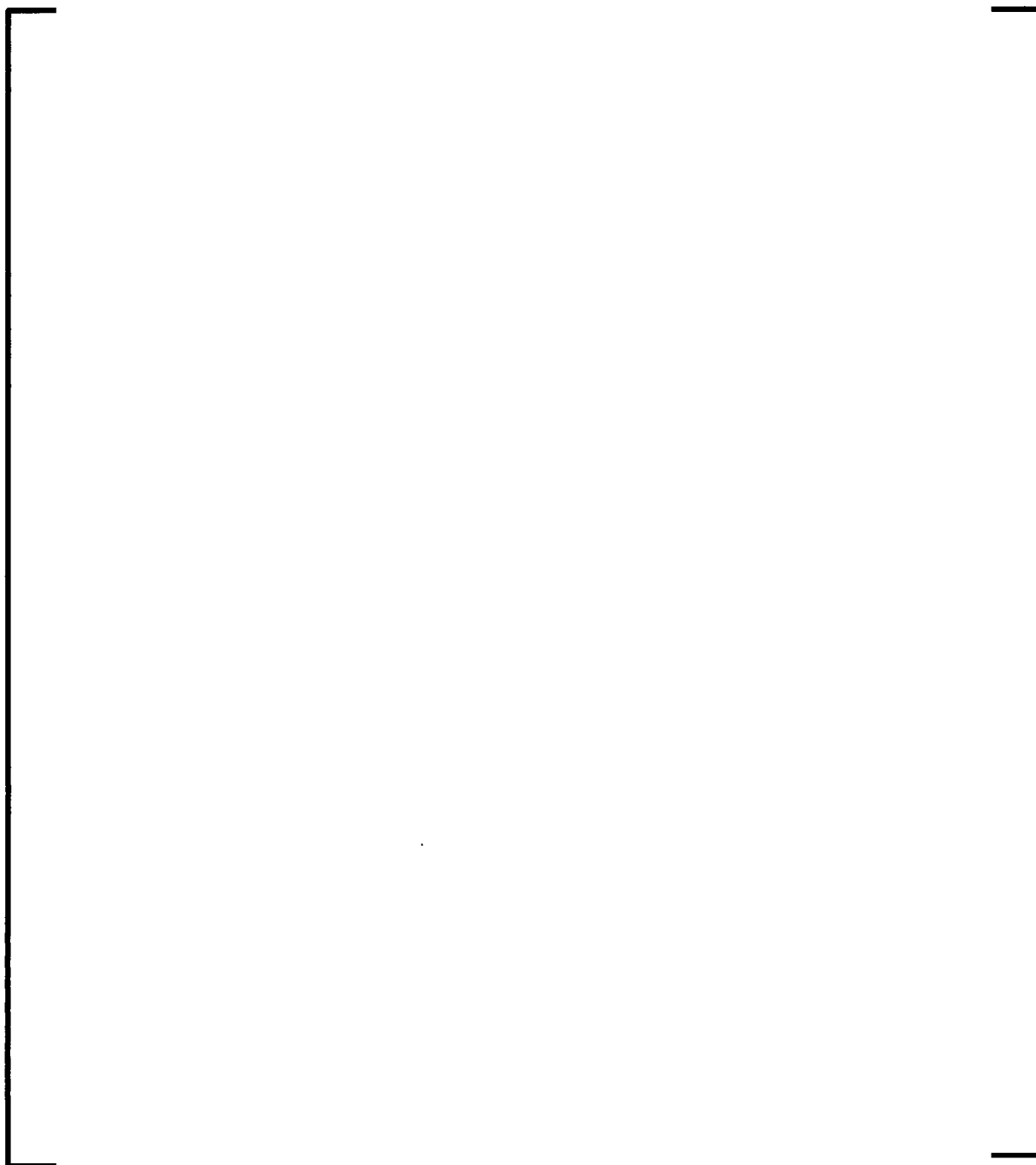
A large, empty rectangular frame with a thick black border, centered on the page. It is intended to contain the content of Table 4-3, but the content is not visible in this image.

Figure 4-9—HTP-LX Model Schematic

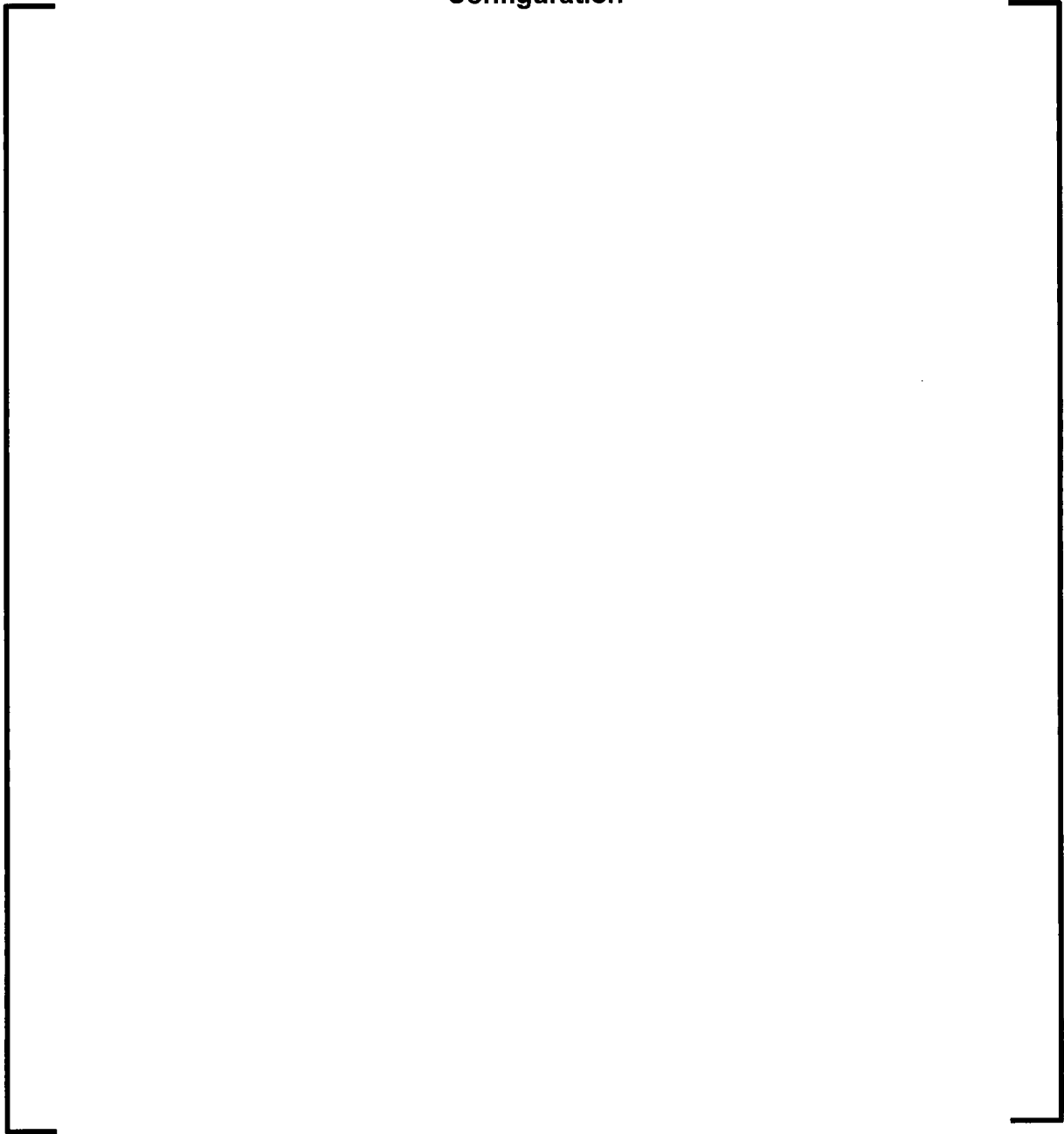


4.1.1.3 U.S. EPR Fuel Assembly Lateral Model - Frequency Sweep

In Section 4.1.1.2.3, it was mentioned that the test base for the unirradiated fuel assembly model (BOL 2003) consists only of the force vibration data, which cover only a portion of the expected range of amplitudes a fuel assembly could experience during a seismic event. Consequently, an analytical technique, referred to as the frequency sweep, addresses the fuel assembly change in lateral natural frequency due to the variations in amplitude and effects of irradiation.

The essence of the frequency sweep approach is to define a set of fuel assembly lateral models with natural frequencies covering a range of expected values, and then analyzing each of these scenarios. The bounding component loads from all these cases will be used to qualify the fuel assembly for service. The fuel assembly natural frequency change is due to a change in lateral stiffness, which is introduced by the non-linear nature of the fuel rod to spacer grid cell interaction. However, due to the fact that the U.S. EPR grids operate well below the point of instability on the spacer grid loading curve (more details are discussed in Section 4.1.4), this change in stiffness of the fuel assembly, with respect to amplitude, can be addressed as a parameter variation without the need to implement a full non-linear model of the bundle. The point is illustrated schematically in Figure 4-10, which shows the two extreme cases a peripheral fuel assembly goes through in the course of a seismic event. The maximum lateral deflection case, where all fuel assemblies in the core are displaced away from the heavy reflector, is at one extreme. This is the position of maximum potential energy for the fuel assembly. This potential energy will be transferred into kinetic energy at the other extreme of the range, where the peripheral fuel assembly impacts the heavy reflector. In this state, the deflection on the fuel assembly is small, and the kinetic energy is transferred in the impact with the heavy reflector.

Figure 4-10—Maximum Deflection versus Maximum Impact Configuration



To accurately predict the maximum grid impact load, the model must be able to correctly capture the potential energy in the maximum deflected configuration, and to correctly transfer this energy into kinetic energy at the maximum impact configuration. The actual path, linear or not, for this energy transfer is a secondary effect, which would

become important if predicting spacer grid loads beyond the buckling limit. This is the reason why a parametric study on a set of linear fuel assembly models will be able to capture the maximum grid impact loads with reasonable accuracy. This conclusion is also formulated in "Review of LWR Fuel System Mechanical Response with Recommendations for Component Acceptance Criteria" (Reference 12), and has been the basis for the long standing industry practice of using linear models for the fuel assembly.

The response to Request for Additional Information (RAI) Number 64 (Reference 7) contains a comparison of the U.S. EPR fuel assembly characteristics and dynamic response with previous AREVA designs. The U.S. EPR fuel assembly dynamic characteristics are shown to be similar to previous 12-ft AREVA fuel assemblies when scaled by assembly length. Additionally, the dynamic response is similar when assessed on a uniform loading basis. These observations, together with the fact that the U.S. EPR grids have substantial margin to the allowable crushing load, indicate that the linear bundle model is applicable to the U.S. EPR fuel assembly.

The non-grid component stress or load evaluations are also based on this approach, whereby the deflected fuel assembly shape at critical times during the loading time history is applied as input on a detailed non-linear finite element model (FEM) to produce component loads/stresses (discussed in detail in Section 4.3).

In order to decide the range of the frequency sweep to be used for the U.S. EPR analysis, one must review the previous testing experience of the AREVA HTP product line. The mode 1 frequency data for a number of AREVA HTP fuel designs are plotted in Figure 4-11, and support several conclusions:

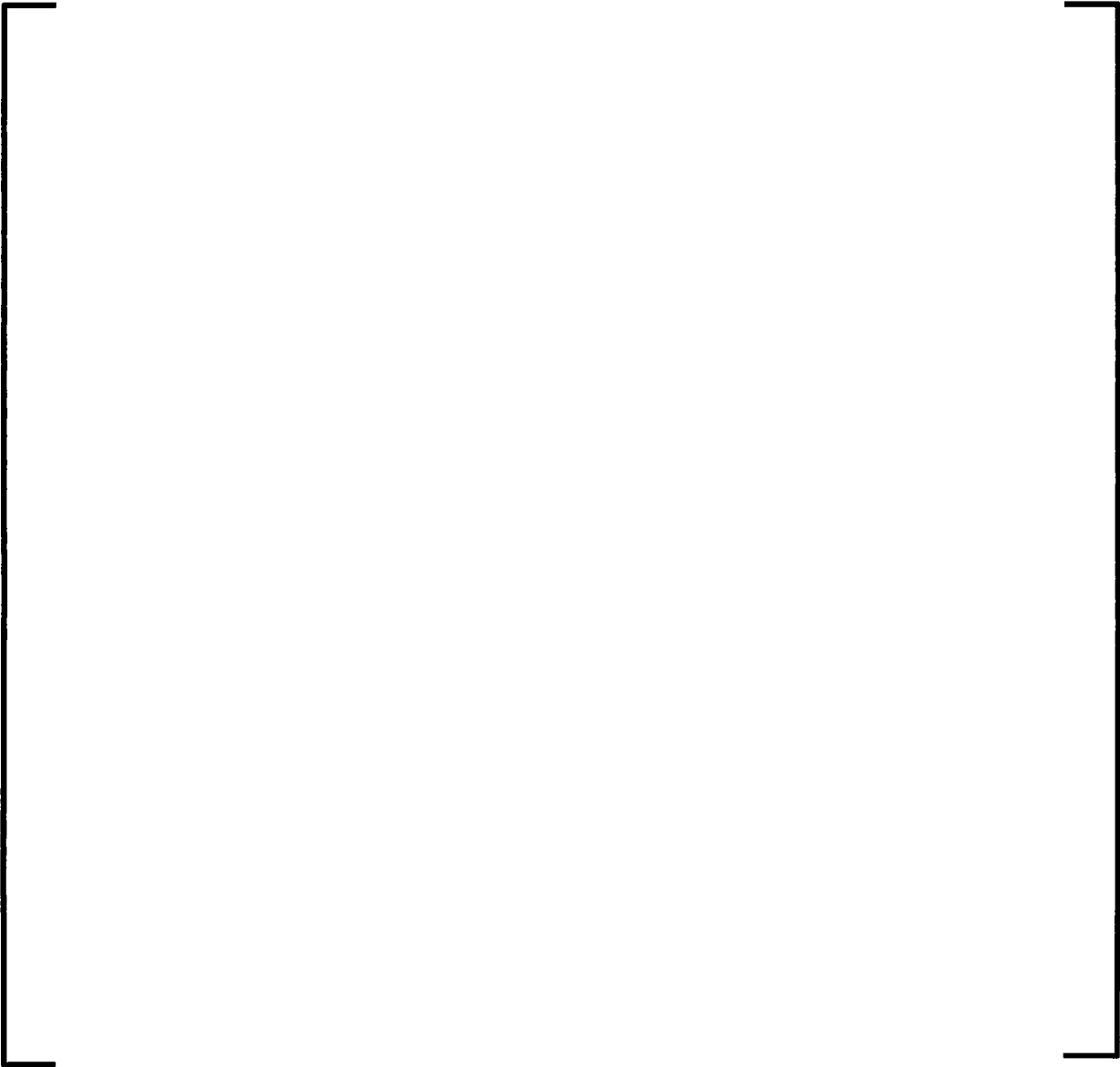
- [

]

• [

]

Figure 4-11—HTP Fuel Designs – Frequency versus Amplitude



The next comparison is shown in Figure 4-13, where the percent variation of the simulated irradiated condition is plotted versus the standard benchmark at [] in unirradiated condition. This shows that a simulated irradiated HTP assembly can have lateral natural frequencies as low as [] from the BOL natural frequency at [] deflection. This is consistent with the comparison between simulated irradiated and unirradiated lateral frequencies shown in Section 4.1.1.2.3.

Figure 4-13—Frequency Percent Drop from BOL Benchmark at [] to EOL



Taking into account the conclusions from Figure 4-12 and Figure 4-13, a frequency sweep range of [] is defined for the U.S. EPR fuel assembly, which

accounts for all possible frequency variability for both the effect of vibration amplitude, and the effect of irradiation. It must be pointed out that this frequency sweep range is very conservative. On the high frequency side, the [] limit is conservative because it is associated with a very small amplitude of vibration, which is inconsistent with high impact spacer grid or component loads. At the low frequency end of the range, the [] limit is conservative because it exceeds the measured frequency difference between the BOL 2003 and EOL 2012 tests (Section 4.1.1.2.3).

To further validate the frequency sweep range, a different comparison of the U.S. EPR frequency data with the other AREVA HTP designs is shown in Figure 4-14. The comparison is based on a uniform frequency parameter defined below. The natural frequency of any beam in bending depends on the beam physical characteristics and the support conditions. The general equation is:

$$\omega_k = (\lambda_k)^2 \sqrt{\frac{EI}{mL^4}} \quad \text{Equation 4-3}$$

where ω_k is the circular natural frequency, E is Young's Modulus, I is the section inertia (calculated as the simple sum of the slender component inertias), m is the mass per unit length, L is the span length, and λ_k is the corresponding root of the characteristic equation, which depends only on the support conditions, and not on the beam characteristics. By plotting the natural frequency of various fuel assemblies against the uniform frequency parameter, $\sqrt{(EI)/(mL^4)}$, a consistent comparison of various fuel designs can be formulated. The comparison, shown in Figure 4-14, indicates that all the AREVA HTP assemblies are dynamically equivalent, as demonstrated by the fact that all designs follow a linear trend, with predictable differences in frequency stemming from the range of particular physical characteristics. The stiffening effect of the HTP spacer grid, over and above the intrinsic stiffness of the slender components of the fuel assembly, is the same, on a percentage basis, for all the designs.

The main conclusion for the U.S. EPR fuel assembly accident analysis is that any estimates or trends derived on a percent basis from previous AREVA HTP designs carry over, on a percent basis, to the U.S. EPR. Thus, the definition of the frequency sweep range in terms of percentage frequency is applicable. It is also worth mentioning that the transferability of percentage differences applies only to the frequency data, which is linear with respect to the uniform frequency parameter $\sqrt{(EI)/(mL^4)}$. This is why it is given the name "frequency sweep," when, in reality, it is the assembly stiffness that changes.

Figure 4-14—HTP Design Family Dynamic Similarity



An additional justification for the acceptability of the frequency sweep range is to compare the lateral stiffness plots of the unirradiated and simulated irradiated fuel assembly data to the lateral stiffness of the fuel assembly models included in the frequency sweep. The loading curves for the BOL 2003 and EOL 2005 lateral stiffness tests were plotted over the analytical loading curves of the linear models that form the frequency sweep. The BOL 2003 plot is shown in Figure 4-15. The data also includes an elastic loading curve, which is obtained from the total loading curve by subtracting half of the hysteresis value, and represents the true strain energy storage capability of the fuel assembly. The remaining energy is dissipated by the friction forces.

[

]

Figure 4-15—U.S. EPR BOL Lateral Loading Curve versus Frequency Sweep Models



The similar lateral loading plot for the EOL 2005 and EOL 2012 tests is shown in Figure 4-16. [

]

Figure 4-16—U.S. EPR EOL Lateral Loading Curve versus Frequency Sweep Models



The actual construction of the frequency sweep models is obtained from the standard benchmark model (based on the BOL 2003 test, and discussed in Section 4.1.1.2.4) by modifying the stiffness of the rotational spring elements at the spacer grids. The details of the rotational stiffness values and the natural frequencies are presented in Section 4.1.5.

4.1.2 U.S. EPR Fuel Assembly Lateral Model – Hydrodynamic Coupling

This section describes the hydrodynamic coupling elements used in the U.S EPR lateral analysis methodology. The definition of these elements follows the standard AREVA lateral analysis methodology in Addendum 1 of Reference 2.

The hydrodynamic coupling between the structure and the fluid described in this section concentrates on the interaction between the lateral motion of the fuel assembly and the lateral motion of the fluid, and the lateral forces imparted through the fluid by the lateral accelerations of the reactor vessel. Since the theoretical details have not changed from those presented in Addendum 1 of Reference 2, this section focuses is on the implementation of this technique to the U.S. EPR fuel assembly.

The hydraulic coupling element models two physical phenomena:

- The added kinetic energy contained in the fluid, as the fuel bundle moves laterally. When the fuel rods and guide tubes move laterally with a given speed, the surrounding water must move in the opposite direction and fill the void. This creates a partitioning of the kinetic energy between the moving hardware, and the coolant water. To maintain the balance between the maximum strain energy and the kinetic energy of the fuel assembly, the kinetic energy of the cooling water must be taken into account by reducing it to the degree of freedom of the fuel assembly in the form of the “added mass.” Since the motion of the fluid involves increased flow velocity between the fuel rods, and since the added mass is introduced on a slower moving degree of freedom for the purposes of matching kinetic energy, it is not uncommon for the added mass to be a multiple of the physically available water mass.

- The other effect modeled by the hydrodynamic coupling element is the lateral buoyancy force resulting from the lateral acceleration of the reactor internals. When a structure is submerged in a fluid, in a gravitational field, the net fluid force is equal and opposite to the weight of the displaced fluid. The same phenomenon occurs if the acceleration is in the lateral direction. In this case, the fluid will exert a force on the structure equal in magnitude to the mass of the displaced fluid times the lateral acceleration of the vessel, and acting in the opposite direction of the acceleration.

The hydrodynamic element captures these two effects in the form of a mass matrix element, which augments the mass matrix of the structure. The element equation is:

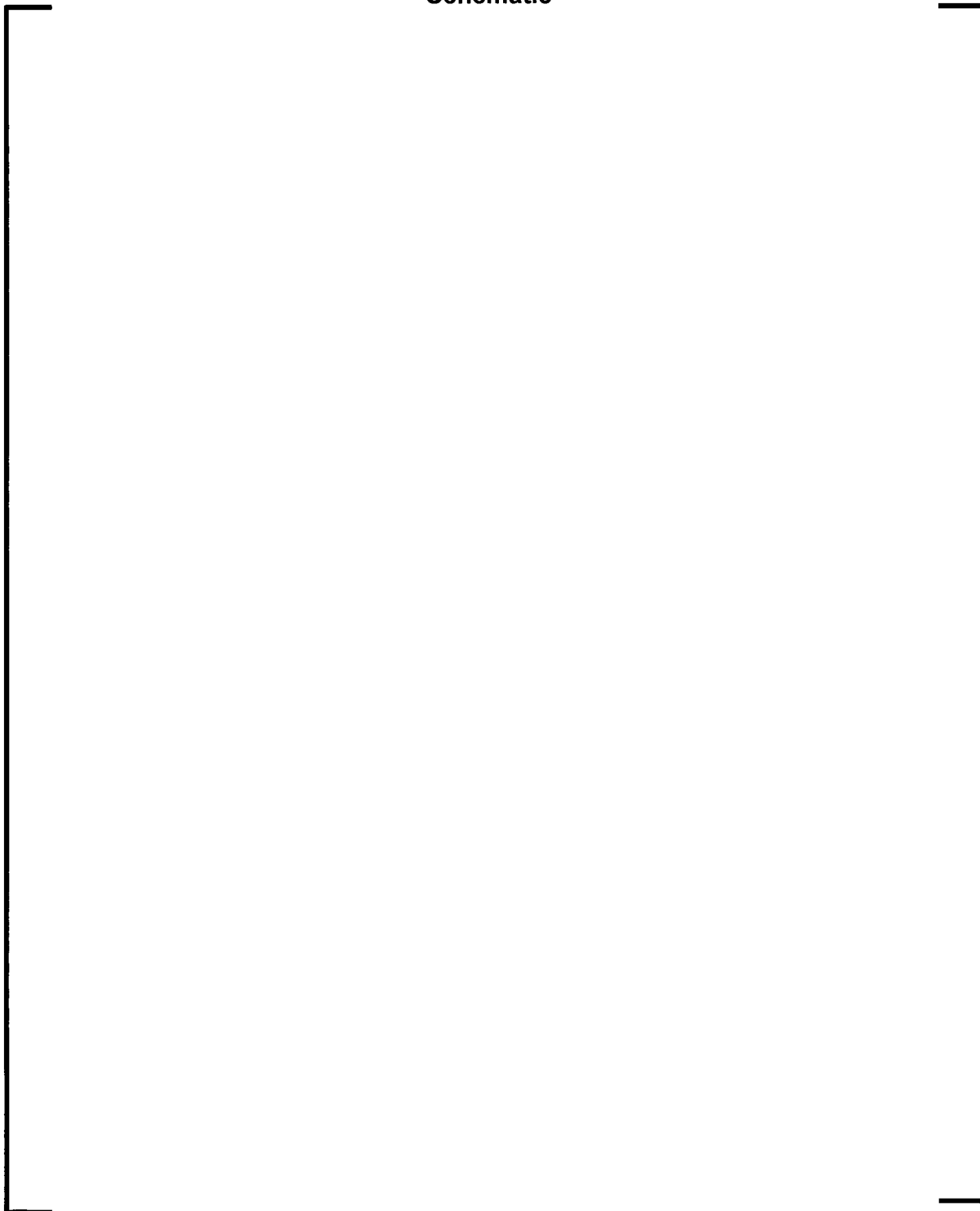
$$M = \begin{bmatrix} m_a & m_c \\ m_c & m_a \end{bmatrix} \quad \text{Equation 4-4}$$

The elements are defined at every spacer grid elevation, between the spacer grid node lateral degree of freedom, x_f , and the corresponding heavy reflector node lateral degree of freedom x_b (according to Figure 4-17). The m_a and m_c quantities represent the added mass and the coupling mass respectively.

The added mass is calculated as [] times the displaced water mass at reactor operating conditions, and is assigned so that one element groups half the mass displaced by each of the two adjacent spans (according to Addendum 1 of Reference 2). This multiplier was derived for a 17x17 lattice, and applies to the U.S. EPR fuel assembly.

The coupling mass is derived so that upon the application of a uniform lateral acceleration, and under relative equilibrium, the net body force applied on the fuel assembly degree of freedom is the negative of the displaced water mass times the acceleration. The multiplier for the coupling mass is, therefore, [], as indicated in Addendum 1 of Reference 2.

**Figure 4-17—U.S. EPR Hydrodynamic Coupling Elements –
Schematic**



4.1.3 U.S. EPR Fuel Assembly Lateral Model – Damping

This section discusses the damping phenomena associated with the lateral motion of the fuel assembly. For the purposes of the U.S. EPR analytical models, all damping forms will be treated as a viscous equivalent, meaning that the model assigns a damping force proportional to the lateral generalized velocity vector. The methodology relies on the established and approved AREVA unirradiated fuel assembly damping values, and implementation using the Rayleigh method, as described in Addendum 2 of Reference 2. However, for the U.S. EPR fuel assembly the method had to be refined to some degree in order to allow for the implementation of a consistent damping mechanism for all the cases included in the frequency sweep approach (Section 4.1.1.3), so that the model can reflect both unirradiated and irradiated condition damping.

There are three general sources of energy dissipation associated with the lateral motion of a fuel assembly:

- Structural damping is caused by the internal friction at the fuel rod spacer grid interface. The damping coefficient is a function of grid cells spring load which, in turn, is a function of bundle condition irradiated versus unirradiated.
- Viscous water damping is caused by the irrecoverable pressure losses that occur as the fuel rod lattice moves through water and the water is forced to accelerate and decelerate through the bundle.
- Axial coolant flow damping is caused by the hydrofoil effect associated with the axial flow rate and the lateral motion of the fuel assembly.

The various forms of damping are summarized in Table 4-4.

Table 4-4—Fuel Assembly Damping Sources**4.1.3.1 U.S. EPR Fuel Assembly - Structural Damping**

The structural damping in a fuel assembly is a result of the interaction between the fuel rods and the spacer grid cells. As the assembly bends laterally, the relative axial and rotational displacements between the fuel rods and the spacer grids dissipate energy. The dissipation of energy reduced to an equivalent viscous damping (for ease of implementation in the fuel assembly model), and expressed as critical damping ratio is plotted in Figure 4-18, for a range of AREVA HTP fuel designs. The data includes the EOL 2012 tests, but does not include the BOL 2003 tests. The reason for this is that the BOL 2003 tests were forced vibration tests, and the technique used was to detect the minimum of the excitation force frequency response function, which does not produce damping information. All data reflects in-air, ambient temperature test conditions. The data supports a few conclusions:

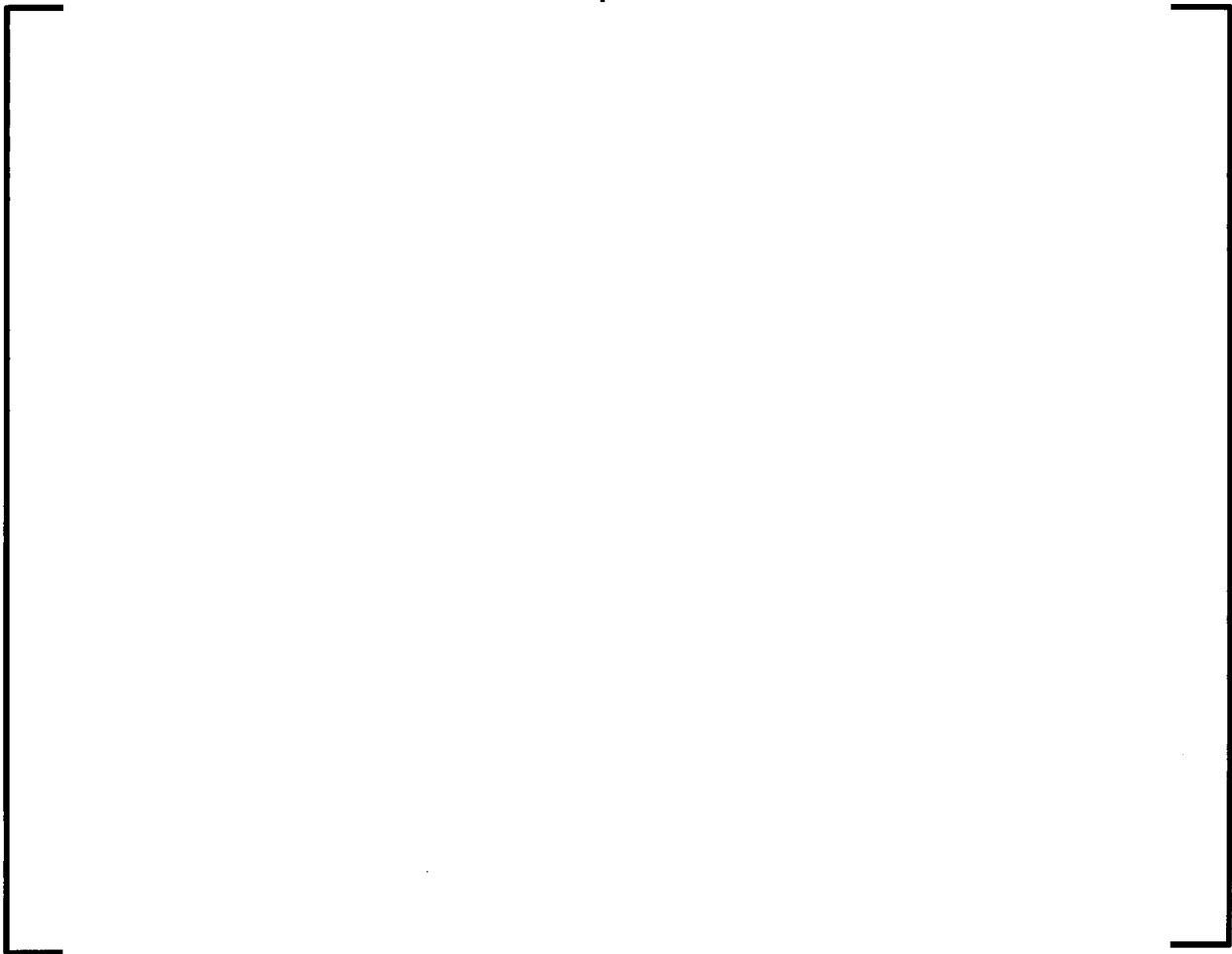
- [

]

• [

] The value is clearly supported by the test data, and is in line with the default damping values specified in USNRC Regulatory Guide 1.61 (Reference 9).

Figure 4-18—HTP Fuel Assembly Structural Damping versus Amplitude



4.1.3.2 U.S. EPR Fuel Assembly – Coolant Induced Damping Test Base

This section contains more details on the damping mechanisms resulting from the interaction of the fuel assembly with the reactor coolant. As indicated in Table 4-4, the coolant induced damping has two dissipation mechanisms:

1. The irrecoverable pressure loss associated with the lateral relative motion of the fuel through the coolant.
2. The hydrofoil effect produced by the axial flow of coolant.

The strength of the two damping mechanisms is determined by tests performed on full scale assemblies that are subjected to realistic flow conditions, and to lateral forced excitation. The test data supporting the U.S. EPR damping model comes from two test campaigns:

MASSE 99 (1999)

- These tests form the basis of the standard AREVA methodology in Addendum 2 of Reference 2. The test program involved three stages: the first stage consisted of pluck tests in [] at various flow rates, the second stage consisted of pluck tests in water at various flow rates over a [], and the third stage consisted of sine sweep forced displacements applied at [] water at various flow rates.
- The tests were performed on a [] fuel assembly in unirradiated condition.
- The fuel assembly natural frequency in air was measured at [] lateral displacement amplitude. The unirradiated U.S. EPR fuel assembly has a natural frequency of [] lateral displacement, which makes the two assemblies very similar from a dynamic point

of view. In addition, the geometric characteristics (e.g., rod diameter, rod pitch, lattice array, span and assembly height) are very similar. Therefore, the hydraulic damping information from the tests is representative of the U.S. EPR, as the only significant difference in design is the spacer grid type. The spacer grid differences would primarily affect structural damping, which as discussed in Section 4.1.3.1, is defined based on a conservative lower bound.

- The average bundle flow velocities used for the test were: [.] Given that the U.S. EPR average bundle flow rate is [], the test data constitutes a lower bound for the actual axial coolant flow induced damping at full flow rate.
- The test results discussed in this report are the sine sweep imposed displacement at []. The actuation force and displacement data were post-processed by the half-power Q method for lower damping values, and by the circle-fit method for high damping values.

CAMEOL (2004)

- The tests were performed on a [] fuel assembly in simulated irradiated condition. The assembly was tested in [].
- The fuel assembly natural frequency in air was measured at [] lateral displacement amplitude. This frequency is [] than the unirradiated condition, which is consistent with the test results discussed in Section 4.1.1.2.3, and the frequency sweep range defined in Section 4.1.1.3. The U.S. EPR in simulated irradiated condition (Figure 4-8) has a natural frequency of [] lateral displacement, which makes the two assemblies very similar from a dynamic point of view. In addition, the

geometric characteristics (e.g., rod diameter, rod pitch, lattice array, span and assembly height) are very similar. Therefore, the hydraulic damping information from the tests is representative of the U.S. EPR, as the only significant difference in design is the spacer grid type. The spacer grid differences would primarily affect structural damping, which as discussed in Section 4.1.3.1, is defined based on a conservative lower bound.

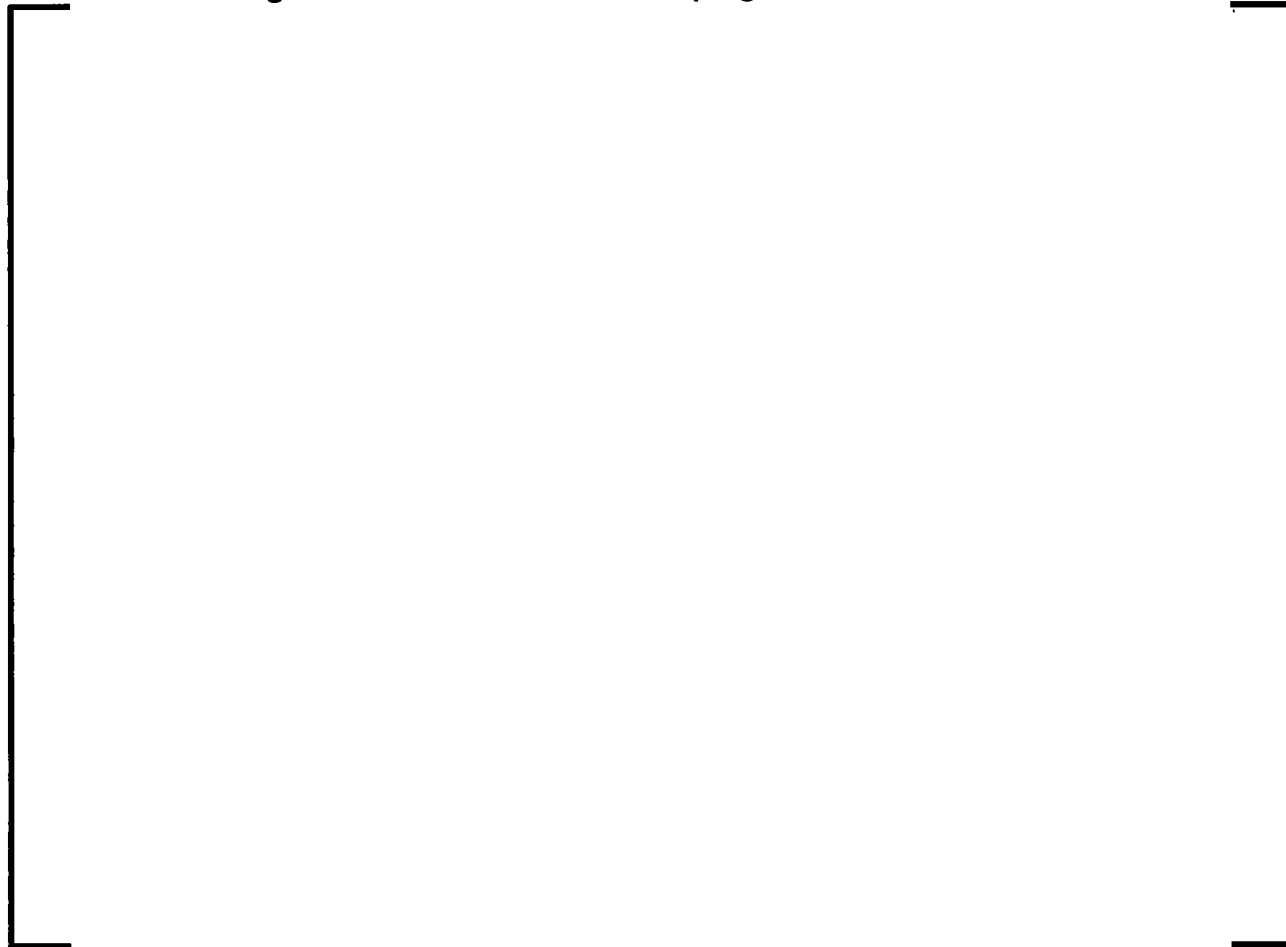
- The average bundle flow velocities used for the test were: [
] which bounds the U.S. EPR average bundle flow rate of
 [].
- The test consisted of applying a forced sinusoidal displacement at one of the center grids, and recording the applied force versus time. The data was post-processed by the half-power Q method for lower damping values, and by the circle-fit method for high damping values.

4.1.3.3 U.S. EPR Fuel Assembly Un-Irradiated Condition Damping

The unirradiated condition damping model for the U.S. EPR fuel assembly maintains the overall damping ratio in the standard AREVA methodology in Addendum 2 of Reference 2. In addition, the implementation of the damping model via the Rayleigh mass and stiffness coefficients is maintained. However, the partition between the mass proportional and stiffness proportional damping is modified to accommodate the fuel assembly natural frequency variation included in the frequency sweep approach.

The first part of this section discusses the test base and the conservatism incorporated in the standard method. The test base for the standard method is represented by the MASSE 99 tests (Section 4.1.3.2). A plot of the fuel assembly damping ratio obtained from these tests under various environments (air and water at various flow rates) is shown in Figure 4-19.

Figure 4-19—Unirradiated Damping Ratio Measurements



The damping ratio data from the MASSE 99 tests supports a few important conclusions:

- [

]

• [

]

• [

]

Further analytical investigations show that:

• [

]

• [

]

The second MASSE test phase demonstrated the effect of [

]

Figure 4-20—Effect of Temperature on Fuel Assembly Damping



Based on the test results discussed in the previous paragraphs, the extrapolation of the ambient temperature results to in-reactor conditions is performed differently for the hydraulic and the structural damping terms, as follows:

- [

]

All the preceding considerations can be grouped in the following scaling equation:

$$\zeta_{hot} = K_E (\zeta_{test-structural} + K_{density} \cdot \zeta_{test-hydraulic}) \quad \text{Equation 4-5}$$

Applying these scaling factors to the still water damping and axial coolant flow damping ratios in Figure 4-19, and to the overall elastic modulus scaling factor, the in-reactor scaled damping ratio at an amplitude of [] The value used in the U.S. EPR fuel assembly analysis, and in the AREVA standard methodology (Addendum 2 of Reference 2) is [] which shows that the methodology conservatively underestimates the in-reactor damping effects.

In terms of actual implementation, for the U.S. EPR, the unirradiated overall damping ratio of [] is maintained, but it is partitioned [] as mass proportional

damping, and β as stiffness proportional damping (shown to be conservative in the preceding section). The reason and merits for this approach will be discussed in further detail in Section 4.1.3.4 . The numerical implementation relies on defining the Rayleigh coefficients , α , and β , so that the mass proportional damping results in a ζ damping ratio, and the stiffness proportional damping amounts to amounts to a ζ damping ratio:

$$\left[\begin{matrix} \dots \\ \dots \end{matrix} \right] \tag{Equation 4-6}$$

In the Equation 4-6, f_i represents the operating temperature mode 1 natural frequency of the fuel assembly.

4.1.3.4 U.S. EPR Fuel Assembly Irradiated Condition Damping

This section discusses the irradiated condition damping model for the U.S. EPR fuel assembly.

During a lateral pluck test, the fuel assembly motion is dominated by the mode 1 response. For illustration purposes, a one-degree-of-freedom (1-DOF) system will suffice. The equation of motion for the free vibration of a 1-DOF system under initial displacement conditions is:

$$\begin{aligned} M\ddot{x} + C\dot{x} + Kx &= 0 \\ x(0) &= X_0 \\ \dot{x}(0) &= 0 \end{aligned} \tag{Equation 4-7}$$

The M , C , and K notations signify mass, damping, and stiffness, respectively. The solution can be expressed in the traditional form, in terms of the natural frequency, and the critical damping ratio, as:

$$x(t) = \frac{X_0}{\sqrt{1 - \zeta^2}} e^{-\zeta\omega t} \cos(\omega\sqrt{1 - \zeta^2}t - \varphi) \quad \text{Equation 4-8}$$

Where:

$$\omega = \sqrt{\frac{K}{M}} \quad \text{Equation 4-9}$$

And:

$$\zeta = \frac{C}{2\sqrt{KM}} \quad \text{Equation 4-10}$$

The ensuing oscillation described by Equation 4-8 is a damped harmonic response, with the motion decay envelope, given by $\exp(-\zeta\omega t)$. This expression shows that the motion decay is controlled by the product of the natural frequency and the critical damping ratio, but beyond this, it is difficult to capture the actual effect of the physical system parameters. To obtain a better understanding of the nature of the motion decay envelope, it is useful to rewrite the response in Equation 4-8, in terms of the physical constants of the system as:

$$x(t) = \frac{X_0}{\sqrt{1 - \frac{C^2}{4KM}}} e^{-\frac{C}{2M}t} \cos\left(\sqrt{\frac{K}{M} - \frac{C^2}{4M^2}}t - \varphi\right) \quad \text{Equation 4-11}$$

In this new form, the motion decay envelope is controlled by the damping coefficient, and the system mass. Additionally, it can be seen that the damping coefficient, C , has a direct effect, by making the decay steeper, while the mass, M , has an inverse effect, causing a slower motion decay. The important fact to notice is that the motion decay envelope does not depend on the system stiffness. This implies that two systems with the same damping coefficient and mass will have the same decay envelope. The

graphical illustration of this point is presented in Figure 4-21, where a 1-DOF system with a frequency of [] is plotted together with a 1-DOF system with a frequency of [], the mass and damping coefficient of the two systems being the same. The two systems are selected to be representative of the U.S. EPR assembly unirradiated and irradiated condition respectively. The damping coefficient was selected so that the unirradiated system has a damping ratio of [] This choice of constants produces a damping ratio of [] for the irradiated case. However, the two motion decay envelope curves are practically identical, except for a minor difference which manifests itself in the early stages of motion, but becomes inconsequential after one pseudo-period.

Figure 4-21—1-DOF System – Motion Decay Envelope



The preceding remarks are applicable to the dynamics of a fuel assembly in lateral motion. The only parameter that changes throughout the service life of a fuel assembly is the lateral stiffness resulting from the relaxation of the spacer grid cells. The mass of the assembly stays constant, and so does the damping coefficient associated with the hydrodynamic effects (both still water and coolant flow induced). This is because these effects are primarily a function of the fuel assembly general geometry, which does not change over the service life of the assembly. The consequence is that the pluck test response motion at any point in the service life of a fuel assembly would stay within the same decay envelope.

For the U.S. EPR model, the damping model will be defined in a way that preserves the same motion decay envelope. [

]

By applying this method, which preserves the strength of the energy dissipation mechanisms as the fuel assembly stiffness decreases under the effects of irradiation, the damping ratio of the irradiated fuel assembly increases (see Equation 4-11).

To further confirm the validity of the proposed damping formulation, a review of the damping test data in the simulated irradiated condition is in order. The tests were part of the CAMEOL 2004 campaign discussed in Section 4.1.3.2. A plot of the fuel assembly mode 1 damping ratio obtained from these tests under various environments (air and water at various flow rates) is shown in Figure 4-22.

Figure 4-22—Simulated Irradiated Damping Ratio Measurements



The damping ratio data from the CAMEOL 2004 tests supports a few important conclusions:

- [

•

]

The extrapolation of the ambient temperature results to in-reactor conditions is performed in same manner as in the unirradiated case discussed in Section 4.1.3.3.

[

], which is consistent with the

expected damping ratio values discussed in previous paragraphs in this section.

The damping model described in the preceding discussion is extended over all the cases of the frequency sweep approach. As the bundle natural frequency changes, the damping ratio changes as well as indicated in Equation 4-12, where α and β are defined in Equation 4-6.

$$\zeta = \frac{\alpha}{4\pi \cdot f_1} + \beta\pi \cdot f_1$$

Equation 4-12

As the bundle frequency [

]

4.1.3.5 U.S. EPR Fuel Assembly Damping - Summary

To summarize, the fuel assembly damping model used for the U.S. EPR seismic and LOCA analysis is an extension of the AREVA methodology presented in Addendum 2 of Reference 2. The main characteristics are summarized as follows:

Unirradiated Condition Damping Model:

- [

]

Irradiated Condition Damping Model:

- [

]

Sources of Conservatism Not Credited in the Damping Model:

- [

]

- The flow induced damping is not credited for LOCA analysis.

4.1.4 U.S. EPR Fuel Assembly Lateral Model – Spacer Grid Dynamic Characteristics and Allowable Crushing Load

The spacer grid is the second building block of the lateral seismic and LOCA core row model. The features and capabilities of the spacer grid element and the functional requirements of the spacer grid hardware component are tightly connected. Under accident conditions, the functions of the spacer grid hardware component are to maintain:

- The fuel rod pitch and the square arrangement of the fuel rod bundle, under certain acceptable deviation limits, to ensure coolability.
- The control rod insertability by preserving the guide tube pattern within acceptable limits.
- Sufficient load carrying capability to support a large number of the fuel assemblies in the row, as they bend and impact together against the heavy reflector.

The spacer grid element in the core model must be able to:

- Predict the correct peak impact load, for a given impact velocity.
- Restore the right amount of strain energy in the maximum deflected condition into kinetic energy of the bundle.
- Provide for a simple numerical implementation.

In addition to these requirements, the spacer grid element formulation must return peak impact loads, which can be compared directly to tested allowable crushing loads on the spacer grid hardware component.

As a result of the interconnected nature of these topics, and to improve readability, this section is structured as follows:

- Spacer Grid allowable load definition – Section 4.1.4.1 discusses the design intent, the allowable load definition, the test base supporting the values used in the U.S. EPR analysis for both unirradiated and irradiated condition.
- Spacer Grid element definition – Section 4.1.4.2 discusses the element formulation, the test base supporting the element constants, and some of the parametric sensitivity studies.

4.1.4.1 U.S. EPR Spacer Grid Allowable Crushing Load

This section concentrates on the issue of spacer grid allowable crushing load. The issue will be approached from the point of view of:

- Definition – How this allowable load is defined so that it can be directly compared to the calculated loads from the core model, and serve as a conservative estimate of the impact load capability of the spacer grid.
- Effects of in-reactor operation – How the exposure to in-reactor conditions over the service life of the spacer grid affects the grid strength.

- Test Protocol – Identify the appropriate testing conditions for both unirradiated (BOL) and irradiated (EOL) condition, which would produce a conservative, but reasonable estimate of the spacer grid impact load capability for each condition.

4.1.4.1.1 Grid Strength – NRC Guidance Review

The current industry-wide grid strength definition is based on the guidance provided in SRP 4.2 (Reference 2), and one of its background documents, NUREG/CR-1018 (Reference 12).

The SRP 4.2, Appendix A, defines the allowable crushing load $P(\text{crit})$ under externally applied forces produced by earthquakes and/or postulated pipe breaks as:

“The consequences of grid deformation are small. Gross deformation of grids in many PWR assemblies would be needed to interfere with control rod insertion during an SSE (i.e., buckling of a few isolated grids could not displace guide tubes significantly from their proper location),

In a LOCA, gross deformation of the hot channel in either a PWR or a BWR would result in only small increases in peak cladding temperature.

Therefore, average values are appropriate, and the allowable crushing load $P(\text{crit})$ should be the 95% confidence level on the true mean as taken from the distribution of measurements on unirradiated production grids at (or corrected to) operating temperature. While $P(\text{crit})$ will increase with irradiation, ductility will be reduced. The extra margin in $P(\text{crit})$ for irradiated grids is thus assumed to offset the unknown deformation behavior of irradiated grids beyond $P(\text{crit})$.”

It is important to note a few of the main points of this definition:

- The allowable crushing load is derived from the average value of the test sample, because the expected deformations of grids are small, and a few isolated deformed grids will not have an impact on coolability and control rod insertability. This shows that the intent of the original design basis was to ensure that grid deformation remains low for most grids. Some grids may even buckle, and perfectly elastic operation of the grids is not required.

- It is recognized that the strength will vary from ambient temperature to operating temperature, and a provision is made to account for the in-reactor temperature either by performing the tests hot, or by testing cold and correcting for operating temperature. The actual correction procedure is not specified.
- The effects of irradiation are assumed to counteract the deformation behavior, and, as such, the BOL strength is the controlling design parameter.
- The SRP 4.2, Appendix A, is focused primarily on the statistical definition of the allowable crushing load from the grid sample data, on the condition of the test grid specimens, and on the test environment, but it does not specify an individual grid test failure criterion (maximum indicated load versus limitations on total deformation).

Background document NUREG/CR-1018 (Reference 12) contains a more detailed discussion on the actual definition of the grid allowable impact load. Section IV of this document distinguishes between two scenarios: the case of "no permanent deformation", and the case involving "permanent deformation." The "no permanent deformation" case is defined by a limited and acceptably small permanent deformation, and not as a complete absence of permanent deformation. The relevant paragraphs are reproduced, for convenience, as follows.

"If spacer grid loading caused no permanent deformation of the spacer grid then rod to rod spacing and coolant channel flow area is undisturbed and a coolable geometry would be maintained. A small amount of permanent deformation is almost always present after spacer grid loading. Settling of the connecting strip joints and local deformation due to high local stresses are just two of the possible causes of permanent deformation. Obviously, a condition of no permanent deformation must be defined.

A sufficient condition to demonstrate that no permanent deformation has occurred appears to be that the spacer grid remain within manufacturing tolerances. This condition should be sufficient although possibly not necessary because the only meaningful definition of departure from a no-deformed condition would be that deformation which causes a measurable perturbation in the ECCS peak cladding temperature calculation.

Manufacturing tolerance criteria should fall within this deformation definition. The quantity to be used for comparison with the calculated results could be defined as that load at which initial departure from the no deformation condition is obtained.”

The following important points must be highlighted:

- The items of interest, when assessing whether a grid has “no permanent deformation,” are the rod-to-rod pitch and the flow channel area. These two parameters control the grid performance and its ability to perform the coolability function. Since this is the “no permanent deformation” scenario, control rod insertability is not the primary concern.
- The physical dimension of the overall envelope of the grid is a secondary concern. This dimension only affects the grid gaps, which NUREG/CR-1018 (Reference 12) deems to be of second order importance (Table I in Section II, Section 4.2.1). This point is discussed in more detail in Section 5.0.
- It is recognized that a small amount of permanent deformation will always be present, and that the condition of “no permanent deformation” needs to be defined.
- The “no permanent deformation” condition is defined in terms of a finite, but acceptably small deformation, which does not interfere with the coolability requirement. Essentially, the “no deformation” condition is understood to be the deformation threshold beyond which the coolability would begin to be measurably impacted.
- Limiting the grid deformation to the manufacturing tolerances would constitute a sufficient, but not strictly necessary criterion for the “no deformation” condition.

In light of the guidance contained in the SRP 4.2 Appendix A, and NUREG/CR-1018 (References 2 and 12), an appropriate spacer grid strength definition for the “no permanent deformation” case should be based on the maximum load that would produce a stable permanent deformation, which is still acceptable from a fuel coolability point of view. If the grid deformation at the buckling point is within grid manufacturing

tolerances, then the buckling load becomes the allowable grid load. In addition, even in the case of the "no permanent deformation" scenario, a measure of control rod insertability must be assured. A more detailed discussion is presented in Section 4.1.4.1.4.

One aspect of spacer grid performance, which will receive additional attention in this technical report, is the effect of in-reactor operation on the grid deformation behavior under external loads and the definition of the grid allowable impact load at EOL. While the current regulatory guidance assumes the BOL condition is limiting, AREVA defines and implements an EOL test protocol for the U.S. EPR, which will be discussed in Section 4.1.4.1.6.

4.1.4.1.2 AREVA Spacer Grid Test Method Principle

For the purpose of clarifying the discussion in subsequent sections, a brief discussion of the spacer grid testing procedure and results interpretation is included. The architecture details of the spacer grid test process and bench set-up are presented in Section A.2.

The test consists of a sequence of impacts of monotonically increasing kinetic energy content. At each impact, a small amount of permanent deformation accumulates in the spacer grid. At a certain point, the stability of the load path is lost, and the spacer grid buckles. At this point, the kinetic energy is kept constant, and additional impacts are performed. The permanent deformation of the grid is the result of localized plastic strains in the grid strips, and does not reflect a net-section plastic deformation. Using the incremental plastic deformation data from each impact, it is possible to calculate the cumulative permanent deformation, and to construct a plot with the cumulative plastic deformation on the horizontal axis, and the peak impact load at each impact on the vertical axis. This plot is referred to as the grid loading curve. A sample grid loading curve is shown in Figure 4-23 (data represent loading curve 10HP2794 in Figure 4-29). Upon inspection, a few observations are in order:

- The incremental plastic deformation at low kinetic energy levels is zero. This indicates the existence of a zero-permanent-deformation threshold, which is too low for any practical use in fuel design.
- As the kinetic energy is increased, the peak impact load increases, and so does the incremental plastic deformation at each impact. This becomes apparent when looking at the horizontal projection of the loading curve segments.
- The slope of the loading curve is monotonically increasing up to the buckling point, and is decreasing after the buckling point. This signifies that a buckled spacer grid can experience increasing levels of deformation while producing decreasing levels of impact load (i.e., a range of instability).

Figure 4-23—Sample HTP Spacer Grid Loading Curve**4.1.4.1.3 U.S. EPR Spacer Grid Allowable Crushing Load Definition – General Requirements**

This section formulates the general principles and criteria that come together to form the spacer grid allowable crushing load definition. The actual implementation of these principles to the BOL, and EOL condition grid allowable crushing load definition follows in the subsequent sections. The design basis intent for the hardware protections, which a grid strength definition must provide, follows the line of reasoning and the principles outlined in NUREG/CR-1018 (Reference 12).

For the U.S. EPR the spacer grid allowable impact loads will be defined based on the “no permanent deformation” scenario outlined in NUREG/CR-1018 (Reference 12). From the discussion in Section 4.1.4.1.1, it is clear that “no permanent deformation” does not mean the complete absence of permanent deformation, but an acceptably small deformation, which is to be defined based on the departure from flow channel performance. Figure 4-24, which is a schematic representation of an actual grid loading curve, shows the main concepts underlying the spacer grid allowable crushing load definition in the realm of possible spacer grid behavior.

Figure 4-24—Spacer Grid Allowable Load Definition



The main points are summarized below:

First, since the acceptability of deformation is the controlling factor, the limit load/deformation point must be located on the stable side of the loading curve. Taking, for example, the softer grid loading curve in Figure 4-24, the limit load must be to the left of point "C." On this side of the loading curve, a higher incoming kinetic energy, and consequently, a higher impact load is required to produce an increase in the permanent deformation of the grid. This is termed as "stable" loading, as opposed to the unstable side of the loading curve, where, it is possible to increase the permanent deformation of the grid with substantially lower impact loads.

Setting the allowable crushing load on the stable side of the loading curve ensures that the peak impact load becomes a controlling factor that determines the grid permanent deformation. Therefore, the impact loads calculated from the core models can be directly compared to the grid allowable crushing load to ensure that the permanent deformation remains below acceptable limits. This approach is also implemented by the ASME Code (Reference 4), where elastic stress resultant allowables (the formal criterion) are used to ensure dimensional stability under load (the actual design basis intent).

If the buckling load (at Point "C" in Figure 4-24) is exceeded, the maximum impact load is no longer a controlling factor on deformation since it is possible to increase the permanent deformation of the grid at substantially lower impact loads.

- In the case of softer grids, the acceptable deformation will be the limiting factor, and the allowable crushing load will have to be set at the load level that produces that permanent deformation (at point "B" in Figure 4-24). In this case, it is important to distinguish between "allowable crushing load", and "grid buckling limit", or "grid strength." In a strictly mechanical sense, the stable load carrying capability of the grid, which is the grid buckling limit, can be higher than the allowable crushing load. Additionally, in this case, the reported margin on load to the allowable crushing load is conservative from a strictly mechanical point of

view, because it discounts the additional load carrying capability of the grid from the allowable crushing load (point "B") up to the buckling point (point "C").

In the case of stiffer grids, buckling occurs inside the acceptable deformation limit, and the grid allowable load can be the actual grid buckling load (point "A" in Figure 4-24). The design margin is ensured by the calculated load margin to buckling.

The distinction between relatively stiffer and softer grids is not only triggered by their design, but, as will be discussed in the sections to follow, by the condition of the grid – new material versus irradiated. Section A.1 includes a discussion of irradiated grid tests, which shows that irradiated grids reach the buckling point at lower permanent deformation because of irradiation hardening of the grid material, which results in lower permanent deformation before buckling. This means that the "grid strength" for a given grid design could be defined differently at BOL and EOL. At BOL, the acceptable deformation could be the controlling factor, whereas at EOL, the buckling strength could be limiting. Consequently, a scenario such as the one depicted in Figure 4-25 could emerge. The more compliant BOL grid allowable crush load could be limited at point B, or B*, whereas the less compliant EOL grid allowable crush load could be limited at point A. Depending on the stiffness of the BOL design, it is conceivable that the allowable crush load for BOL, which is based on deformation, could be higher, equal, or even less than the allowable crush load at EOL, which is based on buckling load, whereas the mechanical buckling strength of the BOL grid could be substantially higher than the EOL grid.

- If permanent deformation is the controlling factor, the deformed shape of the grid at the limiting acceptable deformation should be uniform, that is to say that the permanent deformation should be distributed approximately equally between the fuel rod rows, so that the change in any individual flow channel is small. Because of this, a deformation pattern, (see Figure A-15), which is representative of deformation in the post-buckling regime, may not be acceptable since most of

the deformation is concentrated in the few buckled rows, and the effect on individual flow channels could be significant. A deformed shape, such as the one presented in Figure A-17, would be acceptable because the permanent deformation of the grid is uniformly distributed between the fuel rod rows with minimal effect on individual flow channels.

- The deformed shape of the grid at the deformation limit must also ensure control rod insertability. Therefore, a special gauge (shown in Figure A-14) simulating the control rods on the outer guide tube pattern is inserted into the deformed grid, to ensure the control rods can move freely. This test represents a conservative way of proving control rod insertability, since it discounts the flexibility of the control rods, which would allow them to “snake” inside the guide tube.

If the grid buckles inside the deformation limits, this test is not necessary, and the control rod insertability is ensured by virtue of the small level of deformation.

Figure 4-25—Spacer Grid Allowable Load Definition



It should be emphasized that the preceding discussion applies when establishing the allowable crushing load for one individual grid. For the purposes of grid testing, a sample of 6 to 8 grids is used, and the allowable crushing load is determined following the statistical process outlined in SRP 4.2, Appendix A. In case the grids are deformation limited, the allowable load at the prescribed allowable deformation is calculated (linearly interpolated on the loading curve) for each individual grid, and then the statistical process is applied on the individual grid allowable loads. For buckling load limited grids, the statistics are performed directly on the buckling loads.

4.1.4.1.4 U.S. EPR Spacer Grid Allowable Crushing Load – Unirradiated Condition

This section discusses the actual determination of the spacer grid allowable load for the unirradiated case, for the two types of intermediate spacer grids included in the optimized U.S. EPR design (Figure 2-2):

- HTP [] thick inner strip – at the mid-elevation locations.
- HTP [] thick inner strip and [] weld nugget size – at the remaining locations.

4.1.4.1.4.1 U.S.EPR HTP [] Strip Grid – BOL Allowable Crushing Load

This section includes an overview of the test results, and defines the allowable crushing load for the M5[®] HTP [] strip grids at BOL.

A total of [] M5[®] grids with strip thickness of [], and weld nugget size of [] in BOL condition, were tested at [] by successive impacts of increasing kinetic energy. The plot of peak impact load at every impact versus the cumulative permanent deformation is presented in Figure 4-26. [

]. The others were tested to buckling, or to the mechanical limits of the test bench.

Figure 4-26—U.S.EPR HTP [] Strip Grid – BOL Test Data

Using the criteria outlined in Section 4.1.4.1.3, the HTP [] strip grid in BOL condition is limited by the acceptable deformation of []. Therefore:

- The allowable crushing load is defined as the 95% lower confidence on the true mean on the load that produces the [] deformation.
- The allowable load / deformation limit point is located on the stable side of the loading curve.

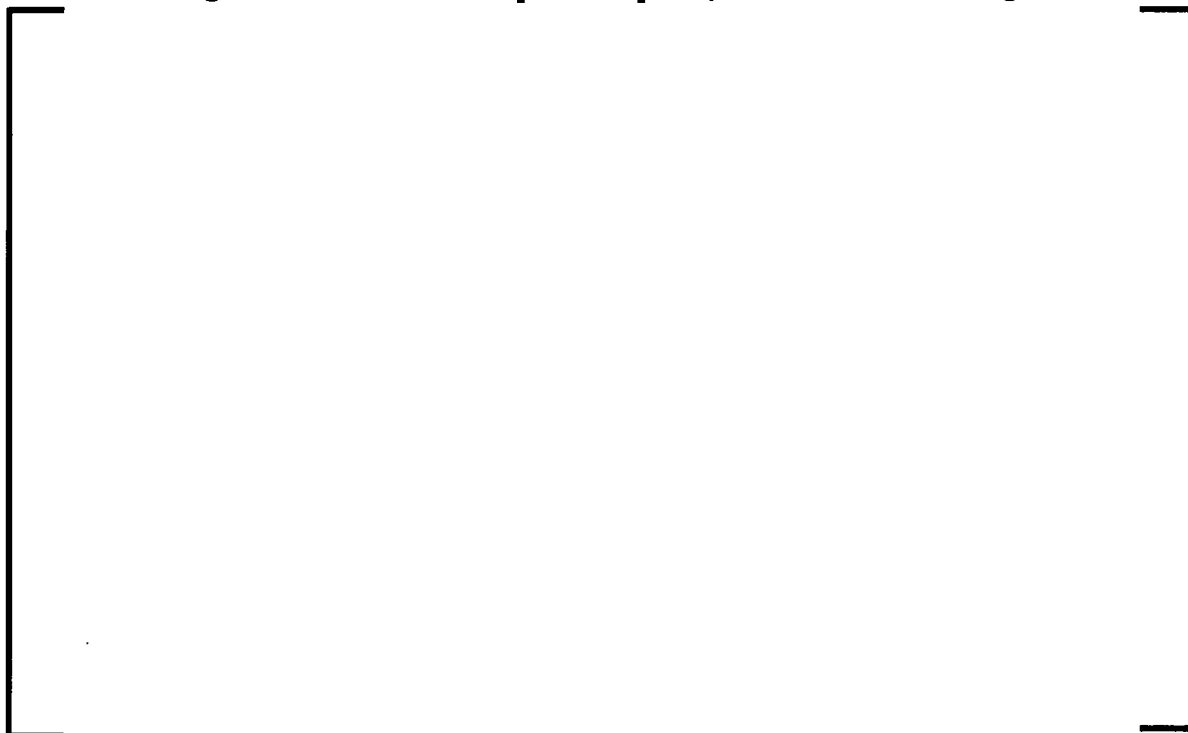
- At the deformation limit of [], the grid deformation is uniformly distributed across the fuel rod rows, as indicated by []. The details of this assessment, which includes data from visual inspections and measurements, are presented in Appendix 0. Figure A-17 and Figure A-18 present the deformed grid condition at [] permanent deformation. The direction of impact is vertical in the pictures. No signs of racking are present, and the deformation is indistinguishable upon visual inspection. Further details can be obtained by examining Figure A-21 and Figure A-22, which plot the [] which indicates uniform distribution of deformation throughout the spacer grid.
- The acceptability of the grid deformation from a coolability standpoint is addressed in Section 4.1.4.1.4.1.
- The control rod insertability was tested on all grids at [] deformation, using the gauge presented in Figure 4-28. The gauge passed through all grids at [] permanent deformation. The simulated control rod pin segment outside diameter [] thus rendering the control rod insertability test conservative. Also, the two spacer grids [] were measured to ascertain the uniformity of the guide tube pattern. The details are presented in Section A.4. Based on these measurements, [].

This displacement is small enough to maintain a clearance between the control rod OD and the guide tube inner surface. It is important to point out that the procedure is conservative, in that it discounts the flexibility of the actual control rods, and their ability to comply with even higher levels of misalignment.

Figure 4-27—Control Rod to Guide Tube Clearance Schematic



Figure 4-28—HTP Grid [Strip - Control Rod Gauge



In conclusion, the tests discussed in this section support an allowable crushing load limit for the U.S. EPR [] strip HTP spacer grids of []

[] The definition of the allowable crushing load limit meets all the general requirements discussed in Section 4.1.4.1.3. Recent tests indicate that this grid design has the potential for directional dependence of the grid allowable crushing load and dynamic stiffness. The tests discussed above were performed along the strong direction of the grid. As such, a penalty factor is applied on the tested grid crushing load. The details are discussed in Section 4.1.4.1.7.

4.1.4.1.4.2 U.S.EPR HTP [] Strip Grid – BOL Allowable Crushing Load

In this section we include an overview of the test results, and define the allowable crushing load for the M5[®] HTP [] strip grids at BOL.

A total of [] Zr-4 grids with strip thickness of [], in BOL condition, were tested at [], by successive impacts of increasing kinetic energy. The grids are very similar to the U.S.EPR design, [], and the Zr-4 material instead of M5[®]. The plot of peak impact load at every impact versus the cumulative permanent deformation is presented in Figure 4-29. All the grids were tested to buckling and beyond, up to [] permanent deformation. Post-buckling behavior is not a concern in this discussion.

Using the criteria outlined in Section 4.1.4.1.3, the HTP [] strip grids in BOL condition are limited by the acceptable deformation of []. Therefore:

- The allowable crushing load will be 95% confidence on the true mean, on the load that produces the [] deformation.

- The allowable load/deformation limit point is located on the stable side of the loading curve.
- The uniform character of deformation at [] has not been tested for these grids, but the behavior is bounded by that of the HTP [] grids discussed in the previous section, based on the fact that the []

[] Also, an additional measure of the uniform character of the grid lattice is the coefficient of restitution during each impact. In order for a spacer grid lattice to incur non-uniformly distributed deformation, the "square" pattern must be broken. During the impact when this happens, the coefficient of restitution drops substantially, signaling a sharp drop in the rebound kinetic energy recovered after the impact. For all impacts within the allowable deformation range and beyond, the coefficient of restitution for these grids is constantly high, which signifies no buckling, and therefore a uniform deformation pattern (more details are discussed in Section 4.1.4.2).

- The acceptability of the grid deformation from a coolability standpoint is addressed in Section 4.1.4.1.4.1.
- The control rod insertability was tested on all grids at each impact, and the simulated control rod gauge (Figure A-14) was insertable for permanent deformation levels of up to [] The simulated control rod pin [] which is prototypical of the U.S.EPR control rod design.

Figure 4-29—17x17 HTP [] Strip Grid – BOL Test Data



The tests discussed in this section support an allowable crushing load limit that meets all the general requirements discussed in Section 4.1.4.1.3 of [

].

One point that needs to be addressed is the difference in grid strip material between the tested grids, which were made of Zr-4, and the U.S.EPR grid design which uses M5[®].

Previous tests [

] Therefore, using the Zr-4 tested grid strength is acceptable.

Recent tests indicate that this grid design has the potential for directional dependence of the grid allowable crushing load and dynamic stiffness. The tests discussed above were performed along the strong direction of the grid. As such, a penalty factor is applied on the tested grid crushing load. The details are discussed in Section 4.1.4.1.7.

4.1.4.1.5 U.S. EPR Spacer Grid Allowable Crushing Load – Thermal-Hydraulic Acceptability of the Unirradiated Spacer Grid Deformation Limit

The impact of the fuel assembly faulted condition analyses for the U.S. EPR on fuel assembly spacers has been evaluated to be minimal. The loads on the irradiated spacers are such that buckling does not occur and any deformation which occurs, is significantly less than manufacturing tolerance on the spacer grid outer envelope of [] inches. This conclusion applies to both irradiated fuel assemblies in the core interior and on the core periphery.

The loads on un-irradiated spacer grids are such that the predicted deformation on all fuel assemblies in the core interior are less than the manufacturing tolerance on the spacer grid outer envelope. The loads on the un-irradiated spacer grids on the core periphery are such that only the [] spacer grids, in specific core locations, are deformed more than the manufacturing tolerance and then by only [] inches. The specific peripheral core locations where this maximum deformation occurs are identified in Figure 5-1.

Fuel assemblies that undergo a deformation less than the manufacturing tolerance on the spacer grid envelope would have a negligible impact on the thermal-hydraulic related criteria for the affected fuel assembly, on the departure from nucleate boiling ratio and on the peak cladding temperature. In addition, the margins for the thermal-hydraulic criteria are especially large for fuel assemblies on the core periphery because of their low power. These low assembly power conditions can be seen in U.S. EPR FSAR Tier 2, Figure 4.3-11, Figure 4.3-13, and Figure 4.3-15.

The core peripheral fuel assemblies identified in Figure 5-1, under a deformation of [] inches larger than the manufacturing tolerance, will experience an increased moderation in the enlarged gap between the fuel assemblies. This total degree of deformation has a small impact on the power peaking between the affected fuel assemblies. These small peaking changes are negligible relative to the high thermal and peaking margins for these core periphery locations because of their low power. Again, the core periphery reduced power condition can be seen in the U.S. EPR FSAR Tier 2 figures noted earlier.

4.1.4.1.6 U.S. EPR Spacer Grid Allowable Crushing Load – Irradiated Condition

A detailed description of the in-reactor operation effects on zirconium alloys, and spacer grid strength is presented in Section A.1. The conclusion is that the major factors that influence the spacer grid strength at EOL are [

[]]. The remaining effects of in-reactor operation, [] were deemed secondary based on previous irradiated grid tests.

The two main factors, [] have opposite effects on the irradiated grid strength. []

]

In Section A.1, as part of the review of the effects of in-reactor operation on the mechanical material properties of Zirconium alloys, it is concluded that [

]. This section presents a quantitative comparison of these factors.

First, the M5[®] [

]

Table 4-5—M5[®] Yield Strength Comparison

[

]

A second comparison must involve the [

]

**Figure 4-30—Comparison of Rate of Strength and Relaxation versus
Fluence**



In conclusion, a more realistic, but still conservative EOL test protocol is to test the [] grids [] , to best approximate the full effects of irradiation. The general requirements in Section 4.1.4.1.3 still apply when deciding the limiting factor for defining the allowable crushing load.

To confirm some of the theoretical considerations presented so far, two types of tests were performed on [] grids. The grids tested were [] material. The first batch of [] grids was tested at [] , and the second batch of [] grids was tested at [] . The results are plotted in Figure 4-31. Note that the only difference between the two sets of grids tests []

The tests discussed above support a 95% confidence allowable crushing load at

[

]

The [] strip HTP [] grids were tested []. A similar post-processing as, previously indicated, was applied to the test data, and the results support a 95% confidence allowable crushing load of []. For M5[®],

[

].

Recent tests indicate that both the [] grid designs have the potential for directional dependence of the grid allowable crushing load and dynamic stiffness. The tests discussed above were performed along the strong direction of the grid. As such, a penalty factor is applied on the tested grid crushing load. The details are discussed in Section 4.1.4.1.7.

For both the [], the deformation to buckling is very low (less than [], as shown in Figure 4-35, and Figure 4-36). The uniform deformation and control rod insertion requirements are therefore met. A further confirmation of this test protocol is discussed in more detail in Appendix 0, where the results of irradiated grid tests performed at operating temperature (discussed in Section A.1) are compared to the results of the [

] and

plotted together with the hot irradiated grid test results. The generic plot is presented in Figure 4-32. The results are indexed on the x-axis by the average grid cell slip load (a proxy for grid cell relaxation), to make the comparison. It is observed that the buckling strength of the [

], adequately follows the trend of the irradiated grids tested hot. This is further proof that the proposed EOL test protocol is a realistic and representative approach for assessing the EOL grid allowable crushing load capability. The discussion in Appendix 0 also covers the higher variability of the irradiated spacer grid data and the conservative nature of the simulated irradiated test data in that context. The two major sources of conservatism in the simulated irradiated grid testing protocol are:

- The effects of oxidation are excluded. []
], as was discussed in Section A.1.
- Tests are performed with []

]

**Figure 4-32—Comparison of Irradiated Hot versus Ambient
Temperature Grid Strength Tests**



4.1.4.1.7 U.S. EPR Spacer Grid Allowable Crushing Load – Summary

This section summarizes the grid allowable crushing load data, and the test protocol information discussed in Section 4.1.4.1. Also, it implements the allowable crushing load penalty factor to be applied on the test data discussed in Sections 4.1.4.1.4 and 4.1.4.1.6.

The allowable spacer grid crushing load is defined based on the following considerations (in accordance with NUREG/CR-1018 (Reference 12)):

- The objective criterion for establishing grid failure is the cumulative permanent deformation threshold, beyond which the thermal-hydraulic performance of the grid would begin to be measurably impacted. A uniform deformation pattern of the grid lattice simplifies the evaluation of this criterion.
- The load/deformation allowable point must be on the stable side of the loading curve.
- An HTP grid can be limited by either deformation or buckling load, depending on the irradiated condition.
- Control rod insertability must be proven at the limiting deformation.

The unirradiated condition grid allowable crushing load is defined as:

- Lower 95% confidence limit on true mean load corresponding to a [] permanent deformation of the grid envelope, []

The irradiated condition grid allowable crushing load is defined as:

- Lower 95% confidence limit on true mean load at buckling. []
- Test protocol is based on []

The main sources of conservatism built-in the spacer grid allowable crushing load are:

- The unirradiated [] deformation load limit is less than the actual grid buckling capability.
- The irradiated grid test protocol ignores the potential benefit of oxidation for M5[®] grids [].
- The irradiated grid test protocol ignores the potential benefit of testing with []. Potential benefits are in the same order of magnitude as oxidation.

As mentioned in Sections 4.1.4.1.4 and 4.1.4.1.6, recent tests performed on the

[

] on the strips as shown in

Figure 4-33 and Figure 4-34. The ligament [

] Separate tests have been

conducted on the [

]

direction. The results show that:

- The un-irradiated condition grids tested in the [

]

- The un-irradiated condition grids have a [

] Since the un-

irradiated condition crushing load allowable limits are based on deformation, this finding has no bearing on the current analysis.

- The simulated irradiated condition grids tested in the [

]

- The [

] direction is taken.

For the U.S. EPR, the proposed design will include a [

]

Figure 4-33 Strip Parallel to Standard Direction of Impact

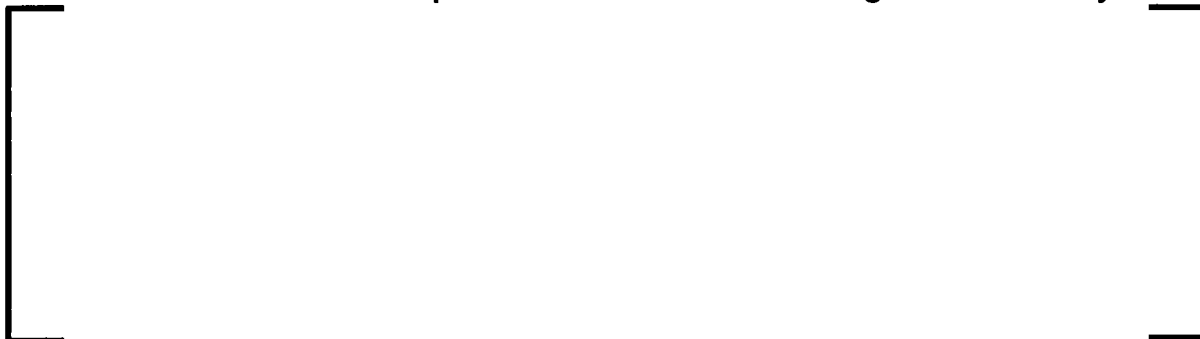


Figure 4-34 Strip Parallel to Non Standard Direction of Impact



In view of all the considerations discussed in this section, the allowable crushing load data used in this analysis is summarized in Table 4-6.

Table 4-6—U.S. EPR Spacer Grid Allowable Crushing Load Summary



For the purpose of comparison, Figure 4-35 and Figure 4-36 plot the unirradiated and simulated irradiated test results on the same set of axes, for the [

] strip HTP grids respectively (note that the results shown are for the standard loading direction). These plots reveal the following common conclusions:

- The unirradiated strength at [] permanent deformation is higher than the simulated irradiated strength.
- Permanent deformation in the simulated irradiated condition is very low, and therefore, is not a concern as it relates to lattice pattern uniformity and control rod insertion.

**Figure 4-35—17x17 HTP [] Grid Strength
– BOL versus EOL**



$$M\ddot{x} + C\dot{x} + Kx = 0$$

$$x(0) = 0$$

$$\dot{x}(0) = V_0$$

Equation 4-13

Where x is the coordinate in the direction of impact, M , C , and K signify carriage mass, damping, and stiffness, ω is the natural frequency of the system, and ζ is the damping ratio (defined in Equation 4-9 and Equation 4-10). With V_0 as the impact velocity, the ensuing response is:

$$x(t) = \frac{V_0}{\omega\sqrt{1-\zeta^2}} e^{-\zeta\omega t} \sin(\omega\sqrt{1-\zeta^2}t)$$

Equation 4-14**Figure 4-37—Spacer Grid Test and Element Schematic**

It is important to notice that Equation 4-14, while mathematically valid for any value of time, applies to the spacer grid model only for the duration of impact, which can be expressed as:

$$T = \frac{\pi}{\omega\sqrt{1-\zeta^2}} \quad \text{Equation 4-15}$$

Two key parameters for the characterization of spacer grid impact behavior are the coefficient of restitution, which is defined as the absolute value of the ratio of the rebound velocity to the impact velocity, and the peak impact load, which occurs at half the impact duration, and can be expressed as the product of the stiffness and maximum displacement. The peak impact load squared is proportional to the maximum strain energy accumulated in the spacer grid during impact. These two parameters are expressed below:

$$\left[\begin{array}{l} \text{Equation 4-16} \\ \text{Equation 4-17} \end{array} \right]$$

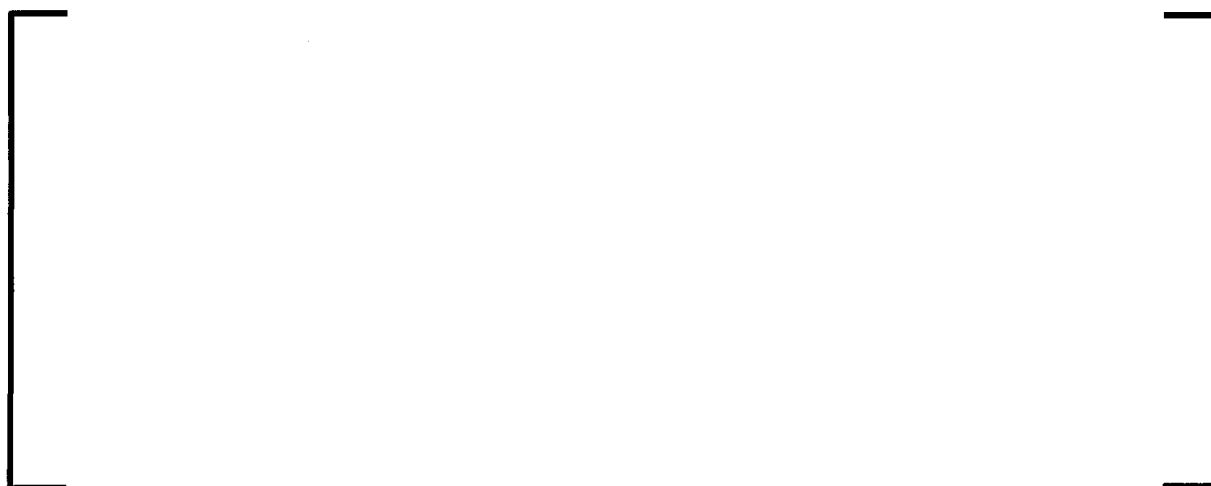
From Equation 4-16, it is apparent that a linear visco-elastic element has a constant coefficient of restitution, which is only a function of the damping ratio. From Equation 4-17, it can be concluded that for a linear visco-elastic element, the square of the peak impact force is proportional to twice the impact kinetic energy with the proportionality factor being a function of the stiffness and damping ratio. For the idealized case of zero damping, the energy conservation principle is recovered.

Thus, if a linear visco-elastic mechanical component were tested under repeated impacts of increasing kinetic energy, with a constant carriage mass M , the plots for F^2 versus MV^2 , and ϵ versus MV^2 [], and would look similar to the schematic representation shown in Figure 4-38.

This observation provides the validation criterion for the adequacy of the gapped linear visco-elastic model for spacer grids. If the F^2 versus MV^2 , and ϵ versus MV^2 plots

generated from a sequence of impact tests of increasing kinetic energy with constant carriage mass (like the tests outlined in Section 4.1.4.1.2) [], the spacer grid is dynamically equivalent to a gapped linear visco-elastic element. This dynamic equivalence pertains to the ability of the gapped linear visco-elastic element to accurately predict the peak impact load, and the rebound velocity, given the input kinetic energy.

Figure 4-38—Impact Behavior of a Linear Visco-Elastic Element



The comparison between the spacer grid test data and the linear visco-elastic element is shown in Figure 4-39 and Figure 4-40. Revisiting the HTP [] grid allowable load plot in Figure 4-29, it can be seen that the allowable crushing load, which is defined by the acceptable permanent deformation, is located [

] All the tested grids have practically the same behavior up to the allowable load, so two representative grids are chosen for illustrative purposes in Figure 4-39 and Figure 4-40. From the plots in Figure 4-39 it is apparent that the F^2 versus MV^2 curve is practically [

]. In the range delimited by the allowable crushing limit, the coefficient of

restitution is [

]

The same observations hold for the HTP [] grid. Revisiting Figure 4-26, it can be seen that the allowable crushing load, which is defined by the acceptable permanent deformation, is located []. Taking, for example, grid B30125, the plots in Figure 4-40 show that the F^2 versus MV^2 curve is practically []. Unlike the [] grids, which were tested in the post-buckling domain, these grids were only tested up to the buckling point. This is the reason why the restitution coefficient does not drop to []. In the range delimited by the allowable crushing limit, the coefficient of restitution is practically [].

The observations above demonstrate the adequacy of the linear visco-elastic grid model in the core row models. The main points are:

- The spacer grid, with all the complexities of its structure and energy dissipation mechanisms, is dynamically equivalent to a linear visco-elastic element.
- The peak impact load squared is in a linear relationship to the incoming kinetic energy over the entire range of allowable crushing loads up to the buckling point.
- The energy dissipation, as measured by the coefficient of restitution is practically constant over the entire range of allowable loads.
- Therefore, the linear visco-elastic element is capable of accurately predicting the peak impact load, the maximum deflection under impact, and the rebound velocity. This is essentially all that is required from an accident loads analysis point of view.

Therefore, the linear visco-elastic grid model is adequate for the accident analysis of the U.S.EPR fuel, up to the allowable crushing load. One outstanding issue that needs to be answered is related to the difference in the energy dissipation mechanism between the visco-elastic element and the spacer grid, and it will be addressed in the following paragraphs.

**Figure 4-39—Impact Test of HTP [] grid 10HP2790 –
Energy Storage and Dissipation**

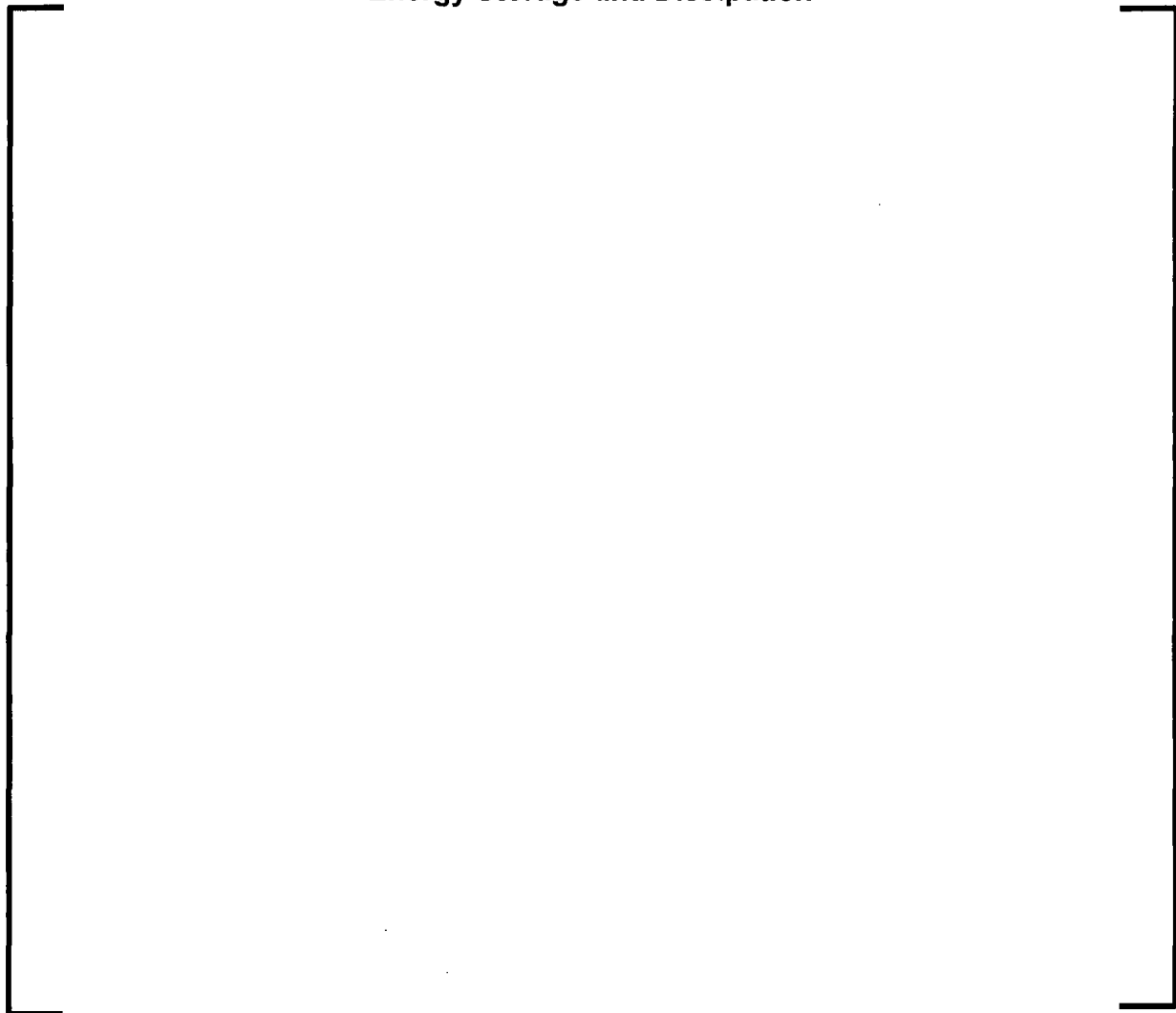
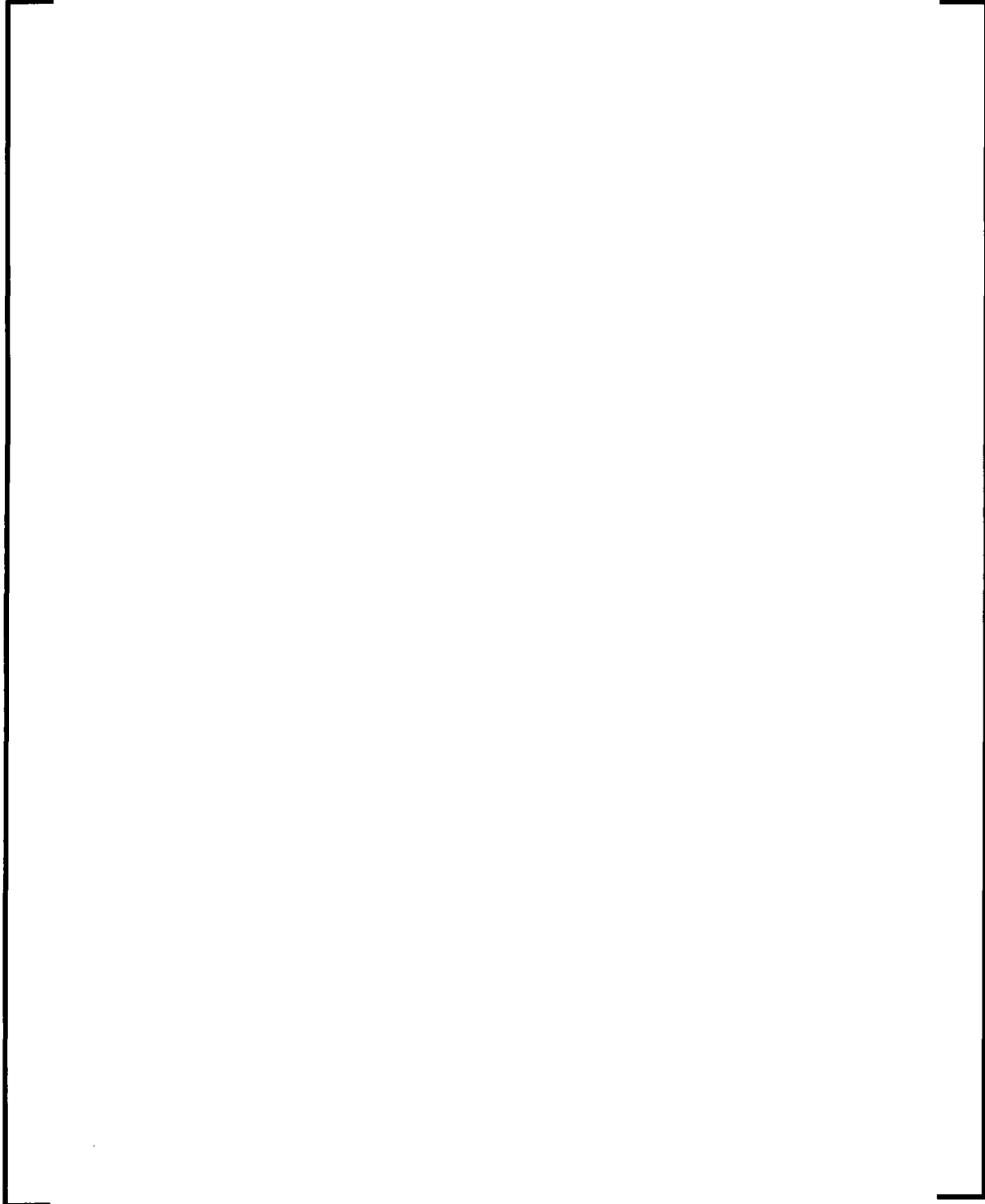


**Figure 4-40—Impact Test of HTP [] grid B30125 – Energy
Storage and Dissipation**



The restitution coefficient and F^2 plots are post-processed to obtain the grid model stiffness. The process conforms to the AREVA standard methodology in Addendum 1 of Reference 2.

The linear visco-elastic grid element discussed in the previous paragraphs is an adequate modeling approach for the spacer grid impact in the core row model, in that it produces accurate values for peak impact load, deflection under load, and rebound velocity. However, the energy dissipation mechanism is different from the actual grid structure. In a real grid, the energy dissipation is structural in nature, and consists of local plastic deformation, and friction. In a linear visco-elastic element, the energy dissipation is viscous in nature. This difference does not alter the prediction of peak impact load, maximum impact deflection, or rebound velocity, but it alters the size of the core gaps. The linear visco-elastic element returns to zero displacement at the end of an impact, whereas a real grid accumulates a small permanent deformation, which changes the core gap at that location.

Because grid deformation is stable by virtue of selecting the limit load/deformation point on the stable side of the loading curve, this issue can be addressed through a core gap sensitivity study. The approach is further bolstered by the fact that the threshold deformation of [

]

For this purpose, a study was conducted to gauge the sensitivity of the reported grid impact loads and non-grid component stresses to variations in the core gaps. The detailed discussion of the study for grid loads is presented in Section 5.0, and for non-grid component loads in Section 7.0.

4.1.4.3 U.S. EPR Spacer Grid – Stability under Repeated Impacts

Note that this section is for information only and the results and conclusions it provides are not used to establish design margins.

The spacer grid allowable crushing load and FEM discussed in the previous sections rely on the assumption that the deformation limits and the dynamic parameters derived based on the standard test protocol (monotonically increasing impacts) are sufficiently applicable to an actual seismic time history, where the impacts come in random order. To address concerns raised during the review process and to demonstrate the conservatism of the standard test protocol, AREVA has performed a few non-standard tests on U.S. EPR [] HTP grids. This section presents the most relevant results and conclusions. The detailed discussion is included in Appendix 0.

The most interesting results were obtained from a [] . Both tests were performed on unirradiated grids.

The main conclusions from the [] impacts test are:

- Under [], the F^2 versus Kinetic Energy plot []
- The grid deformation stabilizes in a few impacts – []
- The total permanent deformation and maximum peak impact load are [] .
- The ascending impact test (the standard protocol) maximizes both peak impact loads and permanent deformation which makes the linear visco-elastic grid model based on the standard protocol conservative. This also results in a grid element which maximizes predicted loads.

The main conclusions from the [] test are:

- Grid permanent deformation stabilizes after the []

- []
- The ascending impact grid protocol is bounding []
- []

For simulated irradiated grids, a test protocol with [] was used.

Each impact in the standard test protocol sequence []
]. The resulting buckling load was unchanged from the
standard test protocol.

Therefore, the U.S. EPR HTP grid is stable under real seismic loading histories involving a large number of impacts. The increasing impact test protocol is conservative, in that it maximizes the permanent deformation the grid accrues under the allowable crushing load, and the resulting grid model maximizes the predicted impact loads.

4.1.5 U.S. EPR Fuel Assembly Row Model – Seismic and LOCA Response Analysis Process

The seismic and LOCA response analysis is performed on the core row models, which consist of a planar section through the core, along a fuel row. The interactions with neighboring rows are disregarded. The conservative nature of this assumption has been discussed in the introduction of Section 4.1. The core row model architecture, presented schematically in Figure 4-41, consists of a number of fuel assembly models (defined in Section 4.1.1) arranged in a parallel array. The top and bottom end nodes

are coupled in all directions, and receive as input the transient time histories derived from the reactor internals models. The intermediate spacer grid nodes on the fuel assembly are connected by gapped spring/damper elements to the heavy reflector and/or to the neighboring assemblies. Heavy reflector node motion is derived from the lower core plate and the core barrel top motions, using the assumption that the heavy reflector is rigid compared to the fuel assembly. Because the natural frequencies of the fuel assembly and those of the heavy reflector are one order of magnitude apart, this modeling technique is justified.

Figure 4-41—U.S. EPR Core Row Model Schematic



The detailed gapped spring connections at FA-FA interface is presented schematically in Figure 4-42. The beam node on the fuel assembly column is connected via an internal spring/damper element (constants K_I and C_I) to a small mass [] node, which, in turn is connected to the gap element on the right, and via an external spring/damper combination (constants K_E and C_E) to the gap on the left. The external stiffness and damping coefficients are determined from the spacer grid tests discussed in Section 4.1.4. The role of the external spring/damper combination is to model the load path going through the fuel assembly when all or most assemblies in the row are deflected and loading against the heavy reflector. The role of the internal spring/damper combination is to represent an energy storage mechanism for the motion of the fuel rods inside the spacer grid, and more importantly, for the higher mode response of the fuel assembly span during an impact. Since the fuel assembly beam model has one element per span, it cannot capture the impact energy partition, between the grid and the fuel bundle, which creates the need for the internal spring/damper. This is detailed further in Section 4.1.5.1.

Figure 4-42—U.S. EPR FA-FA Gapped Spring-Damper Connecting Elements



The rotational springs discussed in Section 4.1.1.1, and benchmarked in Section 4.1.1.2.4, are arranged in a different manner for the core row model. The rotational stiffness is the same, but it is distributed between two rotational springs connected at the top and bottom nodes on the assembly (Figure 4-43), and the stiffness is partitioned inversely proportional to the distance from the individual ISG to the two end nodes of the assembly, as follows:

$$T_1 = T \frac{S - H}{S} \quad \text{Equation 4-18}$$

And,

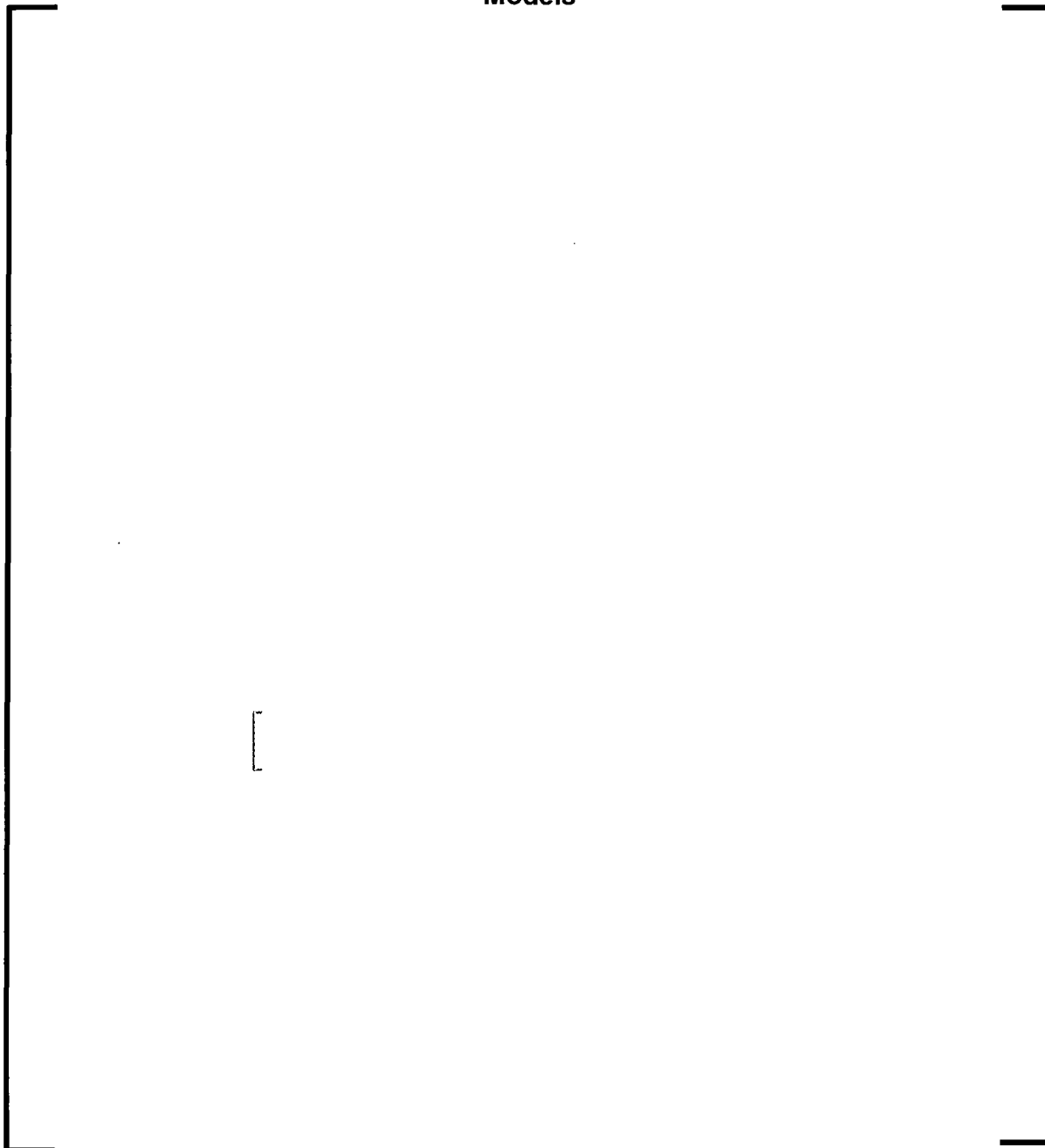
$$T_2 = T \frac{H}{S} \quad \text{Equation 4-19}$$

Where T is the benchmarked rotational stiffness of the intermediate spacer grid; S is the fuel bundle span between the top face of the bottom nozzle, and the lower face of the top nozzle; and H is the elevation of the grid mid-pane from the top face of the bottom nozzle. It is clear that the sum of the two stiffness values T_1 and T_2 is T . Therefore, this technique does not modify the dynamic characteristics of the fuel assembly. [

].

In addition to the elements discussed so far, each fuel assembly in the core row model is coupled to the heavy reflector by the hydrodynamic coupling elements discussed in Section 4.1.2, and presented in Table 4-7. In addition, the fuel assembly beam elements are assigned the Rayleigh damping coefficients as discussed in Section 4.1.3, and as shown in Table 4-8.

Figure 4-43—U.S. EPR Rotational Spring Arrangement for Core Row Models



Element properties are converted from the benchmarked values, obtained at ambient temperature, to the in-reactor operating temperature. For this purpose, the beam elements have their elastic modulus scaled to the core average temperature operating

temperature, which is conservatively 600°F, based on 596.8°F, in Table 4.4-1 of the U.S. EPR FSAR (Reference 5). Spacer grid rotational stiffness is also scaled with grid material elastic modulus. The stiffness values for all the cases in the frequency sweep, and at operating temperature are shown in Table 4-9.

Table 4-7—U.S. EPR Fuel Assembly Model - Hydrodynamic Coupling Matrix Terms

--

Table 4-8—U.S. EPR Fuel Assembly Model – Rayleigh Damping Coefficients

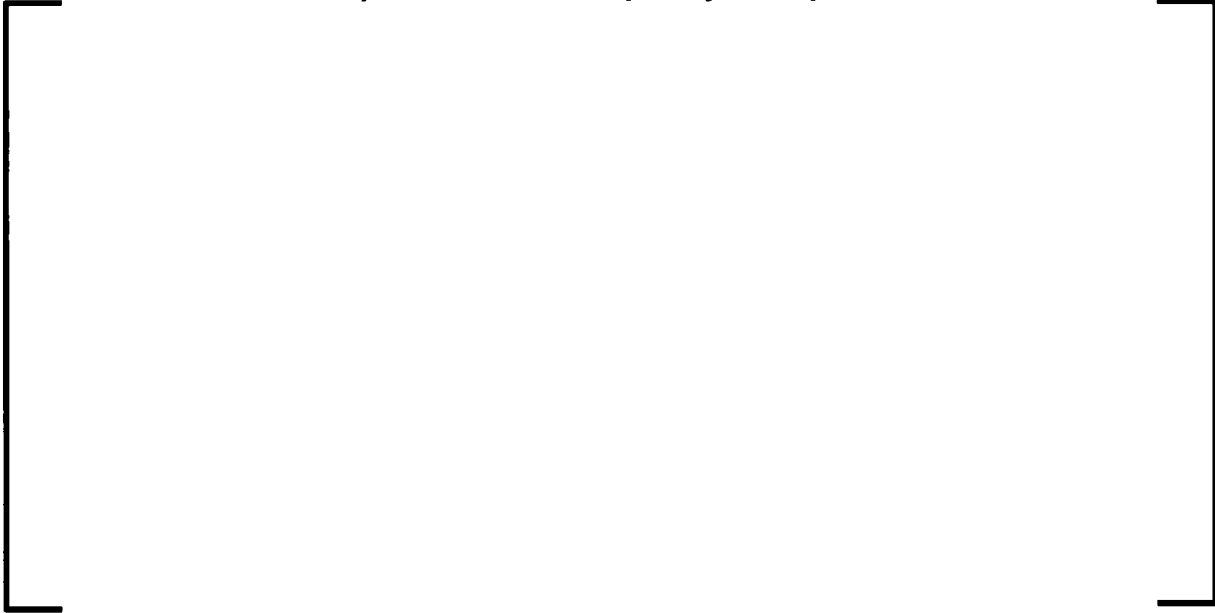
--

Table 4-9—U.S. EPR Rotational Spacer Grid Stiffness – Operating Temperature – All Frequency Sweep Cases

--

With all these parameters included in the fuel assembly, the natural frequencies of a single assembly, in water, at operating temperature, and for all the cases in the frequency sweep, are shown in Table 4-10.

Table 4-10—U.S. EPR Fuel Assembly Frequencies (Hz) – Operating Temperature – All Frequency Sweep Cases



4.1.5.1 U.S. EPR Fuel Assembly Lateral Model – Single Fuel Assembly under Impact in Ambient Air

This section discusses the test benchmark process for determining the internal spring/damper constants, K_i and C_i . For this purpose, the assembly must be tested in an impact test. The arrangement is very similar to that shown in Figure 4-5, with the only difference being that a rigid plate simulating the heavy reflector is placed next to the fuel assembly at the mid-span elevation, at a distance equal to one core gap. For the U.S. EPR, since there is no mid-span grid, the simulated rigid plate extended over the span of HTP4 and HTP5 (in Figure 4-5) and the test was conducted with simultaneous impacts at the two near mid-span grids. This approach is very conservative, because it increases the reported internal stiffness of the grid.

Following the test, the model of the fuel assembly heavy reflector impact test is constructed as shown in Figure 4-44. The gapped springs/dampers at ISG4 and ISG5 are equivalent representations of the actual spring arrangement shown in Figure 4-45.

Figure 4-44—U.S. EPR Fuel Assembly Impact Test Model

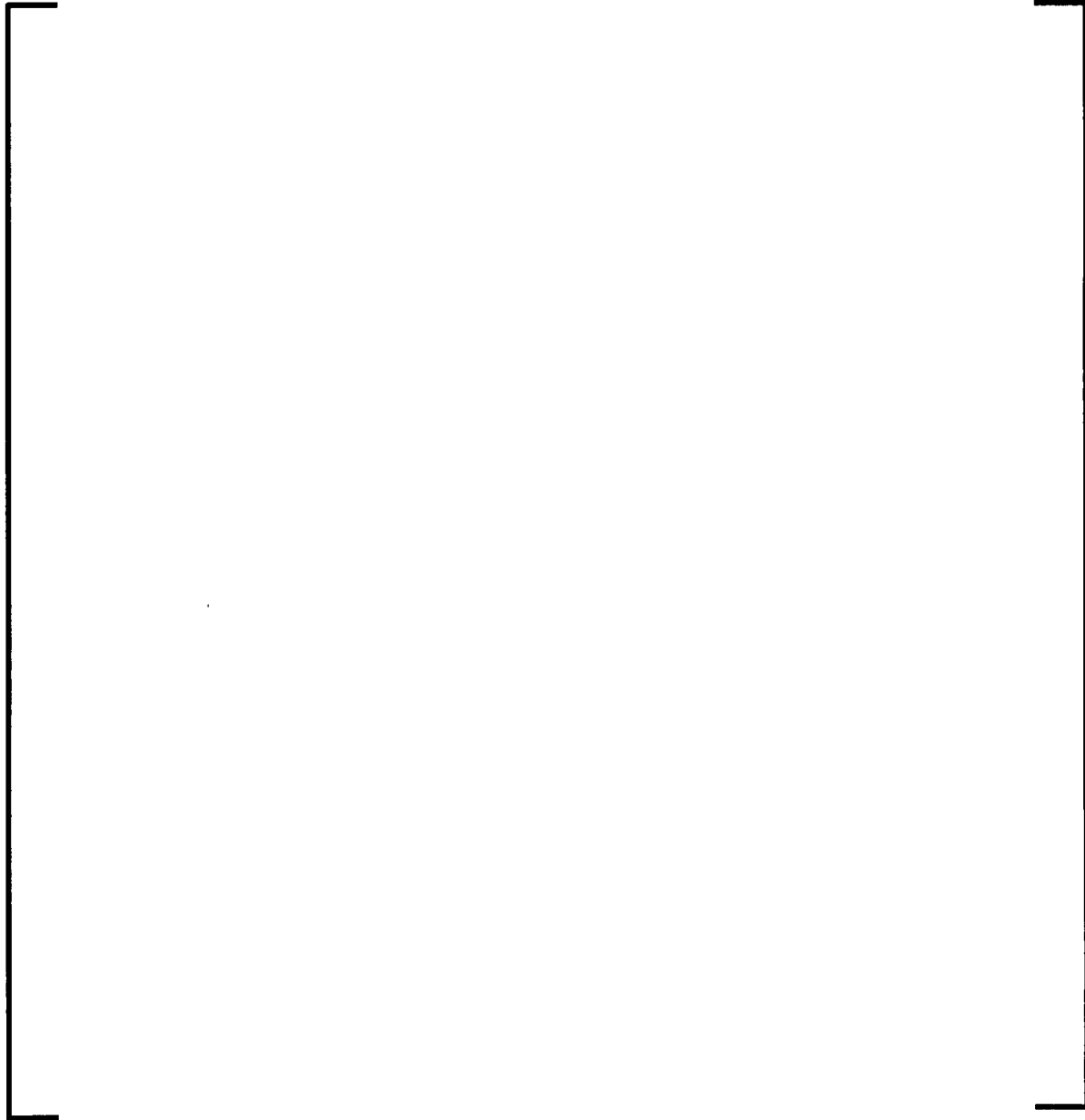
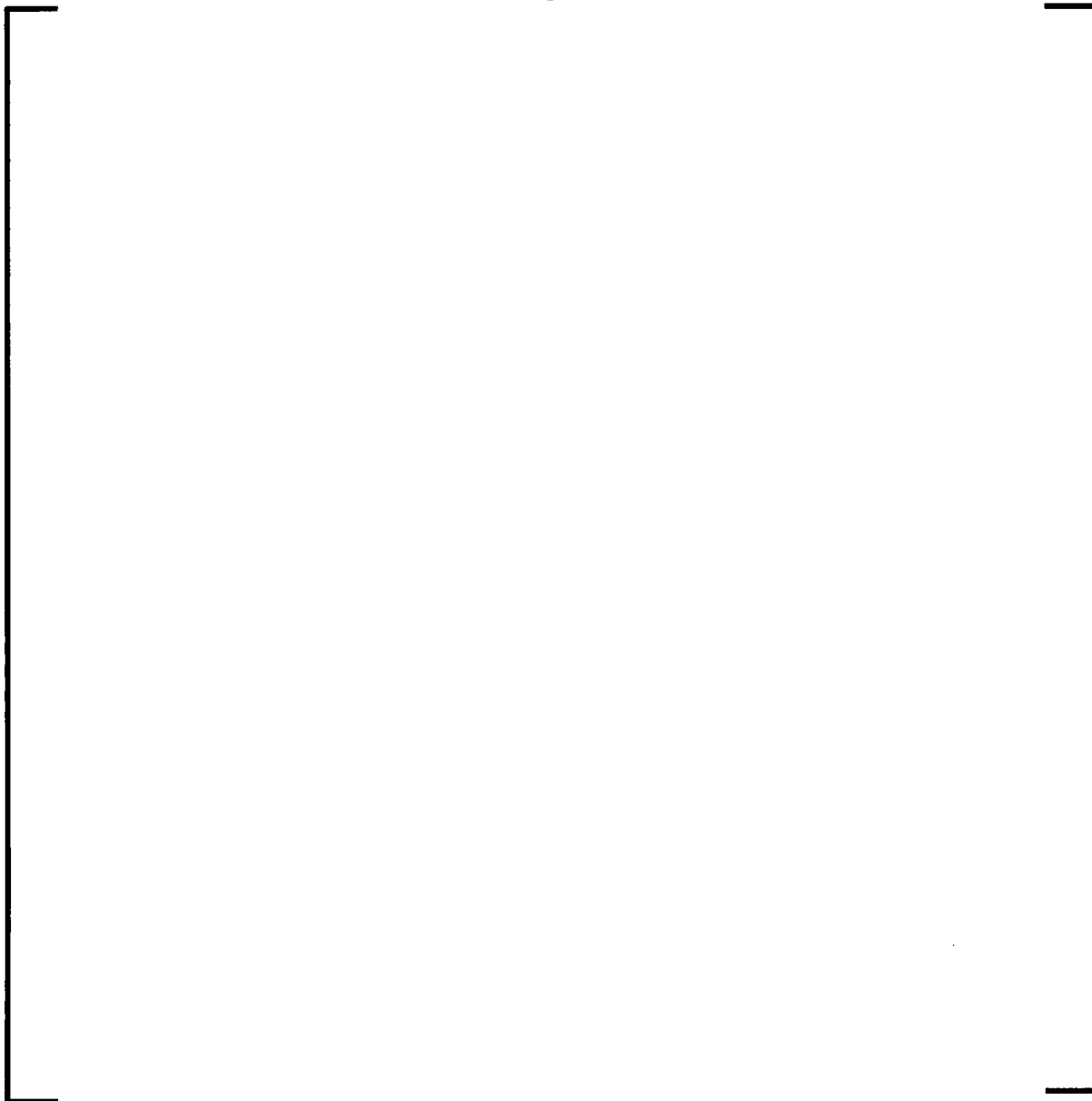


Figure 4-45—U.S. EPR Fuel Assembly Impact Test – Detailed Spring Arrangement



The external stiffness in the case of the fuel assembly to the heavy reflector impact model is two times that of the assembly-to-assembly impact, since one of the impacting bodies is infinitely stiff. The equivalent stiffness and damping are related to the internal and external stiffness/damping by:

$$\frac{1}{K_{EQV}} = \frac{1}{K_I} + \frac{1}{2K_E}$$

Equation 4-20

And,

$$\frac{1}{C_{EQV}} = \frac{1}{C_I} + \frac{1}{2C_E} \tag{Equation 4-21}$$

The benchmarking process consists of adjusting K_{EQV} and C_{EQV} parameters to match the measured impact force, and then using the K_E and C_E parameters determined from the spacer grid dynamic tests to back calculate the K_I and C_I parameters. When performing these calculations, the parameters are scaled to uniform temperature based on the value of the elastic modulus. The values are listed in Table 4-11.

The values of grid external stiffness and damping are taken as the average of the test sample. This is acceptable based on the sensitivity study reported in AREVA NP, ANP-10285Q9P, Response to Sixth Request for Additional Information (Reference 8), where the maximum and minimum grid stiffness and damping values from the grid test sample were used in the analysis of a limiting core model and time history. The conclusions of that study indicated that the variability in the reported peak impact loads is below [] with respect to the average stiffness and damping case.

Table 4-11—U.S. EPR Grid Stiffness and Damping – Operating Temperature

--

4.1.6 Analysis Software – The CASAC Code

CASAC is a general-purpose structural code designed to solve a wide range of mechanical problems. This software is dedicated to the study of structures composed of slender parts, concentrated masses, and connecting elements featuring linear or non-linear behavior. With the CASAC package, numerical solutions can be obtained in 4 different cases:

- Steady-state and stability analyses of non-linear structures.
- Modal analysis of linear and linearized structures including spectrum response.
- Time dependent solutions for elastic, elastic-plastic and visco-plastic structures.
- Transient response of non-linear structures subjected to dynamic loadings.

4.1.6.1 CASAC Program Scope

Regardless of complexity and size, the CASAC computer program handles all types of structural models, among which the following two models are most frequently analyzed with CASAC:

- Mass-spring models, which generally allow analysis of the axial behavior of linear or non-linear mechanical systems along one single axis.
- Models featuring beams interconnected by linear or gapped springs, sticking/sliding friction elements, generalized contact elements and/or fluid/structure coupling elements. These elements simulate the lateral behavior of buildings (seismic analysis of concrete structures), or of mechanical equipment (analysis of vibrational response, earthquake resistance).

These types of models are shown in Figure 4-1, Figure 4-9, Figure 4-17, Figure 4-41, Figure 4-42, Figure 4-44, and Figure 4-45, which illustrate the possibilities of the various elements.

4.1.6.2 CASAC Program Analysis Capabilities

4.1.6.2.1 Static Analysis

Static analysis provides the static equilibrium solutions of a structure subjected to loadings consisting of forces and moments, imposed displacements and rotations, thermal elongations, and irradiation induced growth. The states of equilibrium are defined by:

- Nodal displacements.
- The state and internal forces of non-linear elements.
- Internal forces and stresses in the linear components (springs, beams elements).
- Support reactions.

Once the model has been qualified, prediction is also provided of structural behavior in an environment that is different from that of the reference tests (hot conditions, for example).

4.1.6.2.2 Quasi-Static Analysis of Visco-Plastic Structures

Similarly to the static analysis resolution, time dependent solutions can be determined for visco-plastic structures. Since local values of strains and stresses are not readily available within structural elements, only linear (viscous) creep can be considered in these models. Depending on the loading mode of the structure under consideration, the model will exhibit pure creep, pure relaxation or mixed creep and relaxation response in the case of combined primary and secondary loadings.

Creep can be taken into account in every kind of structural element where elastic scalar relationships can be isolated for each deformation mode. Consequently, with exception of super elements, which cannot be reduced to a set of scalar elastic relationships, every available modeling element is eligible for visco-plastic deformation.

4.1.6.2.3 Modal Analysis

Modal analysis provides the calculation of the vibration eigenmodes of the analyzed system, namely the eigenfrequencies and eigenvectors (mode shapes), together with generalized masses and stiffness.

A direct comparison with tests ensures that the calculation model correctly represents the analyzed structure. The qualified model can then be used for eigenmode calculations in environments that differ from those used for the tests, such as those in water and under hot conditions.

4.1.6.2.4 Transient Dynamic Analysis

Transient dynamic analysis determines the time solutions of a structure subjected to dynamics loads. Dynamic equilibrium at each time step is given by:

- Nodal displacements, velocities, accelerations and elastic forces.
- The state and internal forces of non-linear elements.
- Stresses in the beam elements.

These calculations are generally used to design or verify structures subjected to earthquakes and LOCAs, but this type of analysis may also be applied to other problems, such as:

- The calculation of control rod drop impact.
- The calculation of the vibrational response of a fuel rod in grid cells.

The following two resolution methods are available:

- Direct integration of equations by an explicit integration scheme.
- Linear or non-linear modal superposition (non-linear behaviour restricted to gapped springs).

4.1.6.3 CASAC Program Advanced Analysis Features

4.1.6.3.1 Visco-Elastic Gapped Element Activated in Displacement and Force

The visco-elastic gapped element used for spacer grid modeling in core row models has a special feature. When contact is impending, the element is activated by monitoring the relative displacement of the nodes, and when gap closure is detected, the element is activated. For deactivation, the criterion is switched to the total element force, which includes the elastic and viscous component.

4.1.6.3.2 Damping in the Relative Coordinate System

In the case of most commercial finite element codes, the damping matrix multiplies the velocity vector, which is expressed in the global Cartesian coordinate system. This can create spurious damping forces, which are numerically generated, and have no physical basis. One example is the damping on the fuel assembly, which is governed by forces generated by the relative motion of the fuel assembly with respect to the core plates, which, in turn, have an imposed motion derived from the reactor internals model. Applying the damping matrix on the absolute velocity vector would produce unrealistic damping forces. The CASAC code offers the option to define the damping as acting on the differential velocity vector of the structure, defined as the absolute velocity vector minus the velocity vector of one of the core plates.

4.1.6.3.3 Large Displacement/Rotation of Beams

The beam formulation implemented accounts for both Euler (pure flexion) and Timoshenko (flexion + shear) approximations. CASAC models can therefore represent structures made up of either slender or short beams or both.

The non-linear theory of beams is fully implemented in the steady-state and visco-plastic analyses. This non-linear feature makes CASAC an adequate tool for analyzing the creep-buckling phenomenon.

The non-linear theory of beams is also involved in the stability analysis of reticulated structures providing a useful tool when the structures analyzed exhibit a high degree of complexity, which makes hand calculations difficult.

The stress stiffening effect derived from the non-linear beam theory is also considered with all linear options, which makes it available for modal analysis and for the dynamic analysis of cases with prestressed structures such as fuel assemblies subjected to hold-down forces.

4.1.6.3.4 Mixed Modal-Rayleigh Damping Modeling Technique

Damping is a critical feature in the determination of time solutions for structures subjected to external dynamic loadings. Particular attention is given to the modeling of the dissipative forces that dampen the dynamic response of the structures analyzed.

The traditional damping modeling technique used for direct integration of the dynamic equations, known as Rayleigh damping, is widely accepted. This model is well-suited for structures in which the dissipative forces are neither fully identified, nor fully characterized. Besides its simplicity, the main advantage of this method is that the damping matrix meets the orthogonality criterion of the real modes obtained from the system mass and stiffness matrices. A reduced damping coefficient (proportion of critical damping) can therefore be expressed for each mode of the structure. Not only can the critical damping ratio be expressed, but it can be imposed on two natural modes of distinct frequencies. Generally, the two modes showing the highest participation for the dynamic excitation applied are considered for adjusting the Rayleigh damping parameters. This method provides enough flexibility to satisfy most of the needs encountered with the structures analyzed in the mechanical engineering of the fuel assembly.

Implementing modal damping in the direct integration of time solutions can be interpreted as an extension of the Rayleigh damping, by allowing the specification of reduced damping values to several natural modes of the same structure, with no

limitation in the number of modes. This method is complementary to the traditional Rayleigh damping technique, which is automatically applied to modes that are not specifically assigned a reduced damping value. This method is well-suited for the multiscale approach, which becomes a necessity by the new requirements to integrate an extended range of frequencies in the seismic analyses.

This unique feature also makes it possible to set the damping parameters for a given set of boundary conditions, and to apply the damping properties onto different configurations. Typically, the fuel bundle damping properties are characterized by using flow test results for fixed-fixed boundary conditions at both ends. During a seismic event, the fuel bundle response determination requires different motion time histories to be imposed at both ends. This is achieved by using free-free modes with a traditional modal superposition method. CASAC uses a direct integration method, which can inherently handle changes in the boundary conditions while applying the damping parameters defined for a specific configuration that might be different from that used in the postulated events.

Consistent with the method approved in Addendum 1 of BAW-10133PA (Reference 2), the modal damping feature is not used in the U.S. EPR analysis.

4.1.6.4 CASAC Program Validation

The validation of the CASAC program for the purpose of performing seismic and LOCA analyses for reactor core models is further detailed in Reference 7. The capabilities were tested against fuel assembly pluck tests with impacts, and against a full-scale experimental investigation of six fuel assemblies in a row in water under lateral seismic excitation, as shown in "Validation of PWR Core Seismic Models with Shaking Table Tests on Interacting Scale 1 Fuel Assemblies" (Reference 14).

The single assembly free vibration during a pluck test is compared to the CASAC model predictions in Figure 4-46. The multi-assembly forced response under a simulated earthquake time history is compared to CASAC predictions in Figure 4-47. Finally, the

comparison between the tested and calculated maximum grid impact loads for a number of 15 accelerograms is shown in Figure 4-48.

**Figure 4-46—Comparison of CASAC Model and Test – Free Vibration
(in air)**

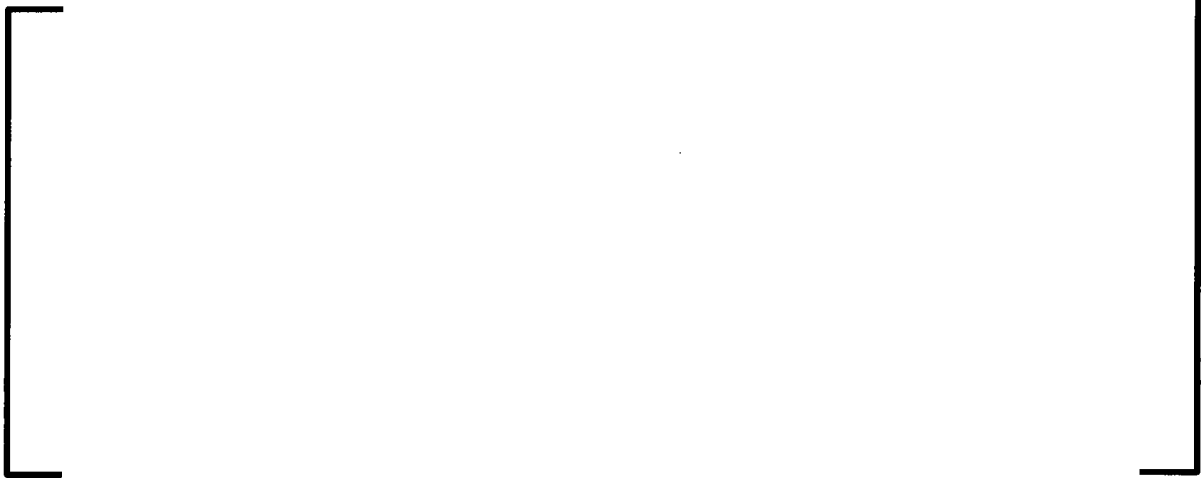


**Figure 4-47—Comparison of CASAC Model and Test - Displacements
(in air)**



**Figure 4-48—Comparison of CASAC Model and Test Impact Loads
(in water)**



The statistical comparison of the CASAC calculated versus tested maximum grid impact loads is summarized in Table 4-12.

**Table 4-12—Comparison of CASAC Model and Test Impact Loads
(in water)**

All the preceding plots and tables demonstrate the capability of the CASAC code to adequately predict fuel assembly dynamic response and component loads in air and in water for a wide range of input seismic time histories.

4.2 U.S. EPR Vertical Seismic and LOCA Methodology

This section discusses the fuel assembly vertical seismic and LOCA loading analysis methodology. In principle, the vertical methodology used for the U.S. EPR follows the

model architecture, benchmark, and numerical solution outlined in AREVA Topical Report BAW-10172(PA), "Mark-BW Mechanical Design Report" (Reference 11), with some refinements and additional steps.

The methodology involves the modeling of only one fuel assembly. The underlying assumption being that each assembly moves independently in the vertical direction. The model is then subjected to the seismically-imposed displacement time-history applied at the core plates, and to the LOCA loading time-history, which consists of hydraulic loads applied to the main pressure drop locations in the assembly, such as the spacer grids and the top and bottom nozzles. The response is post-processed to produce maximum component loads, which are then combined with the lateral loads and used as either inputs for the component stress analysis, or for a direct comparison with component tested collapse loads.

The model is built based on design verification testing results, which provide certain critical fuel assembly static and dynamic response characteristics under specified loading, that are then used as a target output in the process of fuel assembly model creation, benchmarking validation. The two types of tests performed in support of the vertical model development are the fuel assembly axial stiffness test, and the vertical drop test.

Given that this model is used for faulted condition analysis, it is important to indicate that the degree of refinement of the model is only commensurate with the accident operation analytical requirements. The detailed load distribution at the individual fuel rod or guide tube level is, therefore, not of interest in this case. The detailed stress distribution in the top and bottom nozzles is not the main focus either. The main focus of accident condition analysis is net section loads, which are considered as being evenly distributed over the fuel rods or guide tubes. These average loads are then compared to the component capability either on a linearized stress basis, or a tested collapse load basis. Consequently, the vertical faulted analysis model used for the U.S. EPR is based on the following engineering simplifying assumptions:

- All points on the fuel rods move in the same fashion. A horizontal planar section through the fuel rods remains horizontal and planar. This is an approximation, which discards the bending stiffness of the spacer grids, and results in conservatively higher loads between the grid and the guide tube. Also, at EOL, this statement means that the bottom nozzle upper face does not bend under the inertial load of the fuel rods. This modeling approach means that the models will only be able to predict the total force exerted on the bottom nozzle by the fuel rods and the guide tubes, but not the spatial distribution of this force.
- All horizontal and planar sections through the guide tubes remain horizontal and planar. The "horizontal" part of this statement is an approximation which discards the possible bending of the fuel assembly. Since the fuel assembly, as a structure, does not have coupled vertical-horizontal modes of vibration, the approximation is deemed acceptable.
- The support of the guide tubes from the bottom nozzle can be described as a simple linear spring and damper combination. The spring lumps together the bending stiffness of the bottom nozzle and the impact stiffness between the bottom nozzle and the core support plate.

4.2.1 U.S. EPR Vertical Seismic and LOCA Model Architecture

Consistent with the overall assumptions discussed, the general architecture of the vertical faulted analysis model, as shown in Figure 4-49, consists of two columns representing the guide tubes (Elements 1-13), and the fuel rods (Elements 14-24). The two beam element columns comprise the linear part of the model. All nodal degrees of freedom (DOFs) in the lateral and rotational directions are constrained. To account for the presence of the MONOBLOC™ Guide Tubes, the cross-sectional properties of the beam elements are different in the dashpot portion extending from the top face of the bottom nozzle to the mid-point of the wall thickness transition. The top nozzle and bottom nozzle are represented by short beam elements (Elements 28 and 27 in Figure 4-49). The spacer grids are included in the model as point-mass elements only on the guide tube column. The stiffness of the fuel rods is considered to be

concentrated in the cladding. In taking this modeling approach, an engineering judgment is made to the effect that the stiffness of the pellets and plenum springs does not affect the external stiffness of the fuel rod. For the BOL condition, where the pellets can move inside the fuel rod, the approach can be justified by the fact that the plenum spring stiffness is usually two orders of magnitude lower than the axial stiffness of a fuel rod cladding. For the EOL condition, the impact load path moves directly from the fuel rod to the bottom nozzle, and therefore, the axial stiffness of the fuel rod is less important. The two columns in the model are offset laterally to allow for the visualization of the displacements. No extraneous reaction forces or moments are produced as a result since the lateral and rotational DOF are restrained.

The non-linear capabilities of the model consist of a number of gap-springs, gap-dampers, and slider elements, as shown in Figure 4-49. A brief discussion of these elements follows:

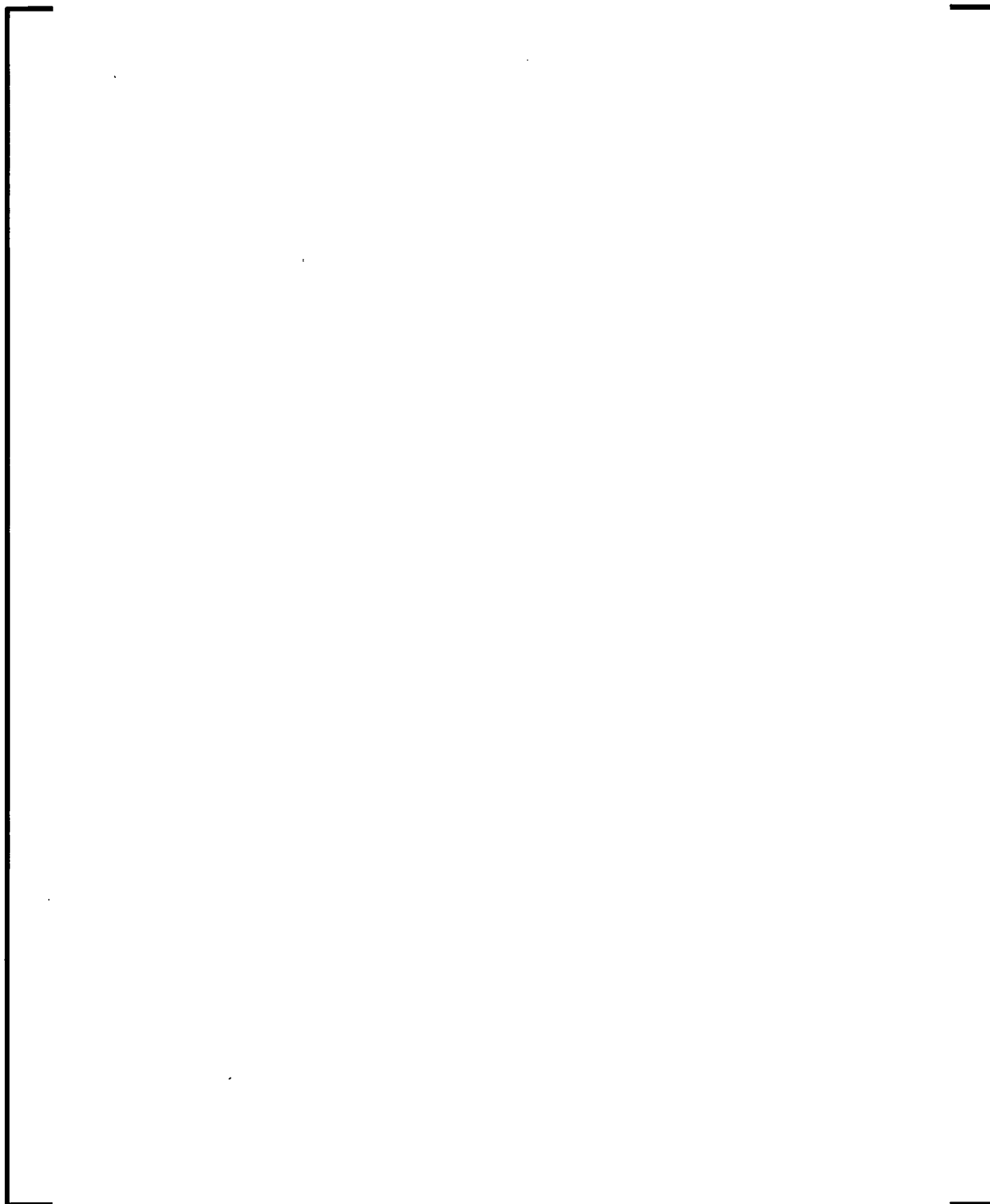
- The non-linear gap-spring-damper element between the bottom nozzle and ground (Element 40 in Figure 4-49). The stiffness of this element is used to account for the stiffness of the load-path between the guide tube embossments and ground for the BOL case, and from the bottom nozzle upper face and ground for the EOL case. In the EOL case, the load is distributed on the upper face of the bottom nozzle, since the fuel rods are resting against this surface. The actual value of the element stiffness is adjusted to match the fuel assembly axial stiffness and drop test results, and is also compared to the static test stiffness of the bottom nozzle from the component test. This is to verify that the model stiffness is sufficiently similar to the measured component stiffness. The element also has the damping capability activated. This constant is adjusted to match the fuel assembly rebound height after the first, and possibly subsequent impacts.
- The non-linear gap-spring-damper element between the fuel rod lower end and the top face of the bottom nozzle (Element 25 in Figure 4-49). The element gap is a function of the BOL or EOL condition. At BOL, the gap is open since the rods are lifted and remain lifted as shown by the drop tests. At EOL, the gap is

closed since the rods are seated on the upper face of the bottom nozzle and the impact load is carried through the stiffness of the bottom nozzle grillage. The stiffness and damping of this spring element are adjusted to remove the high frequency response of the bottom nozzle node in the EOL case. Although the drop test results do not show this response, the model results would, if a very large stiffness value were used.

- The non-linear gap-spring-damper element between the top of the fuel rods and the top nozzle (Element 26 in Figure 4-49). The characteristics of this spring are similar to Element 25, with the gap being different. This gap is designed to remain open over the service life of the assembly under normal operating conditions (including irradiation growth), but could close due to impacts produced by seismic or LOCA loading.
- The non-linear slider elements act between the fuel rod nodes and the corresponding spacer grid nodes on the guide tube column (Items 29 to 38 in Figure 4-49). The stiffness (or slope) of these elements is adjusted to match the assembly axial stiffness test results. The saturation force in the element is initially set according to previous fuel rod spacer grid slip load tests, but is later adjusted to match the dynamic effects of the drop test.

These elements constitute the model to be benchmarked to the verification tests. Additional elements and model adjustments are necessary to effectively simulate the fuel assembly at hot operating conditions for the faulted analysis, and are discussed in Section 4.2.3.

Figure 4-49—U.S. EPR Vertical Seismic and LOCA Model



4.2.2 U.S. EPR Vertical Model Design Verification Testing and Benchmarking

Given its built-in, non-linear characteristics, the vertical faulted analysis model has the following predictive capabilities:

- The fuel assembly axial stiffness under axial loading applied at the top nozzle. The BOL stiffness should be constant over a range of 0-to-2-g axial loads due to the large slip load capability of the fuel rod to the spacer grid connection.
- The free airborne motion, and the peak impact load at the impact of the fuel assembly on the lower core plate.
- The rebound velocity after the axial impact.
- The top nozzle and bottom nozzle overall impact loads – total load only (i.e., without the spatial distribution).
- The Upper Connection and Lower Connection loads – total load for all guide tubes.
- The Guide Tube and Instrument Tube loads at every span – total loads only.
- The Fuel Rod loads at every span and the impact loads with the bottom nozzle and top nozzle respectively – total loads for all fuel rods only.
- The Spacer Grid to Guide Tube connection loads – total loads for all guide tubes.

Given the scope of predictive capabilities that the vertical faulted analysis model requires, the model construction proceeds in multiple steps:

- Assign all the known material and net section properties of the beam column elements based on generic material property data at 70 °F, and closed-form equations based on first principles.
- Assign the static stiffness of the bottom nozzle and top nozzle based on component test data.
- Assign the grid-to-fuel-rod slider slip load at BOL based on fuel rod/spacer grid global slip load measurements.

- Adjust the grid-to-fuel-rod slider stiffness at BOL based on the measured fuel assembly axial BOL stiffness test.
- Readjust the bottom nozzle and slider stiffness to match the drop test peak impact load and the rebound velocity.

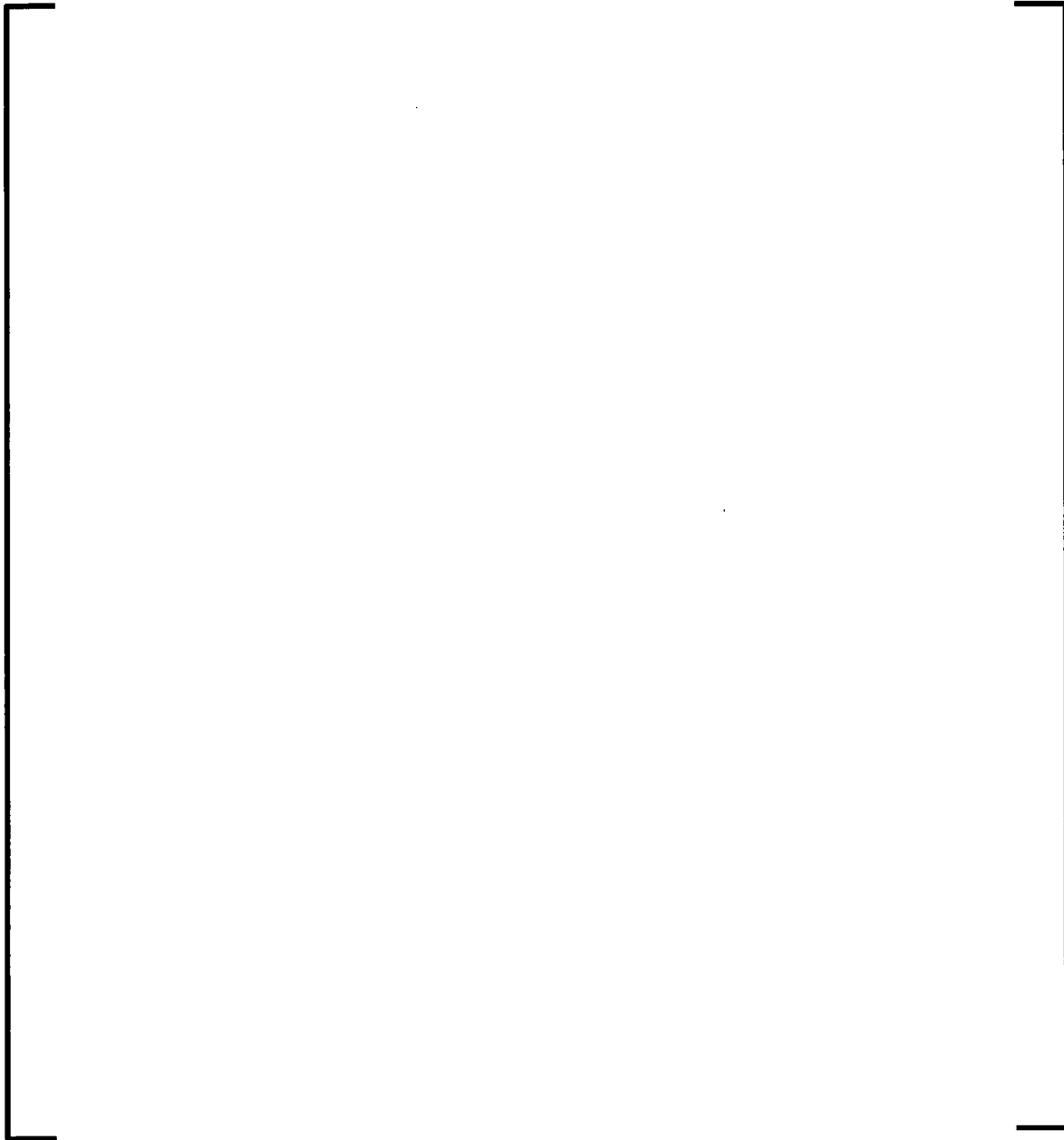
From the preceding discussion, it is apparent that the tested assembly behavior under both static loading (axial stiffness test) and dynamic loading (drop test) is used as the target model behavior, and the non-linear element characteristics in the model are used as parameters to be adjusted in order to match the target behavior.

4.2.2.1 Vertical Testing Description

4.2.2.1.1 Axial Stiffness Test

The general test arrangement is shown in Figure 4-50. The assembly is instrumented axially (configuration "A") and laterally (configuration "B") at the top nozzle, and at several spacer locations with linear variable differential transducers (LVDTs). The fuel assembly is secured at the top and bottom nozzles with a simulated core plate fixture. A screw jack is mounted between the simulated core plate and the upper support structure. A load cell is mounted between the lower support plate and the floor plate. The jack is used to apply the load, and the load cell measures the applied load. LVDTs are used to measure the deflection at each of the locations with respect to a fixed reference. The test data consist of assembly axial deflection (measured at all instrumented elevations) versus axial load, and lateral displacements (in both orthogonal directions) of one of the grids closest to the bundle mid-height. This is to validate that the lateral deflection is minimal, and does not interfere with the axial deformation of the bundle. Excessive lateral deflection can lower the measured axial stiffness of the fuel assembly.

Figure 4-50—U.S. EPR Vertical Stiffness Test Arrangement



4.2.2.1.2 Axial Drop Test

This axial drop test simulates the loading on the fuel assembly components during the lift-off and impacts caused by a seismic or LOCA event. For a LOCA event, when the hydraulic pressure on the spacer grids increases as a result of increased coolant flow

rate, the assembly may be lifted off the lower core plate. The subsequent fuel assembly drop motion causes impacts on the bottom nozzle, guide tubes, and fuel rods. It is for this reason that the faulted analysis model must be able to accurately predict these loads. The vertical drop test simulates this phenomenon, where the assembly is lifted by a distance of [] from the base plate, and dropped. The displacements at the bottom nozzle and at several grids, together with the impact force, are recorded as a function of time. The test offers the possibility of quantifying the relation between the incoming kinetic energy and the peak impact force at the bottom nozzle.

4.2.2.2 U. S. EPR Vertical Model Characteristics and Benchmarking Results

The model characteristics are listed in Table 4-13, Table 4-14, Table 4-15, Table 4-16, and Table 4-17. The weight comparison in Table 4-13 is listed for both the dry and the wet assembly, and serves to validate both the hardware model (the dry weight) and the hydrodynamic coupling elements (Section 4.2.3). The guide tube and fuel rod properties (Table 4-14) are derived analytically from design parameters.

Table 4-13—Model and Actual Fuel Weights

--	--

Table 4-14—Guide Tube and Fuel Rod Properties

--	--

The gap element properties (Table 4-15), the end fitting element properties (Table 4-16), and the spacer grid properties (Table 4-17) have been adjusted to match the axial stiffness and drop test results.

Table 4-15—Gap Element Properties

--

Table 4-16—Top and Bottom Nozzle Properties

--

Table 4-17—Spacer Grid Properties

--

With these model characteristics, the results of the axial stiffness benchmark are shown in Figure 4-51. The tested axial loading results show a practically linear trend, and the model predicted loading curve is in very good agreement with the test results.

Figure 4-51—Axial Stiffness - Model & Test



Note: The abbreviation UTP stands for Upper Tie Plate, which refers to the Top Nozzle.

The drop test comparison is shown in Table 4-18. The model calculated impact velocities and the peak impact force compare well with the tested results.

Table 4-18—Drop Test Benchmarking Summary



4.2.3 U.S. EPR Vertical Model – Augmentation and Conversion for Seismic and LOCA Analysis

The following modifications were performed to the benchmarked model to facilitate the accident analytical simulations:

- Addition of hold-down spring element using the stiffness and preload values shown in Table 4-19.
- Reduction of various contact stiffnesses (bottom nozzle -LCP, FR- bottom nozzle, FR- top nozzle) based on material hot to cold E values outlined in Table 4-20.
- Reduction of spacer grid slip loads based on hot to cold E values, according to Table 4-20.
- Modification of E values of beam elements (GT, FR, BN and TN) to account for temperature effects, according to Table 4-20.
- Addition of hydrodynamic coupling elements to account for coolant in a confined environment. The concept is the same as discussed in Section 4.1.2. The added and coupling mass coefficients are [

]. The displaced water mass values and the subsequent added and coupling masses are presented in Table 4-21 and Table 4-22.

- Inclusion of damping by using damping elements between the LCP and the guide tube and fuel rod nodes. The damping coefficient of these elements was adjusted to achieve a damping ratio (ζ) of 4% as recommended in Table 1 of Reference 9 for faulted conditions.

Table 4-19—Hold-down Spring Properties

--

Table 4-20—Young's Modulus Values

--

Table 4-21—Displaced Water Mass

--

1) Water density @ 315.5°C & 15.5MPa =.692 kg/m³.

Table 4-22—Added and Coupling Masses on Guide Tube and Fuel Rod Nodes

--

For the irradiated (EOL) condition analysis, some further modifications to the model parameters were implemented as follows:

- ISG slip load - Reduced to []
- Upper end grid (UEG) slip load - Reduced to []
- Lower end grid (LEG) slip load - Reduced to []
- Fuel rod- bottom nozzle contact element - Gap reduced from [], which simulates rod seating.
- Fuel rod- top nozzle contact element - Gap reduced from [] (to simulate rod growth at EOL). Note that this element does not change the results since there is no contact at this interface during the simulations.

4.3 U.S. EPR Seismic and LOCA Load Combination and Non-Grid Component Stress Analysis Methodology

This section addresses the load combination technique and the component stress analysis for the U.S. EPR fuel assembly. The core row models and the vertical fuel assembly model described in Sections 4.1 and 4.2 produce fuel assembly

displacements and component loads. Of these, only the impact loads on the spacer grids can be compared directly to test-based grid allowable crushing loads for the purpose of calculating design margins. For the remaining components, an additional analysis step is needed to produce the detailed loads or stresses that can be compared directly to allowable loads or stress limits.

The first step in this analysis process is the construction and benchmarking of the detailed 3D FEM. The model consists of beam elements and linear and non-linear springs, and contains a detailed representation of each guide tube in the fuel assembly, and a lumped representation of the [] fuel rods grouped into four equivalent beam columns. The spacer grids and the top and bottom nozzles are represented as planar reticulate structures. The interaction between the spacer grids and the guide tubes and fuel rods is modeled as a combination of linear and non-linear springs, which are capable of replicating the non-linear behavior at this joint. The model is benchmarked against the lateral stiffness tests on the un-irradiated and irradiated bundles (BOL 2003 and EOL 2005 described in Section 4.1.1.2.3), and is capable of reproducing the non-linear loading curve from these tests. Further details are described in Section 4.3.1.

The second step consists of defining the load combination methodology by following the techniques from Regulatory Guide 1.92 (Reference 3). For every event (seismic or LOCA, as described in Section 5.1), for every frequency sweep case (as described in Section 4.1.1.3), and for every combination of core row models, the results for the two rows are scanned to detect the highest resultant end moment at the top nozzle and bottom nozzle from the two lateral directions. The lateral displacements associated with the maximum top and bottom nozzles are applied on the 3D non-linear FEM, and component loads are produced. The peak values from the two cases, for each of the nine frequency sweep cases are used for subsequent analysis. The limiting horizontal and vertical component loads from SSE and LOCA are combined on a square root of sum of squares (SRSS) basis and added to the normal operating loads, as detailed in Section 4.3.2.

The last step of the analysis consists of defining the acceptance criteria and calculating the design margins for each component. The criteria are expressed either in terms of stress limits, or allowable loads, and are consistent with the ASME Code Section III, Division 1, Appendix F, Level D, limits (Reference 4), with the exception of the guide tubes and upper connection, which are limited by Level C criteria combined with buckling limits to ensure the control rod insertion path. Also, the fuel rods have specific stress criteria in conjunction with buckling limits. Further details are provided in Section 4.3.3.

4.3.1 Non-Linear 3D U.S. EPR Fuel Assembly Finite Element Model

The detailed 3D U.S. EPR fuel assembly FEM has been developed using the general purpose structural program CASAC (described in Section 4.1.6) and is based on a number of key modeling assumptions:

- The slender components in the assembly are modeled with linear material properties. This does not allow for any load redistribution, and makes the calculated stresses compatible with the ASME Code stress limits.
- The top and bottom nozzles are modeled as rigid regions. The connection between the guide tubes and the nozzles is conservatively modeled as clamped.
- The spacer grids are modeled as rigid regions, essentially assuming that the spacer grid stays planar, but not necessarily in the horizontal plane. This discounts the inherent local stiffness of the spacer grid, and precludes load redistribution on both guide tubes and fuel rods.
- The fuel rods are lumped into four equal size groups, each group being represented by an equivalent beam column.

4.3.1.1 Non-Linear 3D U.S. EPR Fuel Assembly Finite Element Model Characteristics

The model (shown in Figure 4-54) contains [] beam columns representing each guide tube in the fuel assembly, placed at their actual physical location. The top and bottom nozzles are represented by two rigid regions implemented using constraint equations on the guide tube top end node's DOFs for the top nozzle, and, separately, on the guide tube lower end node's DOFs for the bottom nozzle. The connection between the guide tubes and the nozzle rigid region represents a clamped interface.

The fuel rods are represented as lumped into four beam columns, one for each bundle quadrant, combining the sectional properties of the fuel rods (sum of cross-sectional cladding area and moments of inertia) in that particular quadrant, and placed on the diagonals of the spacer grid at a distance chosen to match the bundle cross-sectional inertia.

The spacer grids are represented as rigid regions, implemented using constraint equations, and allowing translations and rotations, but forcing a planar configuration of the grid, and maintaining the guide tube and lumped fuel rod pattern. For a given spacer grid, the rigid region consists of a grid master node, placed at the appropriate elevation, and the guide tube nodes at that elevation. The differential linear DOFs on the guide tube nodes are connected to the rotational DOF of the master node.

The guide tube to grid connection represents a pinned interface. The linear DOFs on the guide tube remain on the grid rigid region at all times, while the rotational DOFs on the guide tubes are connected to the rotational DOFs of the grid master node via linear rotational stiffness springs in the two lateral directions.

The connection between the fuel rod to grid rigid region is implemented using non-linear spring and slider elements. In the axial direction, the fuel rod node is connected with the corresponding spacer grid rigid region node by a slider element (Figure 4-52) characterized by a "sticking stiffness" and a "slip load". The element is active on all grids in the BOL case, and only on the top end and lower end grids for the EOL case. The HTP M5[®] intermediate spacer grids [

]. The element constants for all these cases are listed in Table 4-23.

The lateral displacements of the fuel rod nodes are constrained to those of the grid rigid region. The relative rotations with respect to the two horizontal axes are connected via a non-linear rotational spring which mimics the rotational stiffness test results of a fuel rod segment loaded in an HTP grid cell. The generic characteristics and the conceptual implementation are shown Figure 4-53. The non-linear spring characteristic is the result of the superposition of one linear rotational spring which models the shallow stiffness of the HTP cell spring, and the two gapped springs which augment the stiffness when the fuel rod reaches the cell castellation. The linear stiffness, together with the angular gap and the gapped spring rotational stiffness are listed in Table 4-23. These parameters are adjusted during the benchmarking process to match the fuel assembly lateral stiffness test results. The element does not include the hysteresis effect, which results in a model that produces higher component stresses in the guide tubes. The details of the benchmarking process are presented in Section 4.3.1.2.

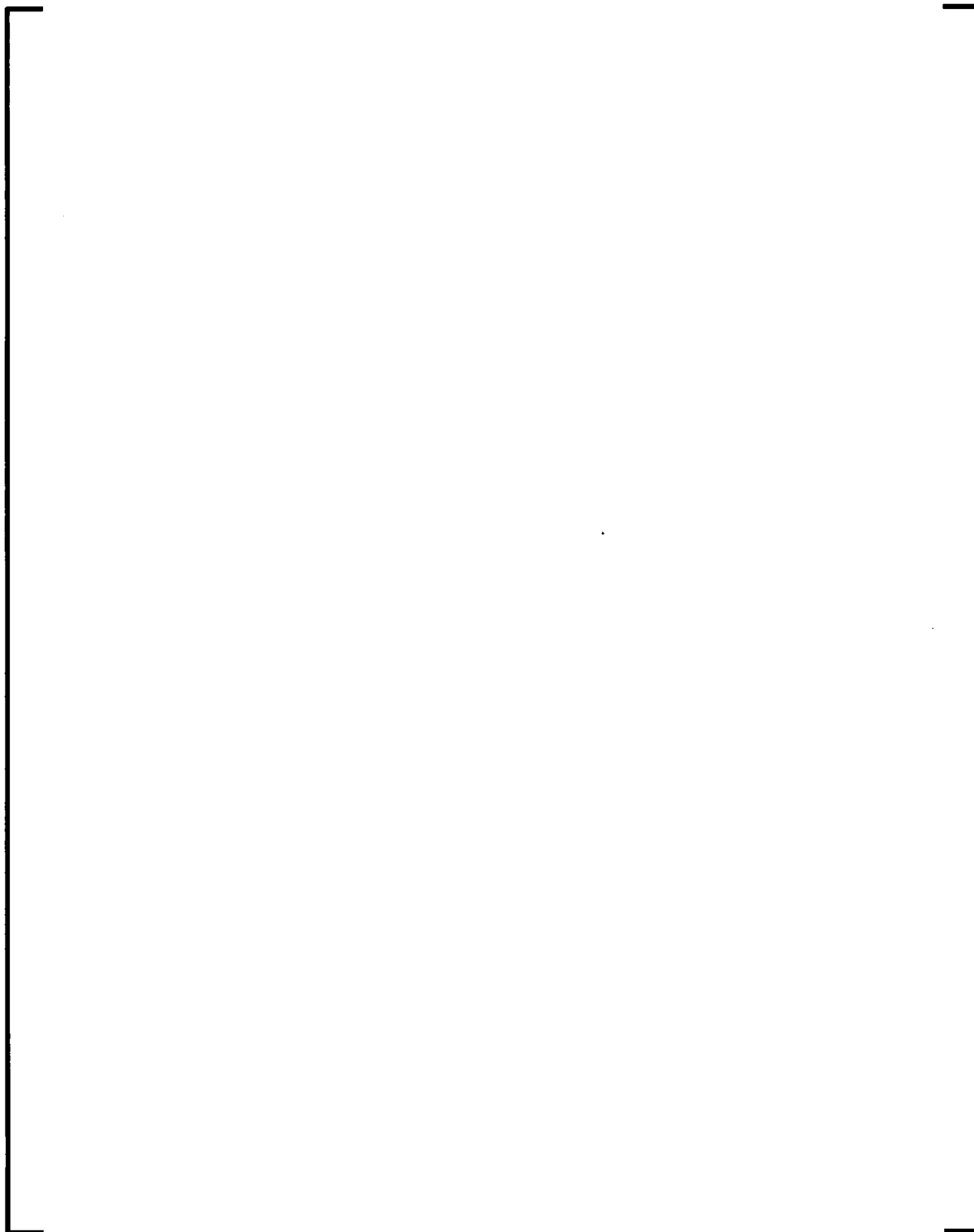
Figure 4-52—Axial Sliding Element at Fuel Rod to Spacer Grid Interface



**Figure 4-53—Non-Linear Rotational Spring at Fuel Rod to Spacer
Grid Interface**



Figure 4-54—U.S. EPR Non-Linear Finite Element Model Arrangement



4.3.1.2 Non-Linear 3-D U.S. EPR Fuel Assembly Finite Element Model Benchmarking

As described in Section 4.1.1.2.4, the tested configuration, HTP-LX, was almost identical to the U.S. EPR assembly, but did not match exactly. Therefore, the model benchmarking process involves three steps:

- First, the model of the HTP-LX fuel assembly is constructed and benchmarked to the test results. The reference test results are the BOL 2003 and EOL 2005 (Section 4.1.1.2.3) lateral stiffness tests. The EOL 2005 was chosen over the EOL 2012 because it indicates a higher lateral stiffness, and therefore, the model benchmarked to this test will predict higher component loads under imposed displacement. The HTP-LX model parameters are shown in Table 4-23, and the comparison between the test results and the model results is shown in Figure 4-55. For increased conservatism, the hysteresis effects are not modeled. This has the effect of increasing the predicted component loads. Therefore, the model loading curves match the loading portion of the tests curves. The model very closely captures the increased bundle stiffness at larger amplitudes, which is characteristic for the AREVA HTP fuel assemblies.
- Second, the input parameters of the benchmarked model are adjusted to reflect the U.S. EPR grid elevations, fuel assembly components, and material properties differences.
- Finally, the model is adjusted for operating temperature by modifying the elastic modulus of the slender components and the spring stiffness values. Table 4-24 lists all the characteristics of the U.S. EPR model at operating temperature.

Table 4-23—HTP-LX Model Structural Parameters

A large, empty rectangular frame with a thin black border, centered on the page. It is intended to contain the structural parameters for the HTP-LX model, but the content is currently blank.

Table 4-24—U.S. EPR Model Structural Parameters

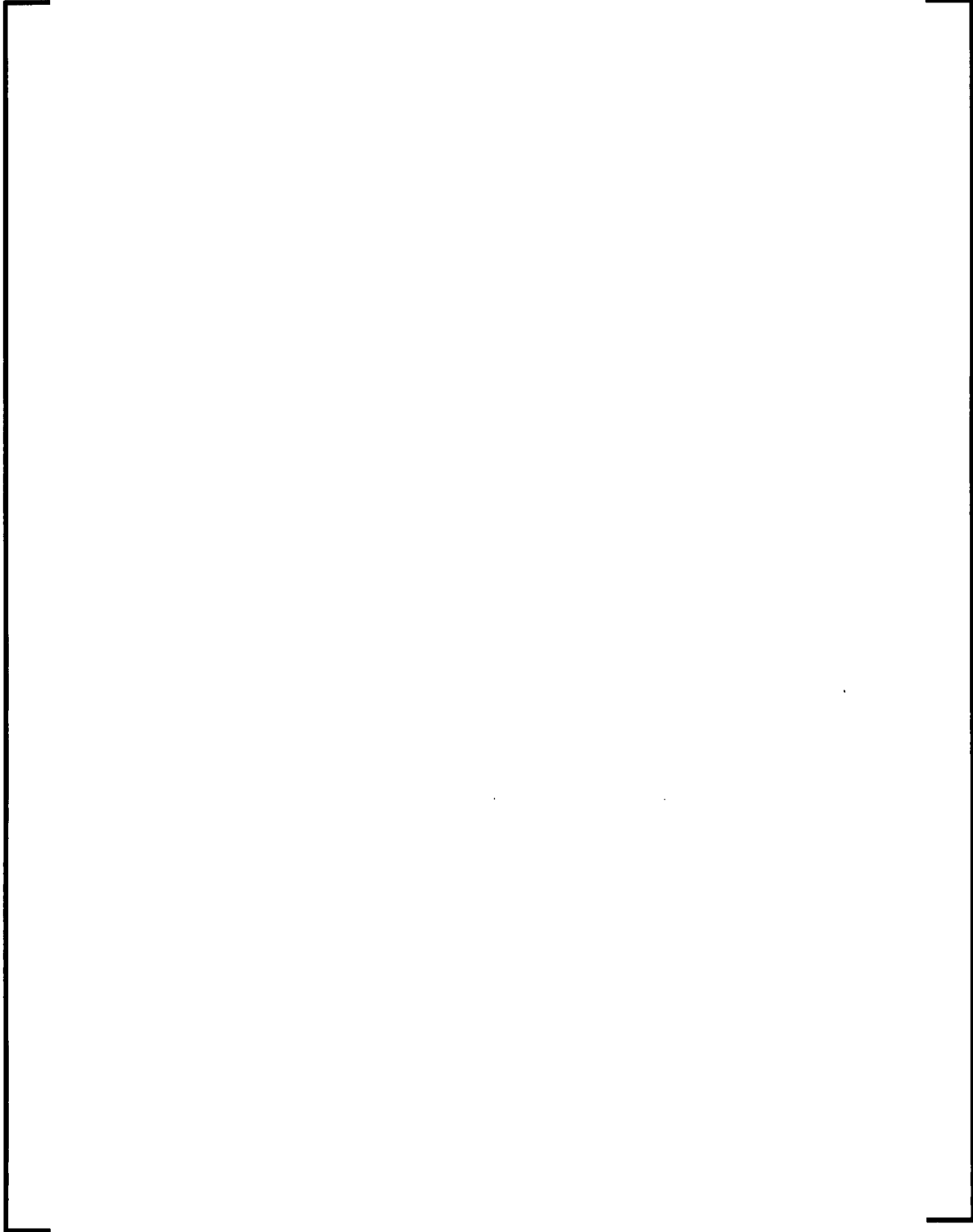
A large, empty rectangular frame with a thin black border, centered on the page. It is intended to contain the structural parameters for the U.S. EPR model, but the content is currently blank.



Figure 4-55—Irradiated and Unirradiated Model Benchmark



4.3.2 U.S. EPR Fuel Assembly Load Combination Methodology

The load combination method for the U.S. EPR fuel assembly follows the requirements of Reference 3. The fuel assembly component load contributions from three orthogonal directions produced by seismic and LOCA events are combined to the normal operating loads to produce the input to the stress evaluation or direct allowable load comparison.

The first step in this process is the two horizontal direction load combination, which is performed using the non-linear FEM and the results of the core row models for every seismic and LOCA event. The process consists of scanning the core row model results for the most demanding load case for every frequency sweep case (Section 4.1.1.3) for all seismic and LOCA events reported separately. The most demanding cases are decided based on the end nozzle moment indicator, whereby the bending moments at the top and bottom nozzle (treated as separate cases) are used as an indicator for the displaced fuel assembly configuration that will produce the highest fuel assembly component loads. The resultant end nozzle bending moments are calculated as vector resultants of the bending moments from every possible combination of two core row models using the data from the corresponding assembly in each row. The maximum end nozzle bending moment is decided without regard to time phasing, meaning that all possible two-direction combinations for a given event (seismic or LOCA) are tested regardless of whether the two perpendicular loads happen at the same time moment or not. Also, the maximum end nozzle bending moment is decided without regard to whether the row intersection producing the maximum actually exists in the core. This adds conservatism to this method, in addition to the conservatisms discussed in the preamble to Section 4.1. The maximum resultant end nozzle bending moment is decided for every frequency sweep case, over all fuel assemblies in the core, over all seismic scenarios, at the two end nozzles separately, and then similarly over all LOCA scenarios. This produces the list of potentially limiting cases, which are then analyzed using the non-linear FEM, by imposing the predicted displacements at each elevation from the two orthogonal directions, and performing a static solution, which produces the corresponding set of fuel assembly component loads. The set of potentially limiting

cases retained for detailed analysis is presented in Table 4-25 for the unirradiated condition, and in Table 4-26 for the irradiated condition.

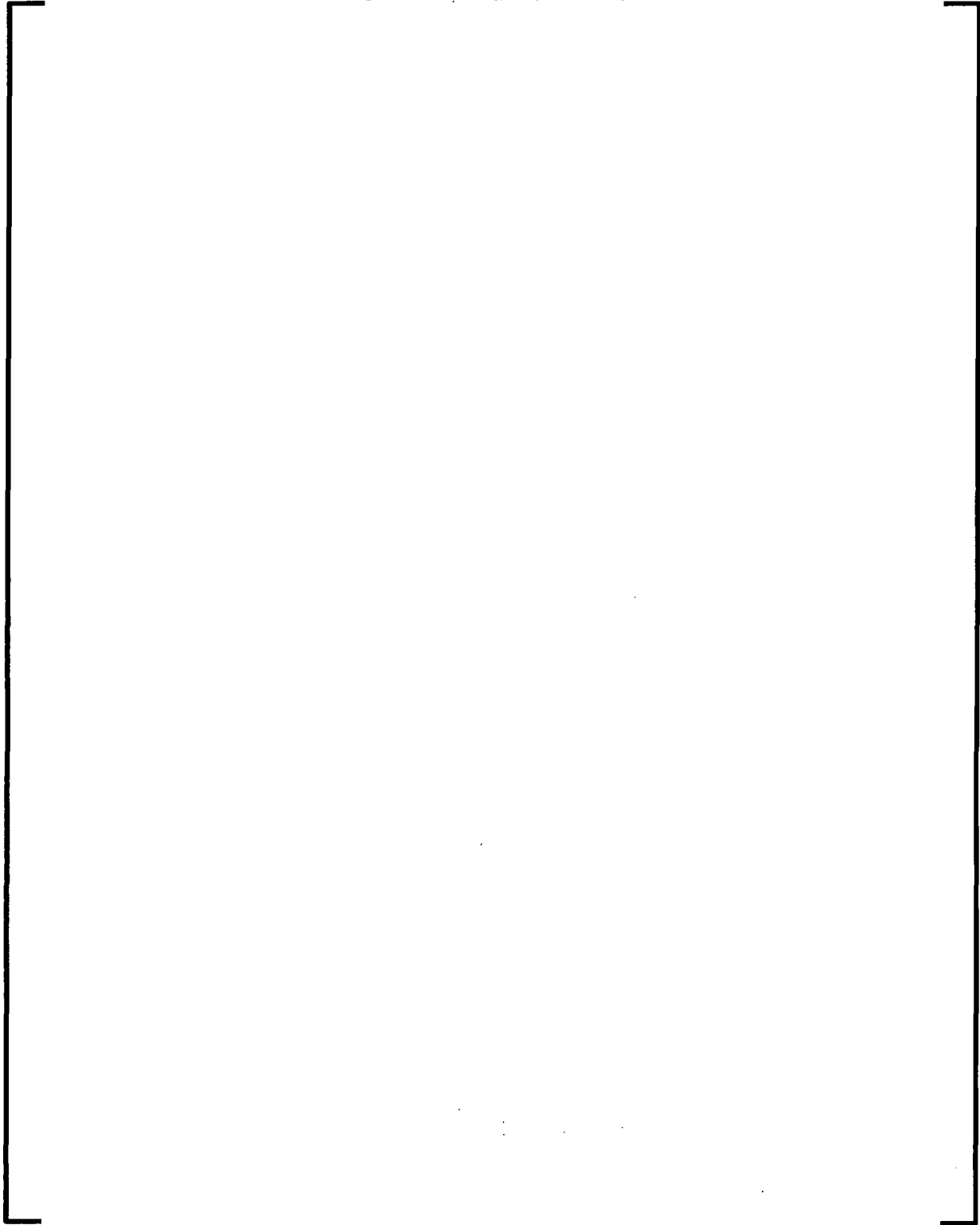
The second step in the load combination process consists of incorporating the component loads due to vertical direction excitation during seismic and LOCA events (accounted for separately). Since the vertical analysis is performed on a single fuel assembly, the vertical loads are combined with the horizontal loads on an SRSS basis, no detailed analysis using the non-linear FEM being necessary. Before combining the vertical loads however, the contribution of the faulted condition loading is isolated by subtracting the normal operating loads. This step is necessary because the vertical model analysis includes the normal operating loads. The final load combination is given by Equation 4-22 as:

$$L = L_{Normal\ Op} + \sqrt{L_{SSE\ Horiz}^2 + L_{LOCA\ Horiz}^2 + \Delta L_{SSE\ Vert}^2 + \Delta L_{LOCA\ Vert}^2} \quad \text{Equation 4-22}$$

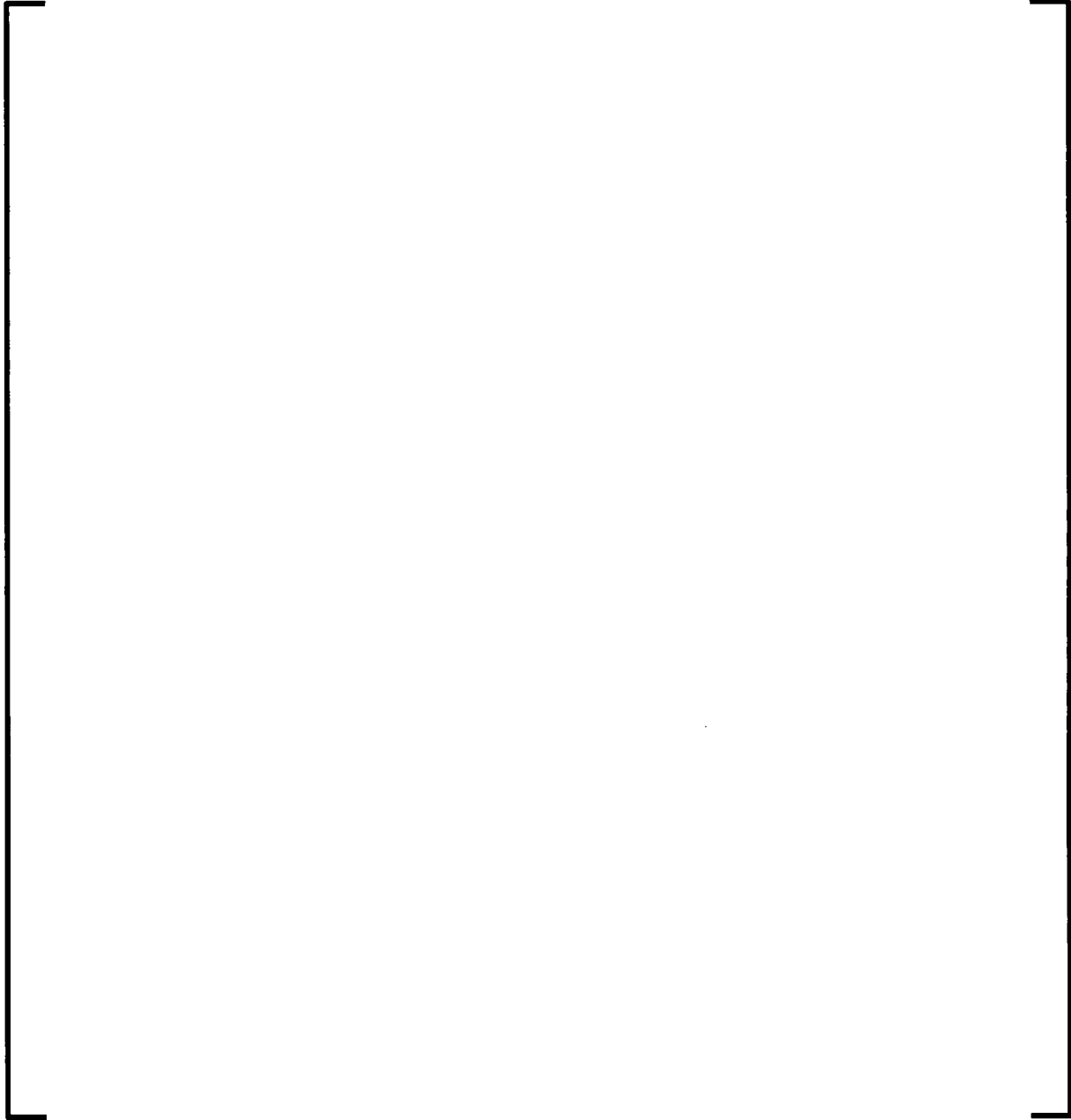
In Equation 4-22, L denotes component load (force or moment), and ΔL denotes the load differential of faulted load in the vertical model. This load combination is performed for all the horizontal loading limiting cases identified in Table 4-25 and Table 4-26, and the margin is reported as the smallest margin over all limiting cases.

For fuel rods, the normal operation loads are separate from the seismic and LOCA loads, and consequently, the full SSE vertical loads are considered in the SRSS operation.

**Table 4-25—Limiting Cases of Seismic and LOCA Loading –
Unirradiated Condition**



**Table 4-26—Limiting Cases of Seismic and LOCA Loading –
Irradiated Condition**

A large, empty rectangular frame with a thin black border, centered on the page. It is intended to contain the data for Table 4-26, but the content is missing from this scan.

4.3.3 U.S. EPR Fuel Assembly Non-Grid Components Acceptance Criteria

The acceptance criteria for fuel assembly components under faulted conditions were introduced in Section 2.3, in conjunction with the general design requirements discussed in Section 2.2. In this section, the acceptance criteria are discussed in more detail.

4.3.3.1 Acceptance Criteria for Guide Tubes

In Section 2.2 it was discussed that certain SSCs that are important to the safe shutdown of the reactor must maintain functional capability during and after the faulted event. Clearly, the guide tubes are in this category, since they provide the insertion path for the control rods. For this reason, the guide tubes stress and load limits must ensure the functionality of these components.

Also, in Section 2.2 it was pointed out that the criteria in 10 CFR 50 Appendix S do not require elastic operation of the safety-related components, and that non-elastic limits can be used. Further, these components can be qualified either by analysis or by test.

Taking these considerations into account, the guide tubes of the U.S. EPR fuel assembly are limited in terms of both stress, and buckling load. The stress limits are consistent with the ASME Code Section III Division 1 Sub-section NG Level C service limits, which means the elastically calculated primary membrane stress is limited by the yield strength of the material, and the primary membrane plus bending stress, or the local membrane stress, is limited to 1.5 times the yield strength. Positive margin to these limits ensures the guide tube maintains an elastic core, even if the outer fibers are allowed to undergo plastic strains. The magnitude of the strains is low, since they are controlled by the elastic core. In Appendix A.1 the ultimate ductility of the M5[®] alloy in irradiated state is shown to be [], which ensures no brittle fracture of the material under the low strains associated with Level C limits.

The buckling limit of the guide tube is in accordance with the requirements of SRP 4.2 (Reference 2), and it is imposed to ensure that the tube will not lose equilibrium stability

under the effect of axial compression (includes primary and secondary loading) even in the presence of a deflected configuration imposed by end of span bending moments.

The actual criterion is the buckling secant formula:

$$\sigma_{\max} = \frac{N}{A} + \frac{N \cdot \delta}{I/v} \times \sec \left(\sqrt{\frac{N}{P_{\text{crit}}}} \frac{\pi}{2} \right) \leq K \cdot S_y \quad \text{Equation 4-23}$$

Where:

σ_{\max} = Compressive load induced membrane plus bending stress

N = Maximum compressive load resulting from the superposition of steady state compressive load plus the SRSS combination of loads generated by horizontal and vertical seismic and LOCA excitations, including secondary loading.

A = Nominal guide tube cross section area

δ = Eccentricity defined as the distance between the line of action of the axial load and the centerline axis deviation at mid length. The eccentricity is determined from the bowed geometry of the guide tube span. This parameter is calculated as the elastic deflection induced by the average span curvature obtained from the average bending moment M as:

$$\delta = \frac{M L^2}{8 EI} \quad \text{Equation 4-24}$$

E = Guide tube Young's modulus

I = Guide tube flexural inertia

v = Distance between guide tube centerline and outermost fiber

P_{crit} = Euler critical load for the span under analysis

K = Plastic shape factor of the tube cross section defined as:

$$K = \frac{16 OD.(OD^3 - ID^3)}{3\pi(OD^4 - ID^4)} \quad \text{Equation 4-25}$$

S_y = Material Yield Strength

The guide tube criteria introduced in this section have two substantial sources of conservatism:

- The yield stress limit used is for unirradiated material, in order to cover the entire service life of the fuel assembly. However, as discussed in Appendix A.1 the yield strength of the M5[®] alloy increases by [] due to irradiation.
- The criteria apply to each individual guide tube (treated as an isolated component) of the [] guide tubes in the fuel assembly. This is conservative since the load can be redistributed between guide tubes, which would provide additional protection.

4.3.3.2 Acceptance Criteria for the Upper and Lower Connection

The upper connection between the guide tube and top nozzle is located on the control rod insertion path, and is therefore limited to Level C service limits. In terms of implementation, the margins are assessed directly on the shear load of the weld nuggets connecting the upper quick disconnect to the guide tube, which are proved by test to be the limiting feature on the component (Figure 4-56). The test-based Level C load limit is 60% of the tested ultimate collapse load of the component, in accordance with NG-3224 of Subsection NG of the ASME Code Section III Division 1 (Reference 4).

Figure 4-56—Guide Tube to Top Nozzle Connection Joint

The lower connection (Figure 4-57) is mostly loaded in compression. The threaded connection between the cap screw and the guide tube is only lightly loaded when the fuel assembly rebounds during a LOCA event. So, the limiting feature of this connection is the guide tube to guide tube lower end fitting weld. The limits on this weld are in accordance with the ASME Code Level D condition. In accordance with Section III, Appendix F, the stress limits for full penetration welds are the minimum of $2.4 S_m$ or $0.7 S_u$ for primary membrane, and 1.5 times this amount for primary membrane plus bending or local membrane.

Figure 4-57—Guide Tube to Top Nozzle Connection Joint**4.3.3.3 Acceptance Criteria for the Guide Tube to Spacer Grid Connection**

As described in Section 2.1, the HTP spacer grids are connected to the guide tubes using [], while the HMP grids are connected by means of [] to the guide tube.

Both connection types are tested to ultimate collapse, and the results are statistically processed to produce the 95% confidence on true mean ultimate collapse load. The connections are limited by Level D limits in accordance with Appendix F of Section III of the ASME Code, article F-1440, which allows for a maximum load of 80% of the tested ultimate collapse load. The tested load is adjusted for temperature based on the ultimate tensile strength ratio.

4.3.3.4 Acceptance Criteria for the Top and Bottom Nozzle

The limits for the top and bottom nozzles are in accordance with the ASME Code Level D. The top nozzle limits are stress based, while the bottom nozzle limits, due to the complexity of the component are test load based.

In accordance with Appendix F of Section III of the ASME Code, article F-1331, for the top nozzle, the stress limits are the minimum of $2.4 S_m$ or $0.7 S_u$ for primary membrane, and 1.5 times this amount for primary membrane plus bending or local membrane.

For the bottom nozzle, the Level D limits are test load based, and conform to article F-1331.1, which allows the use of 100% of the tested collapse load (in accordance with the definition of Appendix II-1430). The collapse load was tested on a prototypical U.S. EPR Bottom Nozzle component.

4.3.3.5 Acceptance Criteria for Fuel Rod Cladding under Externally Applied Loads

The fuel rod cladding analysis scope of this technical report is limited to the mechanical loading effects of the postulated seismic and LOCA events. The normal operating stresses are superimposed on the stresses caused by the seismic and LOCA loading, and design margins are reported for this condition. The evaluation is performed for both irradiated and unirradiated condition, the normal operation stresses including: pressure stresses, ovality stresses, thermal stresses, flow induced vibration stresses, fuel rod - spacer grid stresses, growth stresses, and spring induced stresses. The seismic and LOCA operation fuel rod stresses include: lateral bundle deflection induced stresses, lateral impact induced stresses, and vertical loading induced stresses.

The stress limits for the M5[®] alloy are more stringent than the 90% of irradiated yield strength allowed by SRP 4.2 (Reference 2), and are defined in the approved topical report BAW-10227PA (Reference 10). The M5[®] alloy is limited to [

]. The design stress

5.0 INPUTS, FUEL ASSEMBLY RESPONSE, AND SPACER GRID IMPACTS FOR SEISMIC AND LOCA LATERAL LOADING

5.1 *U.S. EPR Fuel Assembly Lateral Seismic and LOCA Analysis Inputs*

The inputs to the core models discussed in Section 4.1.5 consist of displacement time histories at three locations:

1. Lower core plate.
2. Upper core plate.
3. Heavy reflector top.

The time histories derived from the reactor Internals models are discussed in Section 3.0.

The seismic SSE time histories cover the following nine governing soil cases: 1n2u, 1n5a, 2sn4u, 4u, 5a, BBLB, BBUB, BBBE, BBUB-CR. The results summarized in this section do not include soil case BBBE (best estimate), but this case is bounded by the BBLB (lower bound) and BBUB (upper bound) cases. Each soil case is modeled with an unirradiated and an irradiated fuel condition case, which results in a total of 18 sets of time histories. A set of time histories consists of two lateral directions and the three locations where displacements are imposed.

The LOCA time histories selected for this analysis consist of the two limiting cases:

- The 0% power condition case for the break on the safety injection system line on the hot leg (HELB-0HL).
- The 100% power condition case for the break on the safety injection system line on the cold leg (HELB-100CL).

Each seismic or LOCA time history was applied on five row models [

]. This results in a total of 900 analyses (five row models × 2 directions × 9 frequency sweep cases × 10 time histories).

5.2 U.S. EPR Fuel Assembly Lateral Seismic and LOCA Analysis – Results Summary

The results consist of grid impact loads and deflected fuel assembly configuration transient data. The fuel assembly deflection data are used as input for the component stress analysis, according to the methodology in Section 4.3. The results of the stress analysis are presented in Section 7.0. The grid impact loads are used to establish margins by direct comparison with the allowable crushing loads established in Section 4.1.4.1.7, Table 4-6.

The LOCA loads are square root of the sum of squares (SRSS) combined with the seismic loads. Since the LOCA loads in this application are one or two orders of magnitude lower than the SSE loads, only the SRSS combination is reported in this section.

The allowable crushing loads (unirradiated or irradiated condition) are assigned based on the discussion in Section 4.1.1.3, where the frequency sweep cases from

[

] With these specifications, the spacer grid impact load margins for all the frequency sweep cases are listed in Table 5-1. The limiting margins for the unirradiated and irradiated case for both types of spacer grids are listed in Table 5-2.

In accordance with SRP 4.2, the sensitivity of the spacer grid impact loads to input variations was assessed. The variation in input frequency is covered by the frequency sweep method. The 10% variation in input amplitude produces an upper bound 8.1% variation in spacer grid impact loads, and therefore no correction factors for margin calculation are necessary.

The maximum absolute nozzle bending moments are listed in Table 5-3. The nozzle bending moments are not limited by allowables, but serve as an indicator to facilitate the selection of the limiting cases for non-grid component stresses.

**Table 5-1—U.S. EPR Spacer Grid Impact Load Margins – All
Frequency Sweep Cases**



Table 5-2—U.S. EPR Spacer Grid Limiting Impact Load Margins



Table 5-3—U.S. EPR End Fitting Limiting Bending Moments



The unirradiated condition spacer grid allowable crushing load definition involves a small finite permanent deformation of the grid []. To assess the extent of the presence of permanent deformation [], the data were post-processed for an allowable crushing load limit based on []. The row models and seismic event where the permanent deformation exceeds the manufacturing tolerance are listed in Table 5-4.

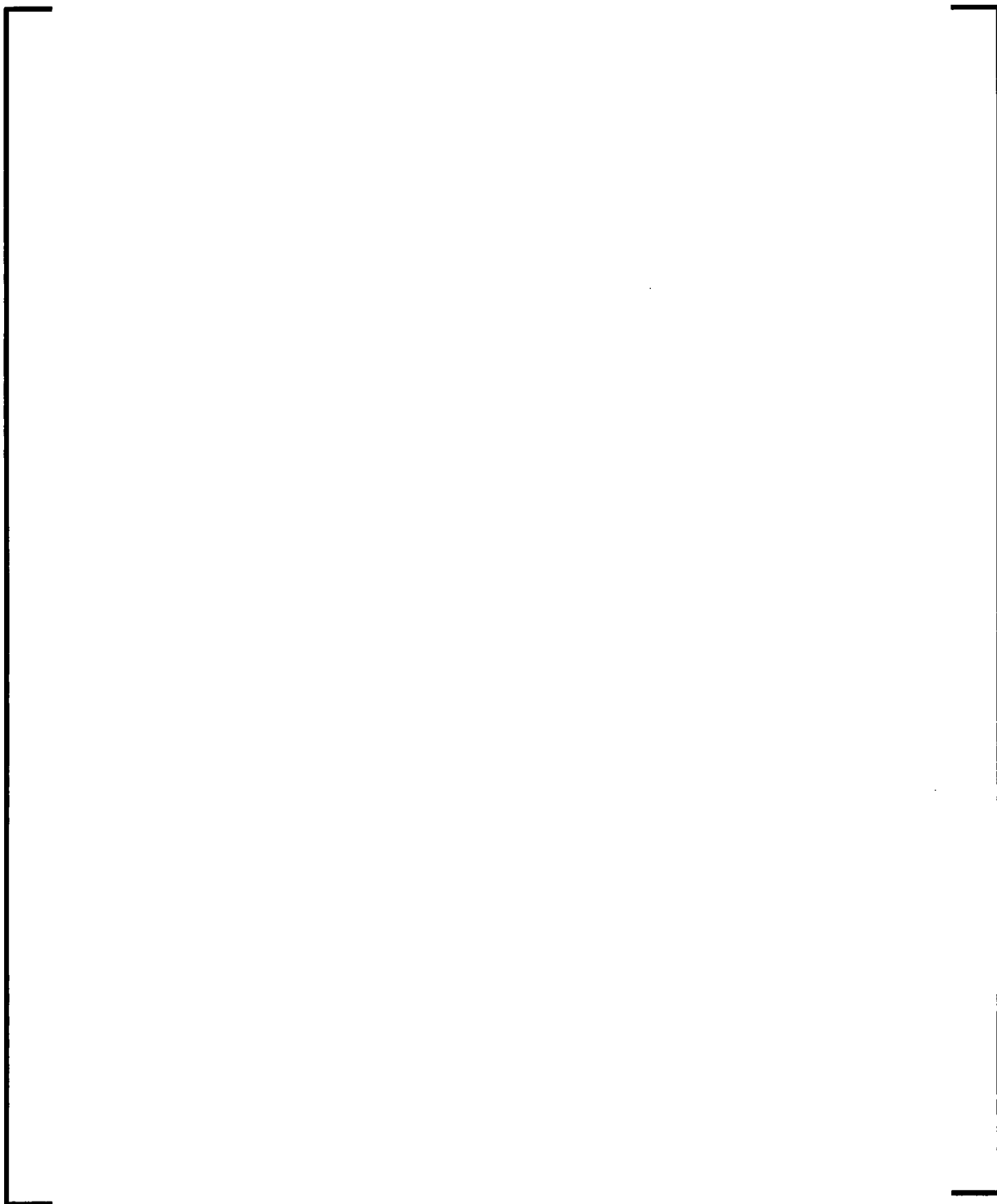
It is important to note that only [] for any combined SSE/LOCA event as noted in Figure 5-1. This is because the simulation results of the cases listed in Table 5-4 reveal that []. The subplots in Figure 5-1 represent independent scenarios that could lead to [].

This information will be used to support the thermo-hydraulic evaluation in
Section 4.1.4.1.4.1.

**Table 5-4—Frequency Sweep Cases with Permanent Deformation
over Manufacturing Tolerance**



**Figure 5-1—U.S. EPR Core Spacer Grid Locations
and LOCA Loads – Eight Independent Scenarios**



5.3 U.S. EPR Fuel Assembly Lateral Seismic and LOCA Analysis – Core Gap Sensitivity

This section presents the results of a gap sensitivity study which was discussed in Section 4.1.4.2 to address the accumulation of permanent deformation in a spacer grid before the allowable crushing load is reached. The linear visco-elastic grid element discussed in Section 4.1.4.2 is an adequate modeling approach for the spacer grid impact in the core row model, because it produces accurate values for peak impact load, deflection under load, and rebound velocity. However, the energy dissipation mechanism is different from the actual grid structure. In a real grid, the energy dissipation is structural in nature, and consists of local plastic deformation, and friction. In a linear visco-elastic element, the energy dissipation is viscous in nature. This difference does not alter the prediction of peak impact load, maximum impact deflection, or rebound velocity, but it alters the size of the core gaps. Whereas the linear visco-elastic element returns to zero displacement at the end of an impact, a real grid accumulates a small permanent deformation, which changes the core gap at that location. Due to the fact that that grid deformation is stable by virtue of selecting the limit load/deformation point on the stable side of the loading curve. This issue can be addressed as a core gap sensitivity issue. The approach is further bolstered by the fact that the threshold deformation is [

]

For this purpose, a study was conducted to gauge the sensitivity of the reported grid impact loads to variations in the core gaps. The study used a limiting time history, and the row model that produced the limiting grid impact loads. The assembly-to-heavy reflector gaps were changed independently from the assembly-to-assembly gaps. When changing the assembly-to-assembly gaps, all the gaps in the row were modified,

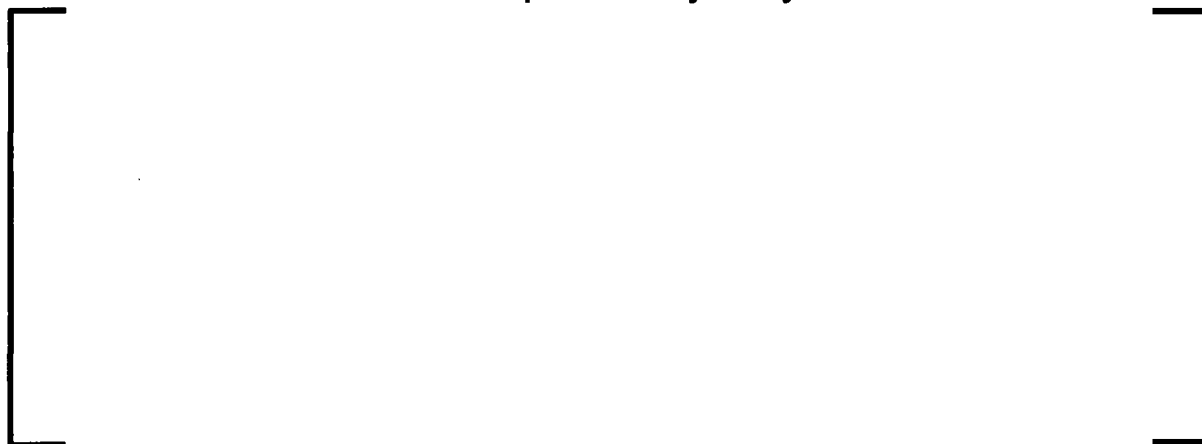
which produces an unrealistically conservative scenario. The study matrix is [

]

The results are presented in Table 5-5. The general observation is that [

].

Table 5-5—Gap Sensitivity Study Results



Due to the low sensitivity and decreasing grid impact load trend with increased core gaps, the linear visco-elastic grid model is adequate and conservative.

6.0 INPUTS, FUEL ASSEMBLY RESPONSE, AND COMPONENT LOADS FOR SEISMIC AND LOCA VERTICAL LOADING

6.1 *U.S. EPR Fuel Assembly Vertical Seismic and LOCA Analysis Inputs*

The inputs to the vertical seismic and LOCA analysis consist of displacement time histories applied to the core plates for seismic events, and hydraulic core load time histories for LOCAs. The hydraulic loads are separated in form loss loads, applied on the guide tube nodes, and friction loss loads applied on the fuel rod nodes.

Since the faulted loads must be analyzed in conjunction with the normal operating loads, the normal operation lift loads are applied in a ramped manner over the guide tube and fuel rod nodes for the first five seconds, and then allowed to reach a steady state during the next five seconds. All the accident simulations start at a time of 10 seconds.

For the seismic simulations, the normal operation lift loads are calculated from the initial loading obtained from the cold leg break time history, since this break occurs at 100% power. The hot leg break LOCA occurs at 0% power, so the normal operation lift loads are different for these cases.

The seismic and LOCA events analyzed are the same as those discussed in Section 5.1.

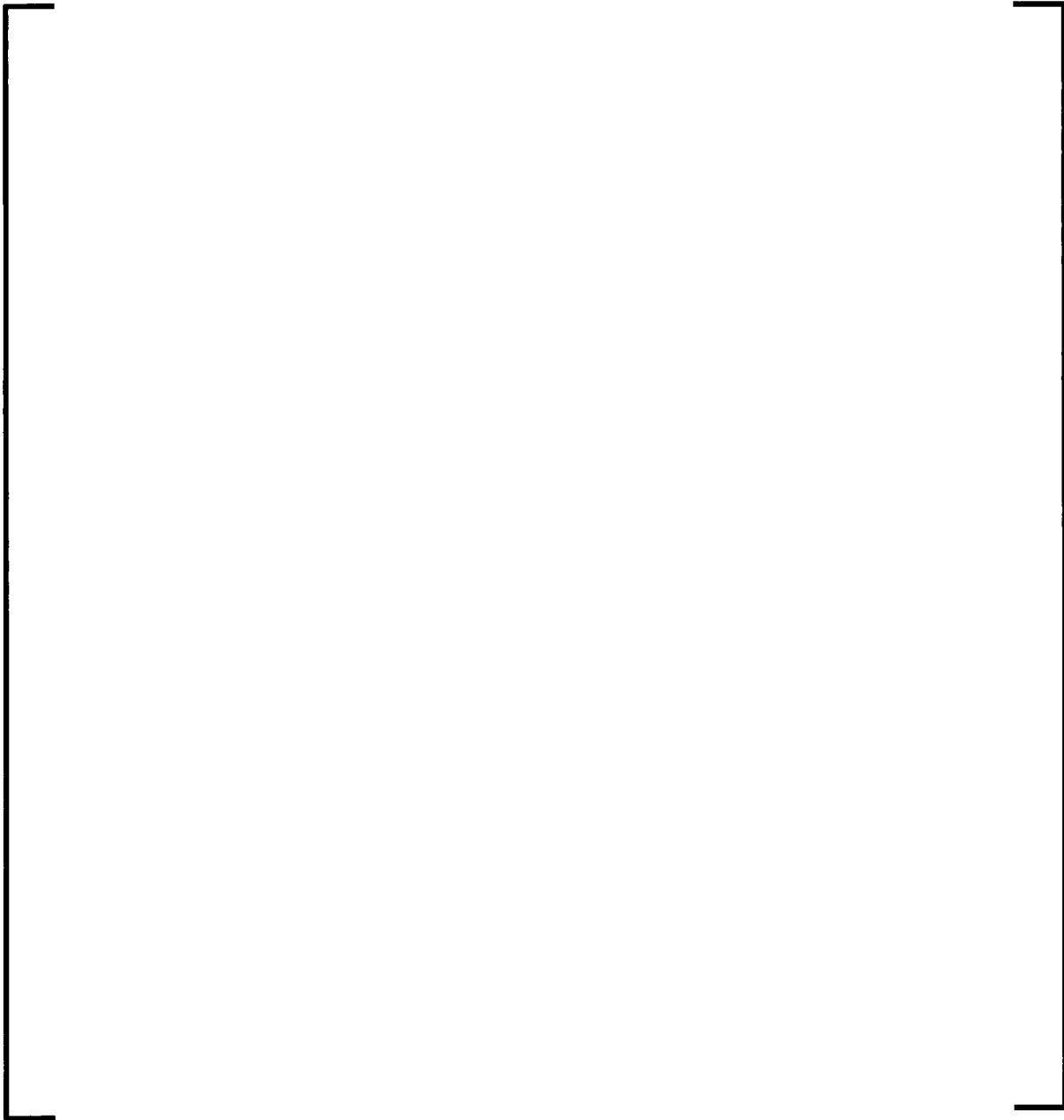
The core load per one fuel assembly in the two LOCA scenarios is plotted in Figure 6-1. In the actual analysis this load was distributed on the guide tube and fuel rod nodes.

The seismic displacement time histories at the core plates for both BOL and EOL cases are plotted in Figure 6-2. The differences between the UCP and LCP, or BOL and EOL are small, and are not visible on the displacement plots, but become apparent on the acceleration plots.

Figure 6-1—U.S. EPR Vertical LOCA Force Time Histories per FA



Figure 6-2—U.S. EPR Vertical SSE Displacement Time Histories



6.2 U.S. EPR Fuel Assembly Vertical Seismic and LOCA Analysis – Results Summary

The results of the analysis consist of component load time histories at all elevations, all guide tube and fuel rod spans, and all component connections.

The vertical analysis does not require the specialized capabilities needed for the lateral analysis. The analysis was therefore carried out using the general purpose finite element program ANSYS, version 11.0.

This section presents only a general summary of the results in the form of limiting component loads. More details will be discussed in Section 7.0. The overall limiting loads are shown in Table 6-1.

Table 6-1—Component Load Summary



7.0 COMPONENT STRESS ANALYSIS UNDER COMBINED LOADING

This section presents the results of the U.S. EPR fuel assembly non-grid component strength evaluation under seismic and LOCA loading. As mentioned in Section 4.3, the stress criteria are formulated in terms of primary membrane or membrane plus bending stresses, while the buckling criteria, and the welded joint load limits must be met for both primary and secondary loading combined. The vertical loading for both seismic and LOCA produces only primary stresses on the fuel assembly components. By contrast, the mechanical lateral loading produces both primary and secondary stresses. The secondary stresses are a result of the end nozzle rigid body rotation constraints applied on the rigid regions at the top and bottom nozzle locations, which essentially imposes a clamped boundary condition on the top and bottom nozzles. The method used to isolate the primary stresses is to run the analysis in two steps. The first step is analyzed with the imposed lateral displacements at all elevations, and with clamped end nozzles as boundary conditions. The results of this run represent primary and secondary stresses combined, and after combination with the normal operation and vertical loads, are used for buckling analysis. The imposed displacement analysis also produces reaction results at all imposed displacement DOFs. The second step consists of relaxing the clamped boundary condition at the end nozzles, and applying on the model the lateral reaction loads from step one. The results of this run consist of primary stresses only. These results are combined with normal operating and vertical loads, and are used in the calculation of the primary stresses to be compared with stress limits.

7.1 U.S. EPR Guide Tube Faulted Loading Analysis

The guide tubes are limited by both primary stress and buckling criteria. Given that the vertical loading model only produces primary stress results, for the purpose of buckling analysis, the vertical guide tube loads resulting from vertical seismic and LOCA loading are multiplied by a mal-distribution coefficient, which captures the non-uniform guide tube loading resulting from the possible bending of the bottom nozzle. The same

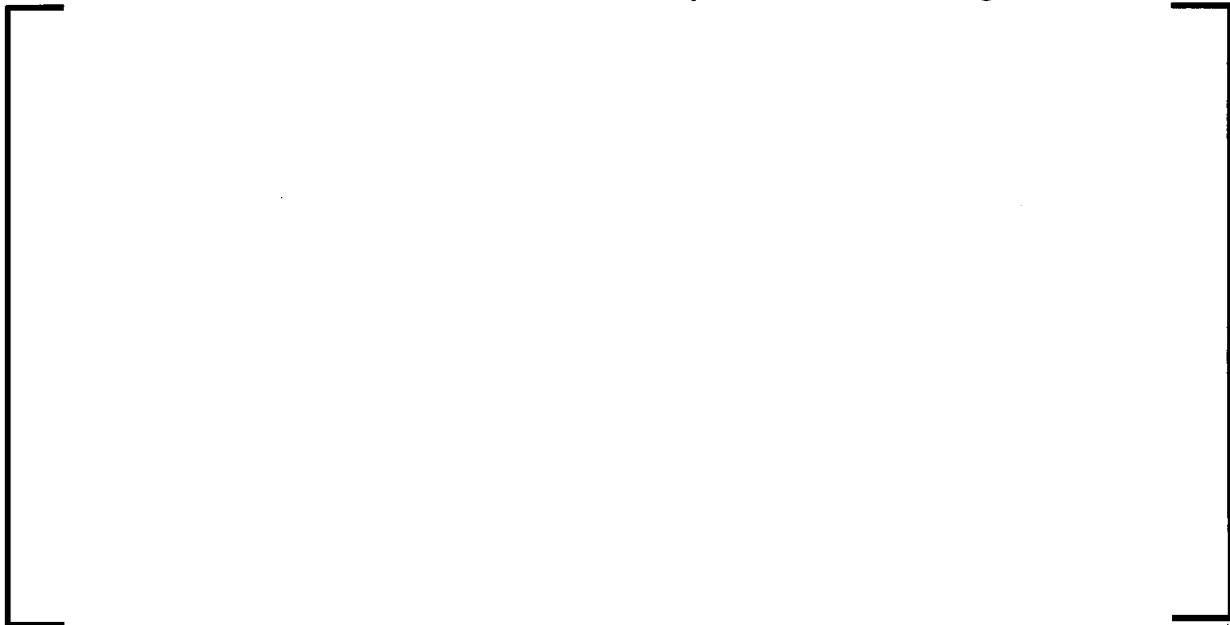
approach is used for the grid to guide tube welded connections. For the purpose of added conservatism in the case of the U.S. EPR, the mal-distribution coefficient is taken as [

] For stress analysis,

since the mal-distribution involves self-limiting secondary stress type loading, the average guide tube loads are used.

The guide tube stress results are summarized in Table 7-1. It must be pointed out that the margins are determined by the irradiated bundle condition cases. It is also important to note that the stress limits are based on unirradiated material properties, which brings substantial conservatism to the reported margins.

Table 7-1—Guide Tube Faulted Operation Stress Margins



The buckling analysis of the guide tubes involves, as a first step the calculation of the Euler critical load for every guide tube span. This has been performed using the [

] Once the Euler critical load is determined, a calculation is made of the maximum span axial load, and the potential lateral deflection at mid-span resulting from the loads applied to the guide tube by the spacer grids or end nozzles. Applying the secant formula (Equation 4-23), the maximum outer-fiber stress is calculated and compared to the yield strength, multiplied by the plastic shape factor. The minimum margin, using unirradiated material strength data is []

7.2 U.S. EPR Guide Tube Upper and Lower Connection Faulted Loading Analysis

The upper and lower connection design criteria are described in Section 4.3.3.2. The upper connection is restricted to Level C service limits because it is located on the control rod insertion path. The limits are based on tested ultimate collapse load scaled by a coefficient of 60% in accordance with NG-3224 (Reference 4). Since the tests were performed at operating temperature, no temperature correction is necessary. The margin is [], and, as in the case of the guide tubes is based on unirradiated material strength data.

The lower connection dominant loading is in compression, during impacts of the bottom nozzle on the reactor core plate. Therefore, the cap screw is not significantly loaded, and the limiting feature is the guide tube to guide tube lower end fitting weld. The limits on this weld are stress based, in accordance with the ASME Code Level D condition. In accordance with Section III Appendix F, the stress limits for full penetration welds are

the minimum of $2.4 S_m$ or $0.7 S_u$ for primary membrane. The margin is [], and is based on unirradiated material data.

7.3 U.S. EPR Guide Tube to Spacer Grid Connection Faulted Loading Analysis

The spacer grid to guide tube connection loads consist of axial shear. The evaluation of the limiting loads shows that the intermediate spacer grid (HTP grid) loads are [

] The weld strength was tested for [

] This strength value was then scaled by the ratio of ultimate tensile strength at operating versus ambient temperature, and scaled by a factor of 80%, in accordance with article F-1440 in Appendix F in Section III of the ASME Code, consistent to the Level D service limits. The allowable strength was [

] In addition to the conservative statistical processing of the strength data, this margin calculation also includes a substantial level of conservatism due to the use of the mal-distribution coefficient, and the fact that the combined axial load on the guide tube exceeds the grid slip load, but this effect is ignored in the analysis.

7.4 U.S. EPR Top and Bottom Nozzle Faulted Loading Analysis

The top nozzle was analyzed using an FEM using the commercial finite element software, ANSYS. The analysis is linear-static. The criteria are stress-based, and are

consistent to the Level D service limits (Appendix F, Section III (Reference 4)). The results and the margins are reported in Table 7-2.

Table 7-2—U.S. EPR Top Nozzle Faulted Stress Analysis

Because of the intricate geometry and brazed features, which make an analytical approach difficult, the bottom nozzle was qualified for service based on tested collapse load. The service limits are consistent with Level D (Appendix F, Section III, Reference 4). The bottom nozzle tests consist of applying an axial compression on the guide tube embossments, while the nozzle is seated on a flat surface. These tests are conducted in accordance with the guidance in Appendix II-1430 in Section III of the ASME Code. The collapse tests differ from the ultimate collapse tests because in the former case, the component does not really collapse, but the loading curve veers off of the linear path and intersects a line with a slope that is double that of the elastic line. When this point is reached, the component is deemed to be on the verge of losing the ability to control displacements under the imposed loading. This is different from the ultimate collapse load, where the component is tested to the point that the tangent to the loading curve has a zero slope (breaking point). Because of this difference, the collapse load can be credited 100% toward meeting the Level D criteria, in accordance with F-1331.1 (Appendix F, Section III, Reference 4). The tested collapse load was scaled by the ratio of yield strength at operating temperature versus ambient temperature, in accordance with the provisions in Appendix II-1430 in Section III of Reference 4. The resulting margin is []

7.5 U.S. EPR Fuel Rod Faulted Loading Analysis

For the purposes of this technical report, the fuel rod cladding analysis focuses on the mechanical loading effects of the postulated seismic and LOCA events. The normal operating stresses are superimposed on the stresses caused by the seismic and LOCA loading, and design margins are reported for this condition.

The faulted stresses are superimposed on the normal operating stresses, for both irradiated and unirradiated conditions. The normal operating stresses include:

- Pressure stresses,
- Ovality stresses,
- Thermal stresses,
- FIV stresses,
- Fuel rod to spacer grid contact stresses,
- Growth stresses,
- Plenum spring induced stresses.

The seismic and LOCA operation fuel rod stresses include:

- Lateral bundle deflection induced stresses,
- Lateral impact induced stresses, and
- Vertical loading induced stresses.

The lateral bundle deflection stresses are obtained from the non-linear FEM, as described in Section 4.3.2, and represent the two most demanding load cases for the unirradiated and irradiated condition, respectively. The non-linear model stresses are extrapolated using a 2D planar extrapolation to capture the limiting fuel rods in the four corners of the bundle.

The lateral impact induced stresses capture the bending response of the bundle spans following a spacer grid impact, which can excite additional bending of the fuel rod cladding within a spacer grid span. The impact energy stored in the internal grid spring element during the impact (Figure 4-42) is assumed to transfer completely into bending strain energy of the adjacent spans. By equating this energy to the bending strain energy of a fuel rod span with fixed-fixed boundary conditions, a maximum bending moment is calculated, and from it a maximum bending fuel rod cladding stress.

The vertical fuel rod cladding stresses are obtained directly from the vertical (as an average over the [] individual fuel rods) by post-processing the response generated by the seismic and LOCA loads.

Using the M5[®] fuel rod stress limits discussed in Section 4.3.3.5, the fuel cladding stress margins are summarized in Table 7-3.

Table 7-3—U.S. EPR Fuel Rod Cladding Faulted Stresses



The buckling evaluation was performed similarly to the one used for guide tube analysis. The corner rods bundle deflection induced compressive loads are SRSS combined with those generated by the vertical excitations. The bundle deflection induced eccentricities are combined with those generated by the impact induced fuel rod deflections using an SRSS combination. Since in the irradiated condition the spacer grid cells are relaxed, the rotational stiffness at the fuel rod to grid interface changes

from the unirradiated condition, and therefore two sets of Euler critical buckling loads were calculated. The first set is relative to unirradiated conditions, and the second one relative to irradiated conditions. The conclusion of the assessment is that the fuel rod cladding buckling margin []

7.6 U.S. EPR Fuel Assembly Component Load Core Gap Sensitivity

As mentioned in Section 4.1.4.2, the effect of the unirradiated grid permanent deformation on grid impact loads and on fuel assembly component stresses can be addressed through a sensitivity study, in which the core gaps can be changed and the analysis repeated to produce a percent change of the results. The grid impact load sensitivity was addressed in Section 5-7, together with the justification for this approach. This section discusses the component stress sensitivity to changes in core gaps.

The study described in Section 5-7 also produces the changes in top and bottom nozzle reaction bending moments. In Reference 8 it was shown that the end nozzle bending moments correlate linearly with the guide tube stresses. Therefore, for comparison purposes, the percent change in the end nozzle reaction bending moment translates into the percent change in guide tube stress.

The study uses the two limiting time histories (one for unirradiated and one for the irradiated condition) applied to the row models producing the highest end nozzle moments. The assembly-to-heavy reflector gaps were changed independently from the assembly-to-assembly gaps. When changing the assembly-to-assembly gaps, all the gaps in the row were modified, which produces an unrealistically conservative scenario.

The study matrix is []

]

The results for the unirradiated limiting case [] are presented in Table 7-4 and Table 7-5, while the results for the irradiated limiting case are presented in Table 7-6 and Table 7-7. The normalized comparison indicates that, in all cases, the variation in the end nozzle bending moments is contained in a range of [] of the nominal case, which is small, especially considering the very large change imposed on the core gaps. The actually predicted grid permanent deformations addressed in Section 5.2 are substantially lower. With the exception of []

] Therefore, a more representative measure of the sensitivity to core gaps is offered by the data coming from the two center rows and columns in each table. This indicates that the sensitivity of the end nozzle bending moments; and, by extension, of the guide tube stresses is in the range of [], which would have a negligible impact on the reported margin on guide tube stresses.

Table 7-4—Unirradiated Normalized SSE Top Nozzle Moments

--	--

Table 7-5—Unirradiated Normalized SSE Bottom Nozzle Moments

--	--

Table 7-6—Irradiated Normalized SSE Top Nozzle Moments

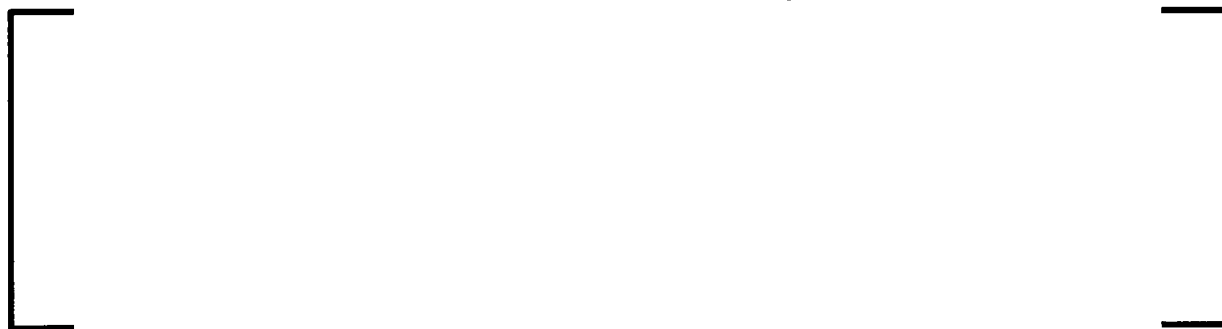
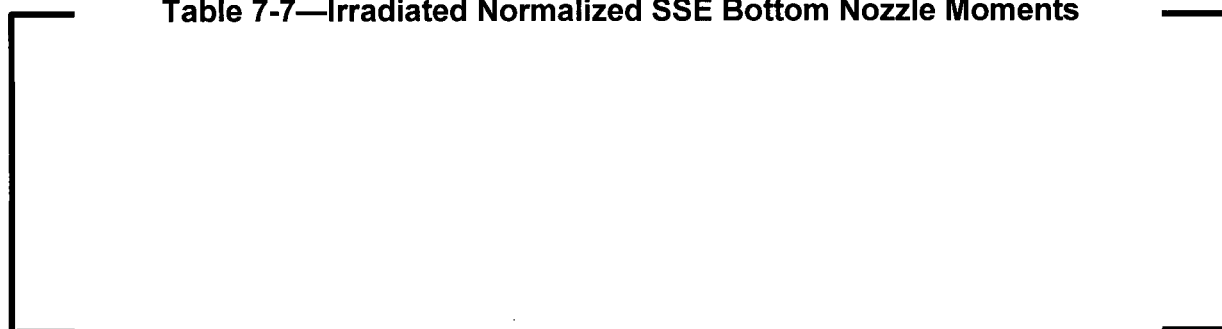


Table 7-7—Irradiated Normalized SSE Bottom Nozzle Moments



8.0 REFERENCES

1. AREVA NP, ANP-10285P Rev. 0 – “U.S. EPR Fuel Assembly Mechanical Design Topical Report,” October 2007.
2. BAW-10133PA, “Mark-C Fuel Assembly LOCA-Seismic Analyses,” Revision 1 and Addenda 1 and 2, October 2000.
3. Nuclear Regulatory Commission, Regulatory Guide 1.92, “Combining Modal Responses and Spatial Components in Seismic Response Analysis,” Revision 3, ADAMS - Accession Number ML053250475.
4. American Society of Mechanical Engineers, Boiler and Pressure Vessel Code, Section III, “Rules for Construction of Nuclear Power Plant Components,” 2009 Revision with Addenda, New York.
5. U.S. EPR Final Safety Analysis Report, Revision 4 - Interim.
6. Meirovitch, L., “Principles and Techniques of Vibrations,” Prentice Hall, 1997.
7. AREVA NP, ANP-10285Q10P, Response to Seventh Request for Additional Information – ANP-10285P “U.S. EPR Fuel Assembly Mechanical Design Topical Report” RAIs Numbered 64 through 71, August 2012.
8. AREVA NP, ANP-10285Q9P, Response to Sixth Request for Additional Information – ANP-10285P “U.S. EPR Fuel Assembly Mechanical Design Topical Report” RAIs Numbered 53 through 59, July 2011.
9. U.S. Nuclear Regulatory Commission, Regulatory Guide 1.61, “Damping Values for Seismic Design of Nuclear Power Plants”, Revision 1, ADAMS - Accession Number ML070260029.
10. Babcock and Wilcox, BAW-10227P-A, “Evaluation of Advanced Cladding and Structural Material (M5) in PWR Reactor Fuel,” June 2003.
11. BAW-10172P-A, “Mark-BW Mechanical Design Report,” December 1989.

12. R. L. Grubb, "Review of LWR Fuel System Mechanical Response with Recommendations for Component Acceptance Criteria," Idaho National Engineering Laboratory, NUREG/CR-1018, September 1979.
13. U.S. Nuclear Regulatory Commission, Seventh Request for Additional Information Regarding ANP-10285P, "Fuel Assembly Mechanical Design Topical Report" (TAC NO. RN1224), May 2011, Available in the NRC ADAMS - Accession Number ML111230049.
14. E. Viallet, G. Bolsee, B. Ladouceur, T. Goubin, J. Rigauddau, "Validation of PWR Core Seismic Models with Shaking Table Tests on Interacting Scale 1 Fuel Assemblies," Presented at the 17th International Conference on Structural Mechanics in Reactor Technology (SMiRT 17), Prague, August 2003.

Appendix A: U.S. EPR Spacer Grid Characterization – Detailed Information

This appendix contains detailed material on the topic of spacer grid characterization and allowable crushing load definition. It is the basis for the conclusions and for the less detailed discussion in the main document, in Section 4.1.4.

A.1 Spacer Grid Allowable Crushing Load – Effects of In-Reactor Operation

The SRP 4.2 bases the grid strength definition on the assumption that the BOL grid strength is limiting, and that the effects of material irradiation hardening and of the more difficult to predict grid cell deformation at end of life cancel each other.

Recently the NRC issued Information Notice 2012-09 (Reference 1), in which the base assumption of SRP 4.2 of the BOL strength being limiting is challenged. This section is a brief review of the effects of in-reactor operation and the industry developments aimed at addressing this aspect of grid operation.

First, it must be mentioned that, for normal operation, the effects of in-reactor operation are addressed in the SRP 4.2 in Section II:

“Oxidation, hydriding, and the buildup of corrosion products (crud) should be limited, with a limit specified for each fuel system component. These limits should be established based on mechanical testing to demonstrate that each component maintains acceptable strength and ductility. The safety analysis report should discuss allowable oxidation, hydriding, and crud levels and demonstrate their acceptability.”

The primary concern of SRP 4.2, Section II is the loss of component load capability by degradation of the wall thickness via oxidation, by decreased yield strength because of increased wall temperature (which is the result of degraded heat transfer), and by reduction in the load redistribution capability of the material via decreased ductility produced by hydrogen pickup. However, for spacer grid accident analysis under externally applied loads, there is no provision requiring limits on these factors. The

made of Zr-4. The spacer grid hydrogen uptake was also measured for a number of grids at [

]. Both the M5[®] and Zr-4 hydrogen pickup limits are identified on Figure A-1 and Figure A-2.

Figure A-1—Ultimate Elongation for Zirconium Alloy Guide Tube Specimens



Strength:

The material strength, as measured by the yield strength, displays very weak effects with respect to the hydrogen concentration in both unirradiated and irradiated condition. In the irradiated condition, the yield strength increases very slightly with increased

hydrogen concentration over the range of 200 to 2000 ppm (Figure A-2). The effect is clearly second order, and by comparison with the effect of irradiation on yield strength, it can be set aside for the purposes of spacer grid mechanical strength, especially for M5[®] grids, because of the very low hydrogen uptake of this material.

Figure A-2—Tensile Strength for Irradiated and Unirradiated Zirconium Alloy Guide Tube Specimens



Conclusion:

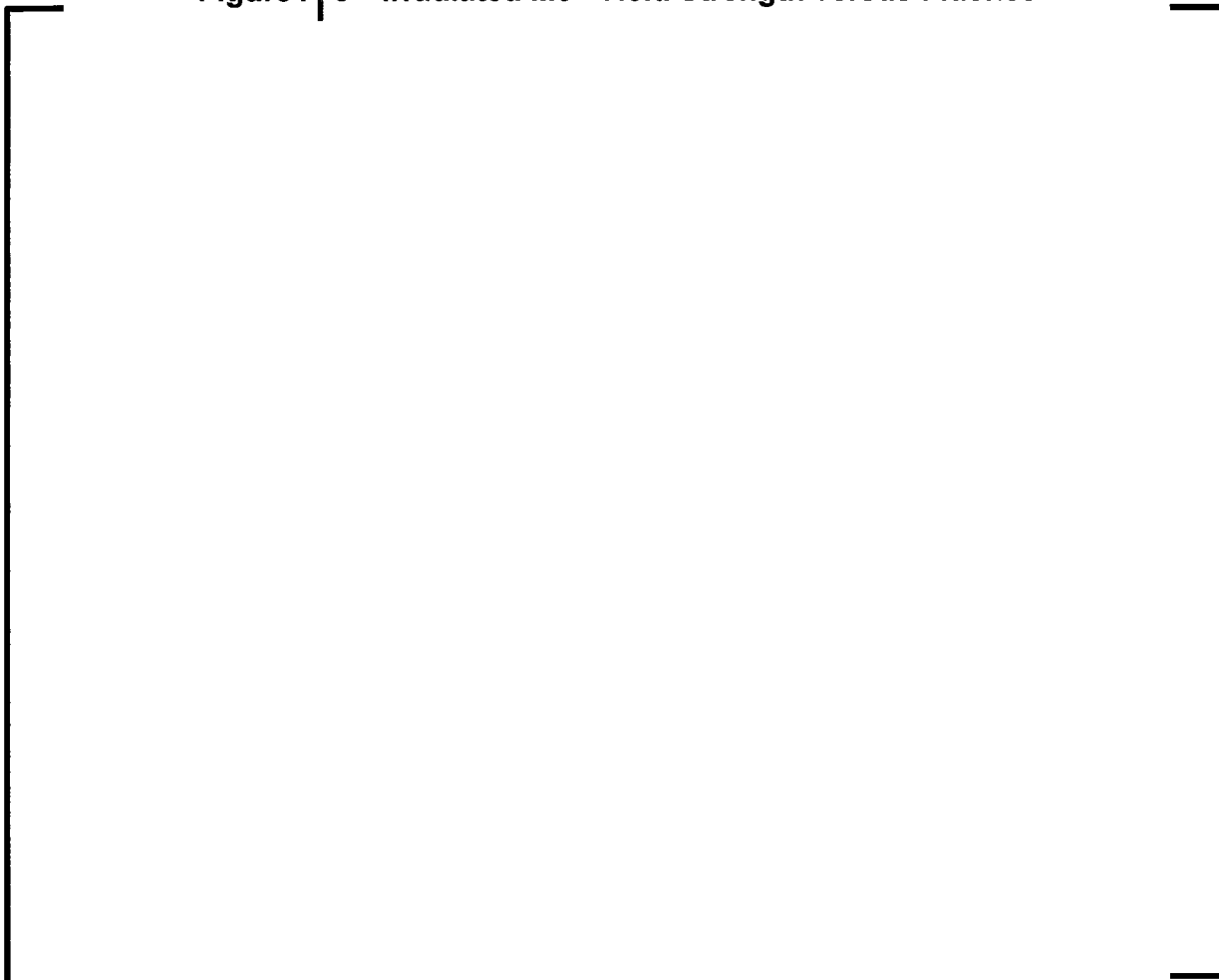
As a general conclusion, the hydrogen uptake, especially over the range of [], which is representative for M5[®] spacer grids, has a negligible impact on both the ductility and yield strength of this material. Even for Zr-4 grids, the effect on

both yield strength and ductility in the irradiated condition is secondary due to the relatively low hydrogen uptake on structural components.

Irradiation Hardening:

As already indicated in Figure A-2, the general trend for all zirconium alloys is that yield strength increases substantially with irradiation exposure at levels compatible with those encountered during the service life of a fuel assembly component. Figure A-3 presents the evolution of the yield strength of M5[®] with fluence. It can be seen that the irradiated yield strength is [] higher than the unirradiated yield strength at operating temperatures. Also, it is clear that the entire irradiation hardening process reaches the asymptotic value in []

].

Figure A-3—Irradiated M5[®] Yield Strength versus Fluence**Irradiation Induced Loss of Ductility:**

The general trend for Zirconium alloys is that ductility, as measured by the total elongation decreases with increased fluence. For M5[®] in particular, the total elongation at operating temperature decreases from [

] as shown in Figure A-4. The ductility loss is essentially complete in

[

] This point will be discussed again

in the context of irradiated grid testing.

Figure A-4—Total Elongation versus Fluence for M5[®]



Irradiation Induced Stress Relaxation:

Zirconium alloys lose almost all prestress due to irradiation relaxation over a fluence range commensurate with the in-reactor service life of a fuel assembly. This material

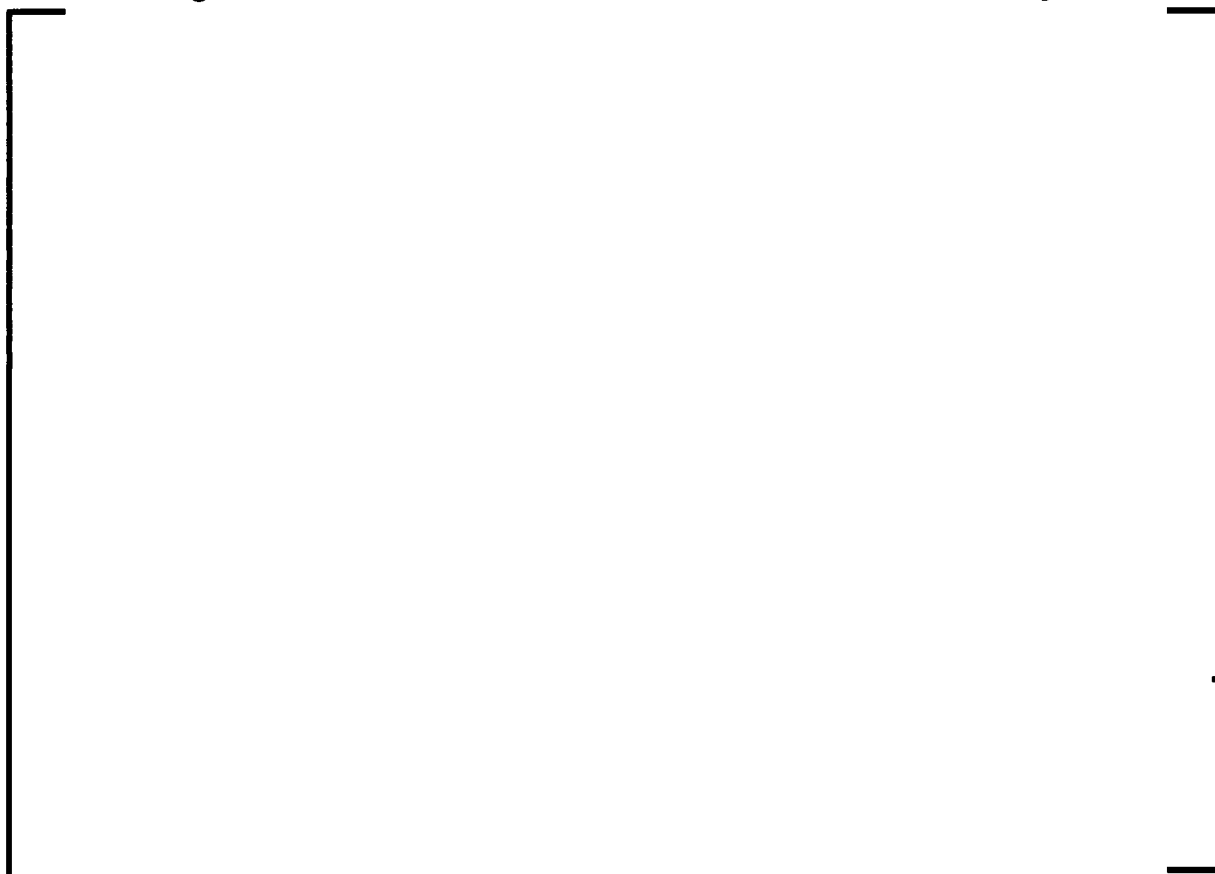
characteristic is [

]. The effect on

grid strength is a result of the relaxation of the grid cell springs, which reduces the lateral load support on the fuel rods, and produces a degradation of the critical buckling load of the grid. Figure A-5 presents a lower bound curve for the stress ratio versus fluence, for a large number of zirconium alloy specimens irradiated in an experimental reactor. The stress ratio of the irradiated versus initial stress are plotted versus fluence, including the Zr1Nb data points. For the purposes of this discussion we will use the lower bound curve. The entire AREVA M5® product [

] specimens.

Figure A-5—Irradiation Stress Relaxation for Zirconium Alloys



A.1.2 Irradiated Grid Testing

This section discusses the results of an irradiated grid test program AREVA conducted a decade ago.

In 2003, AREVA submitted the "Closure of Interim Report 02-002" (Reference 2) to the NRC. In this communication, the conclusions of strength testing on full spacer grids following actual reactor operation up to [] were made public. The main point was that grid strength in irradiated condition was less than the new production grid strength.

The tests were conducted []

]

A conclusion can be obtained by plotting the grid [

], which

is consistent with the data in Figure A-5. The interdependence between grid [

].

[

].

Figure A-6—Grid Buckling Load versus Cladding Insertion Force

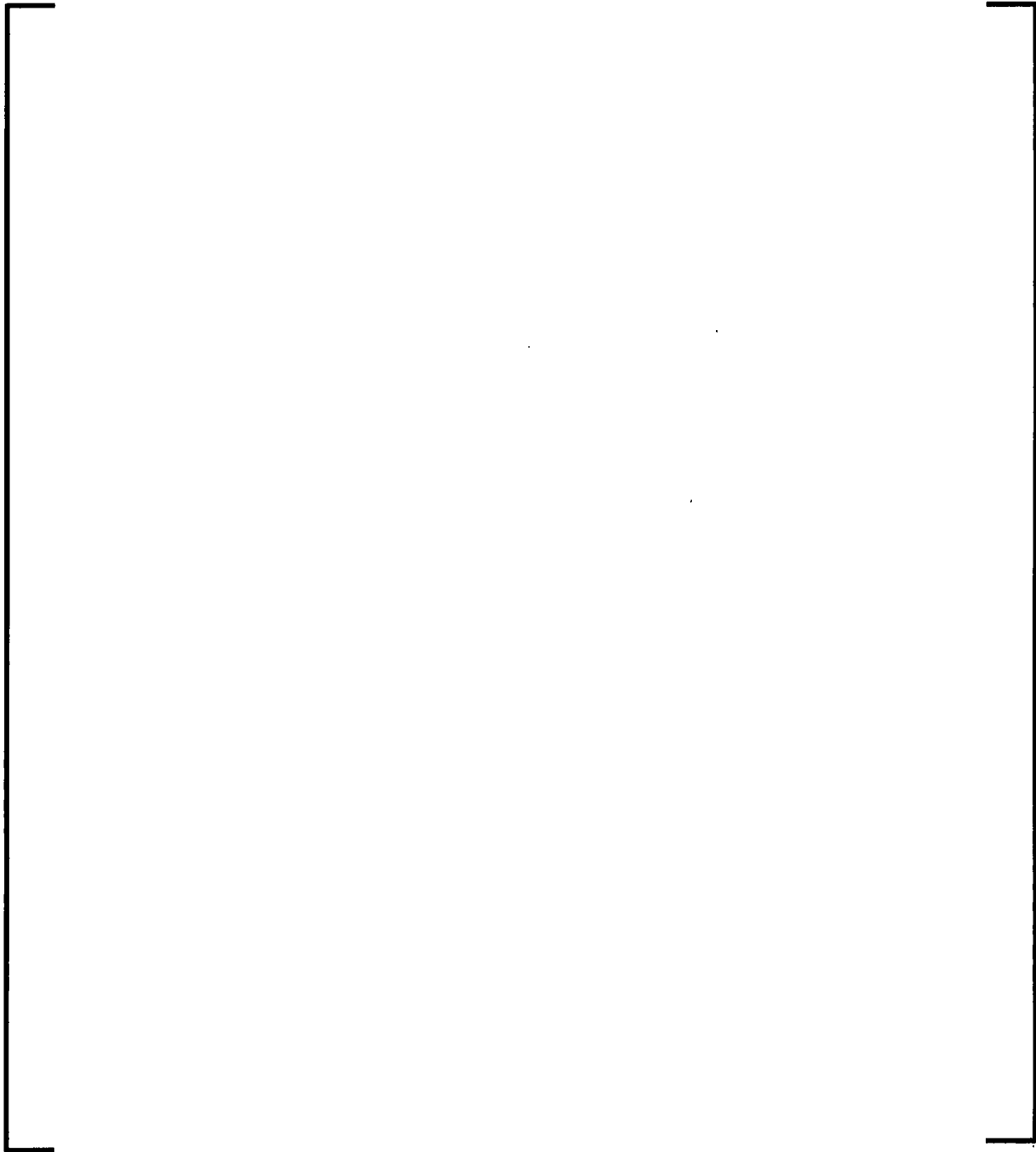
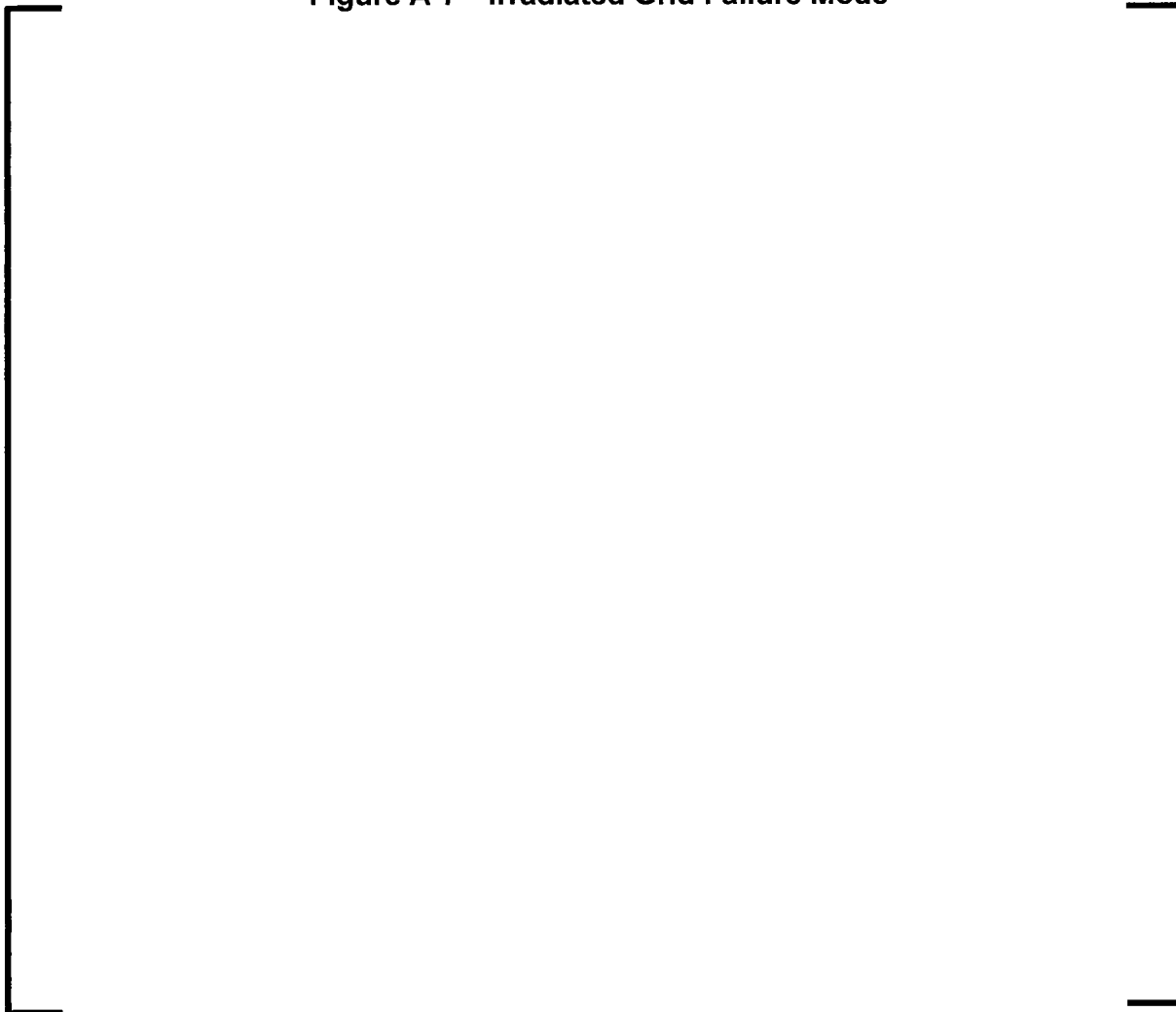


Figure A-7—Irradiated Grid Failure Mode



A second order effect was observed in that the [

]

The variation of the buckling load with [

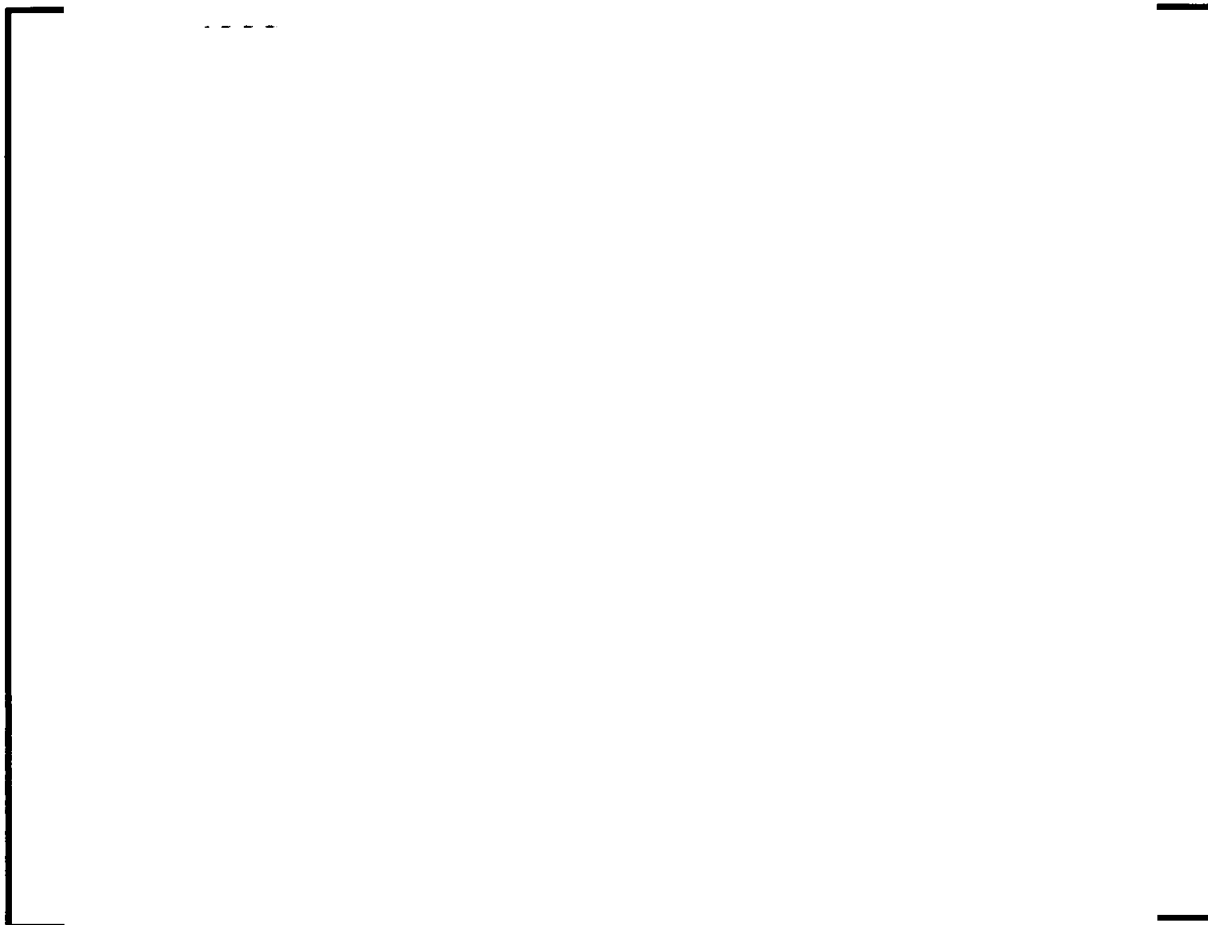
].

Figure A-8—Variation of Grid Buckling Load with Axial Grid Position



The explanation is partially attributed to the [

]

Figure A-9—Grid Buckling Load versus Oxide Layer Thickness

A.1.3 Summary of In-Reactor Operation Effects on Grid Strength

While the effects of in-reactor operation on zirconium alloy mechanical material properties have been the object of extensive investigations, the compounded effect of these factors on the EOL grid strength and mechanical behavior is a relatively recent concern in the industry. Presently, within AREVA's knowledge, the only publicly communicated strength testing of spacer grids that were actually operated in a power reactor are the AREVA tests discussed in this report and conveyed to the NRC in Reference 2.

The conclusion that can be formulated based on the available test data on irradiated materials and on irradiated spacer grids is that the multi-faceted effects of in-reactor operation are clearly distinguishable, with some of these effects being of second order importance. These effects are:

- [

]

These considerations are integrated into the spacer grid irradiated condition allowable crushing load and test protocol, which are discussed in the main body of this document.

A.2 AREVA Spacer Grid Testing Methodology

This methodology was established in Addendum 1 of BAW-10133PA (Reference 2).

The spacer grids are tested on a dynamic test bench. The spacer grid is placed inside a furnace which is supported by a rigid frame. A carriage of a certain mass is accelerated (by means of a mass and pulley system) in linear motion against the spacer grid. A schematic of the test bench showing all the major components is shown in Figure A-10, and the actual test bench arrangement is shown in Figure A-11. The test consists of a sequence of impacts of increasing kinetic energy (starting at [

]).

Figure A-10—Spacer Grid Impact Testing Schematic

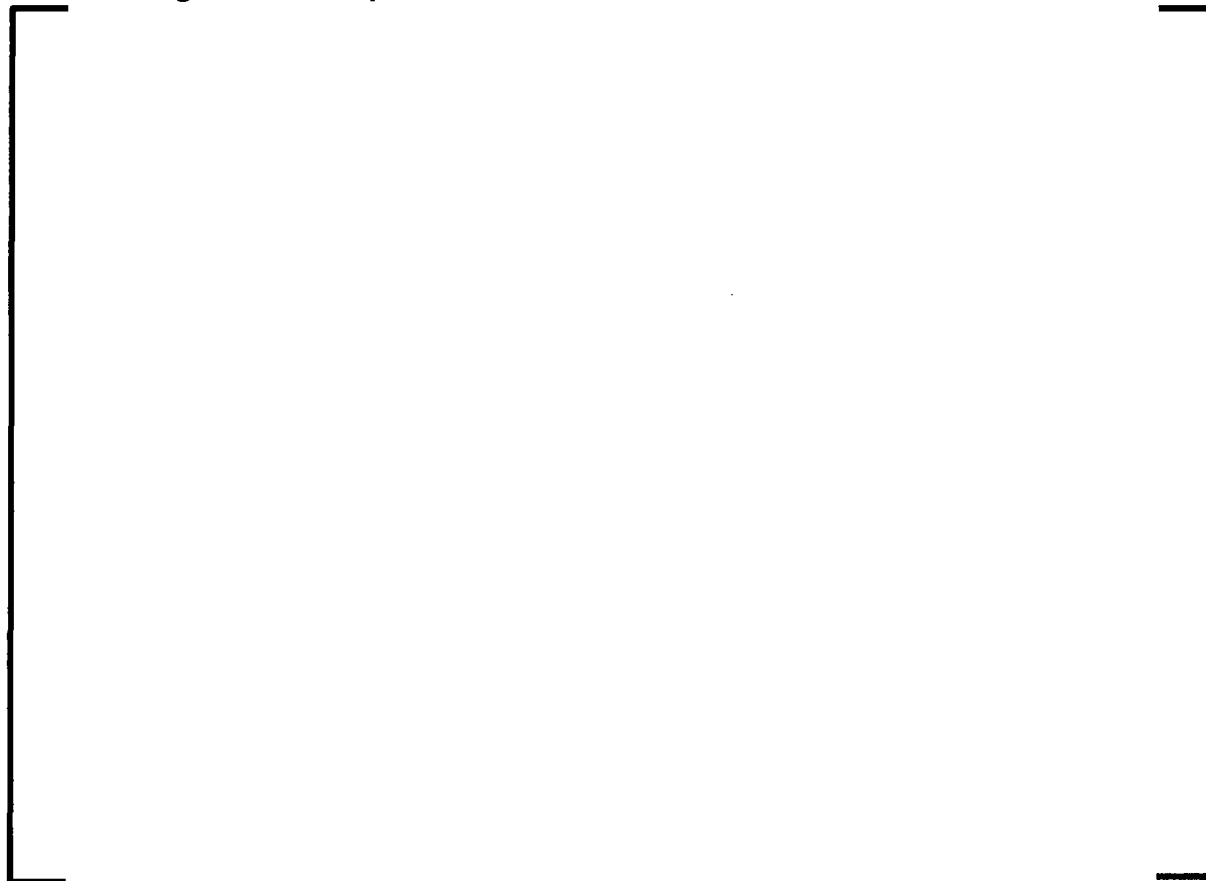


Figure A-11—Spacer Grid Testing Bench

Before the test, the grid envelope is measured and the component is fully inspected (Figure A-12). For the U.S. EPR spacer grids, the coordinates of the guide tubes were also recorded before and after the test. Also, each spacer grid undergoes an insertion load measurement before the test. The grid is supported on a horizontal fixture (Figure A-13), and a set of fuel rod cladding segments is pushed through, while the load is recorded. This measurement is a check on the grid condition – unirradiated or simulated irradiated.

Figure A-12—Spacer Grid Pre-Test Inspection



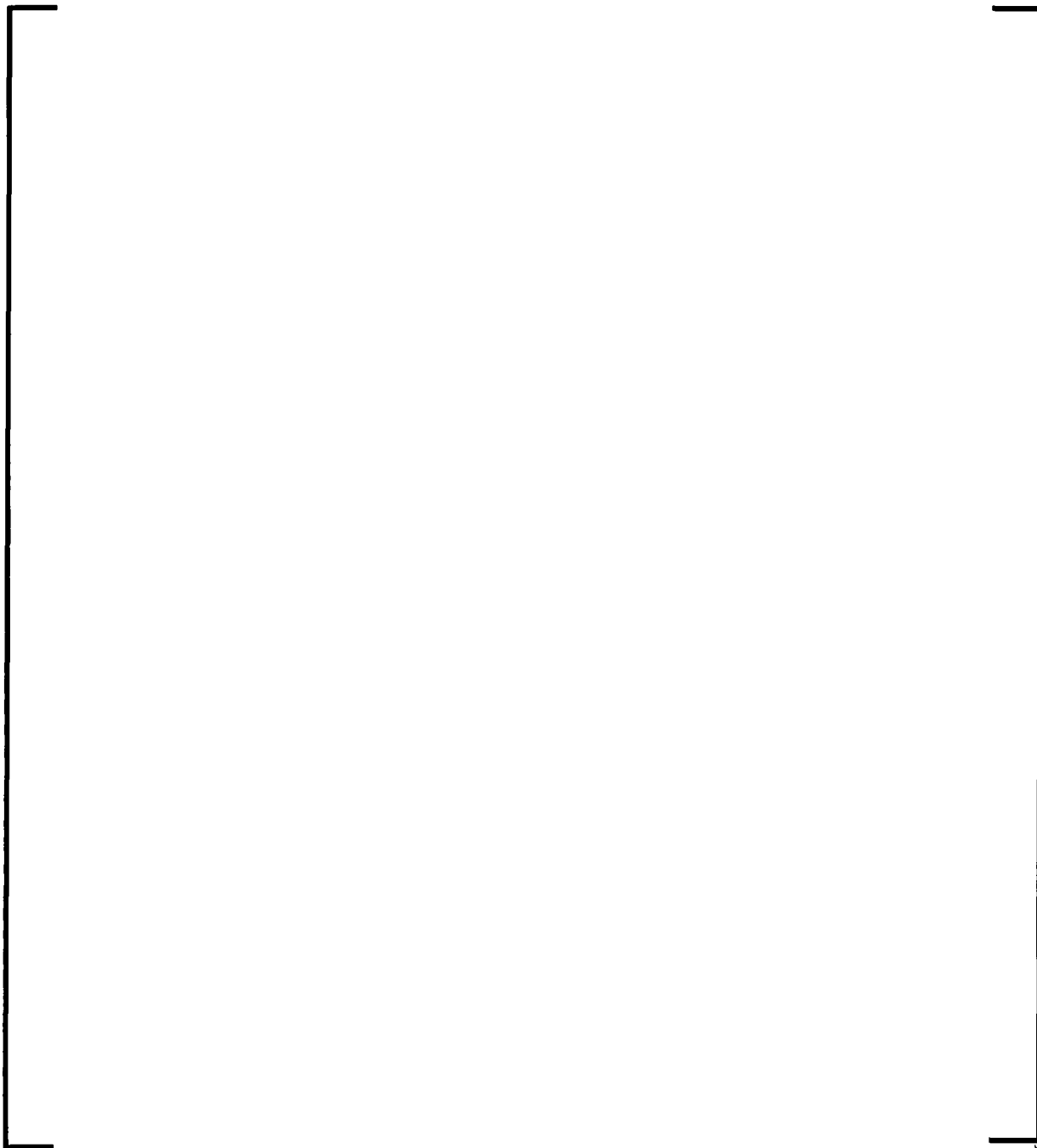
Figure A-13—Spacer Grid Pre-Test Insertion Load Measurement

At every impact, the control rod insertability is checked by means of inserting a rigid gauge holding the outer pattern of control rods. This check is very conservative, since it discounts the inherent flexibility of the control rods, which makes the control rod insertion easier.

Figure A-14—Spacer Grid Control Rod Test Gauge

The impacts are escalated until the buckling limit of the spacer grid is reached. The buckled configuration is characterized by a few rows (usually 2 or 3) which lose their "square" pattern, the cells displaying a "diamond" shape. An example of a buckled spacer grid is shown in Figure A-15.

Figure A-15—Example of a Buckled U.S. EPR HTP Spacer Grid



A detailed photo of the racked area is shown in Figure A-16.

Figure A-16—Detail of a Buckled U.S. EPR HTP Spacer Grid**A.3 U.S. EPR HTP Spacer Grid - Uniform Deformation Characterization**

This section discusses the details regarding the uniform character of deformation at the spacer grid allowable load in the unirradiated condition, in support of the general conclusions listed in Section 4.1.4.1.4.1.

Tests of two of the [] HTP spacer grids (serial numbers B30121 and B30122) used for the allowable crush load testing were stopped after [] permanent deformation. The grids were geometrically inspected to establish:

- General envelope before and after the test.
- Guide tube pattern before and after the test.
- Fuel rod (all fuel rod cells) pitch before and after the test.

Upon visual inspection, the deformed lattice pattern is indistinguishable from the undeformed state, as it can be seen in Figure A-17 and Figure A-18.

The spacer grid envelope measurements are presented in Figure A-19 and Figure A-20. The envelope measurements were performed using a 3D measurement machine that measured the position of 16 locations on each grid face. The deformation in the <x> and <y> direction are scaled by a factor of 10 for better visualization. The <y> direction is aligned with the impact direction. From the envelope inspections, it is clear that nearly all of the deformation is in the impact direction. Except at the corners of the grids, there is no deformation in the direction perpendicular to the impact direction.

Figure A-17—U.S. EPR Spacer Grid B30121 – Uniform Deformation at Allowable Deformation Limit

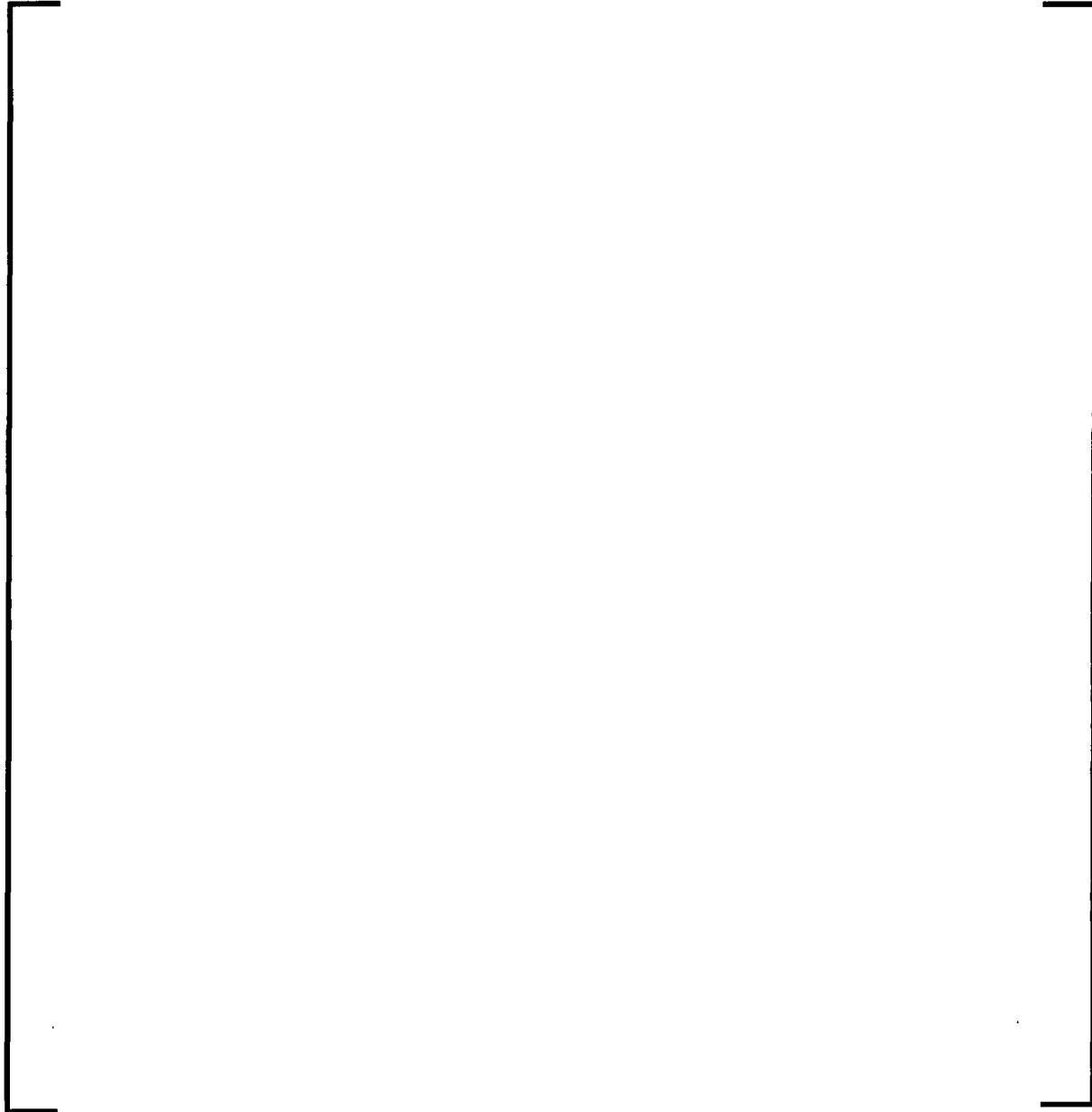
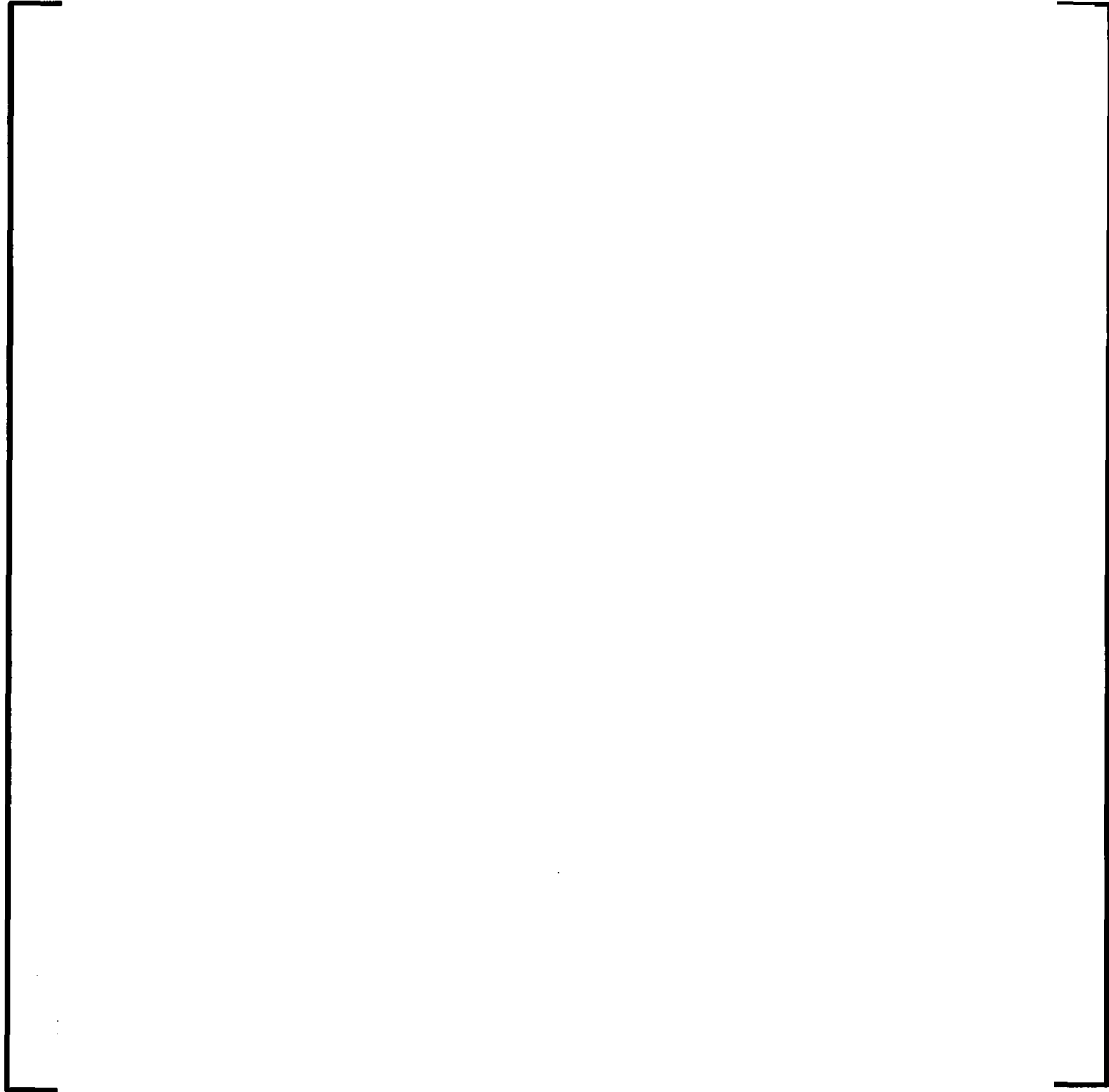
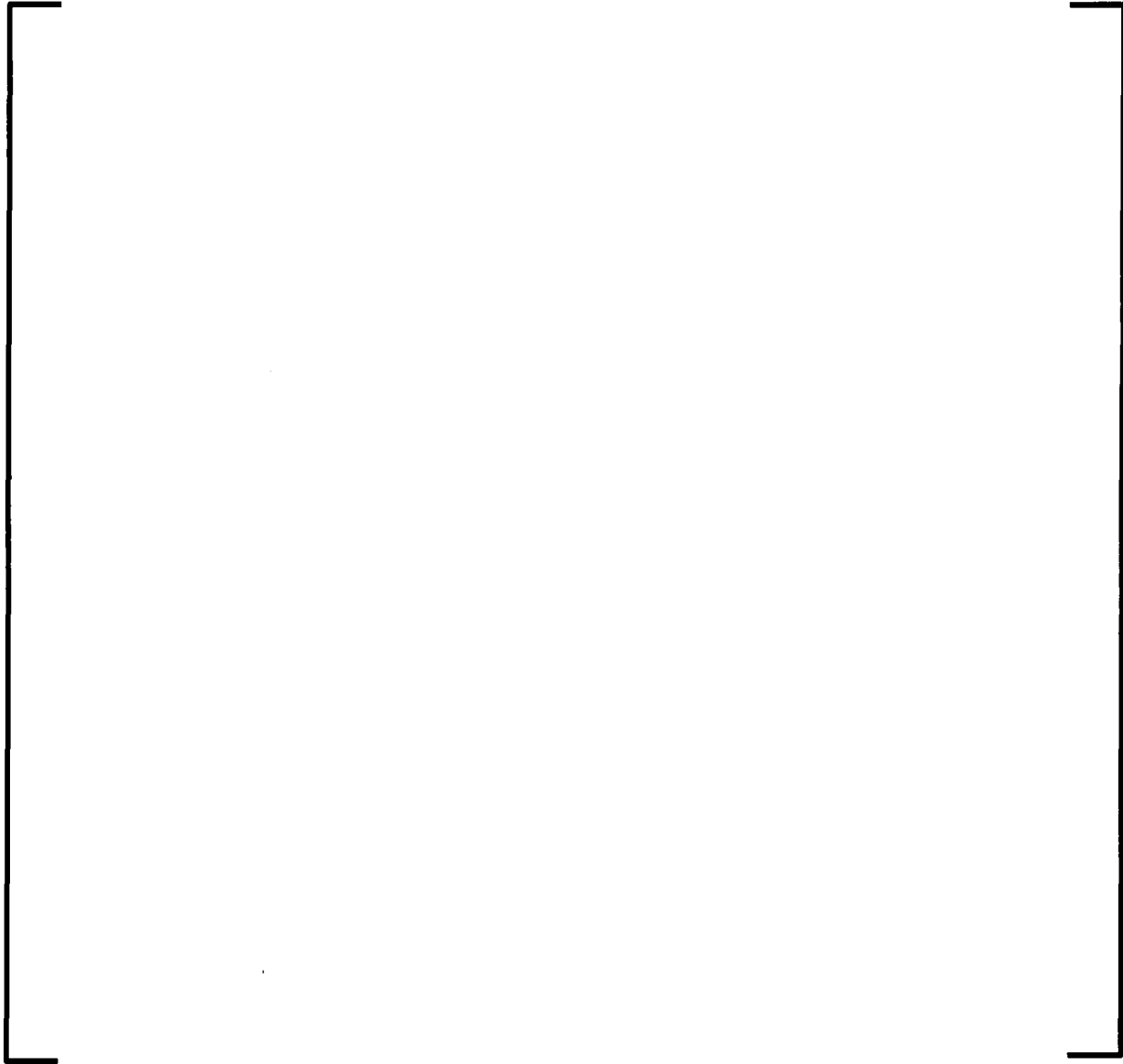
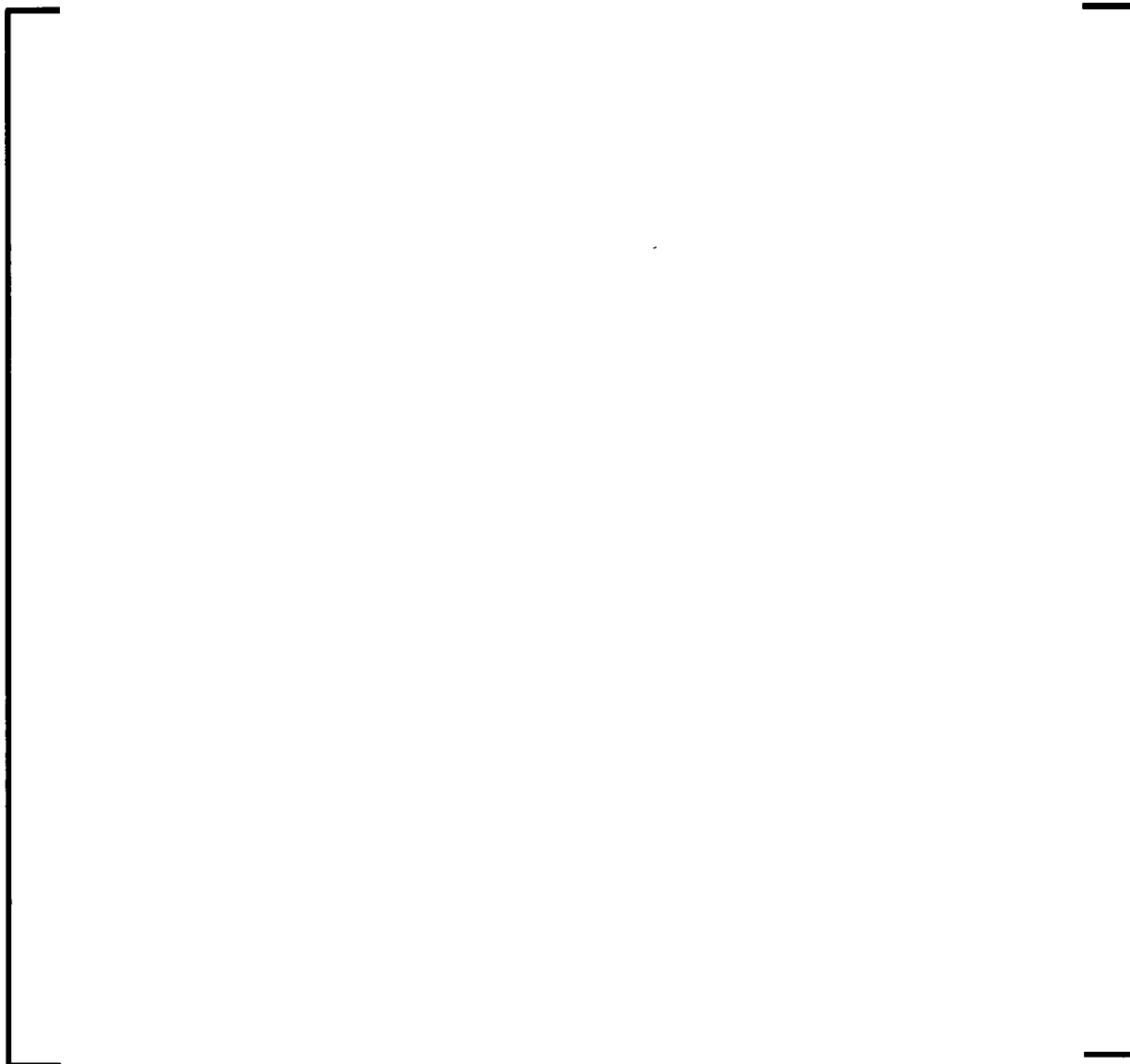


Figure A-18—U.S. EPR Spacer Grid B30122 – Uniform Deformation at Allowable Deformation Limit



**Figure A-19—U.S. EPR Spacer Grid B30121 – Envelope
Measurements**

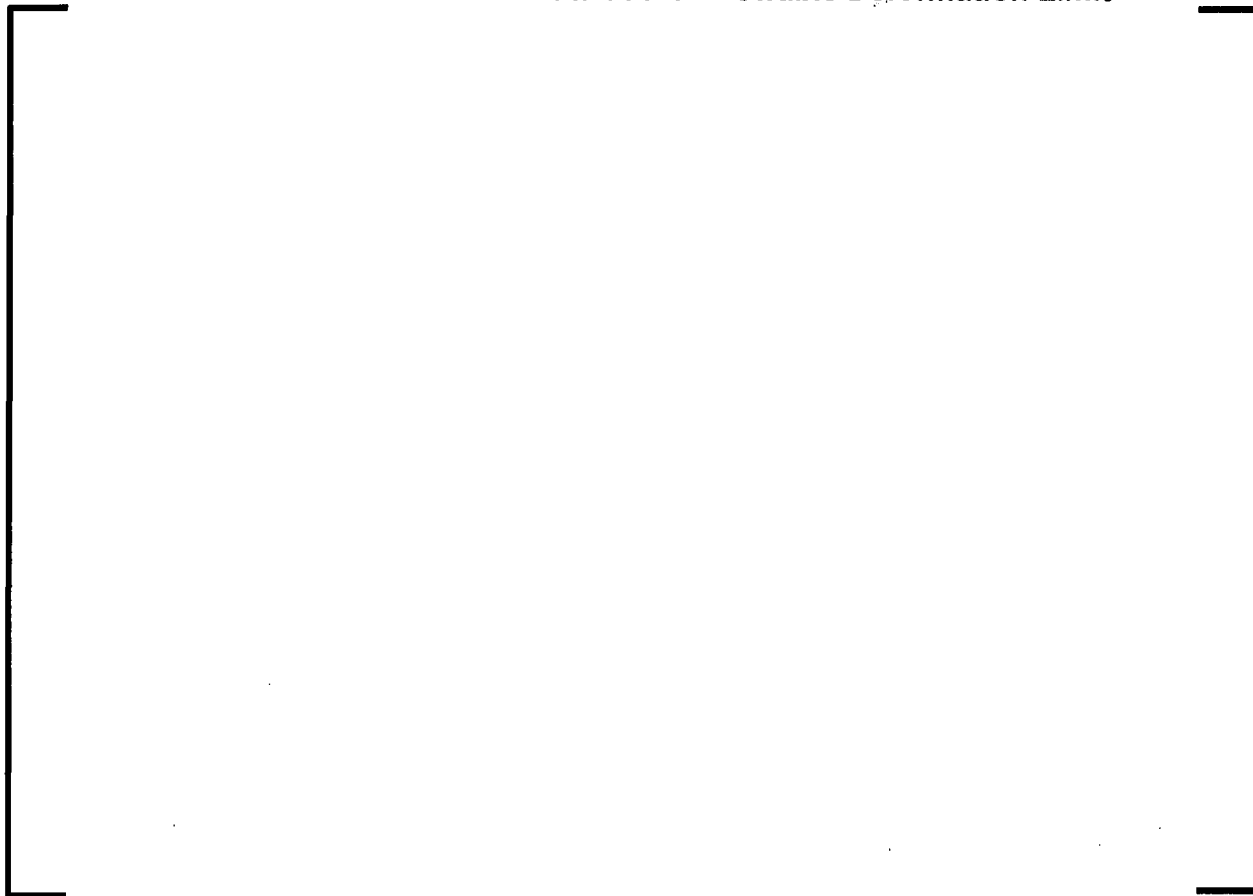


**Figure A-20—U.S. EPR Spacer Grid B30122 – Envelope
Measurements**

A more detailed geometric characterization was performed on grids B30121 and B30122 using a coordinate measuring machine (CMM). For these measurements, all fuel rod and guide tube segments were measured. The results of the measurements can be used to confirm the uniformity of the compressive deformation mode. The CMM measurements report the centerline position of each cladding segment at the centerline of the spacer grid. Given the large amount of data, the best method to demonstrate the

deformation mode is the average change in pitch for each grid row. First, the distance, or pitch, between adjacent cells is calculated based on the coordinate data. The distances are calculated in both the <x> and <y> direction. Again, the <y> direction is aligned with the impact direction. For the impact direction, between Row 1 and Row 2, the 17 cell-to-cell distances are averaged and compared to the theoretical pitch of [.]. The same values are compared between the other rows (e.g., Row 2 and 3, Row 3 and 4). Figure A-21 and Figure A-22 plot the average pitch change and the cumulative pitch change for each grid. The effective pitch change is the overall grid deformation divided by 17.

Figure A-21—U.S. EPR Spacer Grid B30121 – Cumulative and Individual Fuel Rod Pitch Data at the Allowable Deformation Limit



From Figure A-21 and Figure A-22, it is clear that the total deformation of [] is a result of a uniform compression of the grid. If a particular row had a pronounced racking deformation, the effect would be a significant departure from the effective average pitch, and the cumulative change would increase sharply between two rows, and represent a significant proportion of the overall grid deformation.

In the direction perpendicular to the impact direction, the absence of a shear racking mode is apparent from the envelope inspections and the guide tube position measurements.

Figure A-22—U.S. EPR Spacer Grid B30122 – Cumulative and Individual Fuel Rod Pitch Data at the Allowable Deformation Limit



A.4 U.S. EPR HTP Spacer Grid – Control Rod Insertability

This section discusses the details regarding the control rod insertability with the spacer grids deformed at the allowable crushing load in the unirradiated condition, and provides details in support of the general conclusions listed in Section 4.1.4.1.4.1.

Test of two of the [] HTP spacer grids (serial numbers B30121, and B30122) used for the allowable crush load testing were stopped after [] permanent deformation. The grids were geometrically inspected to establish:

- General envelope before and after the test.
- Guide tube pattern before and after the test.
- Fuel rod (all fuel rod cells) pitch before and after the test.

As part of the original work scope, the position of each guide tube segment was measured before and after the dynamic crush test. Two guide tubes formed the reference orientation in both the before and after test measurements. Figure A-24 and Figure A-25 plot the basic position of the guide tubes and the measured displacement of the guide tubes. The displacements are scaled by a factor of 10 to aid visualization. The measured displacements are also listed in Table A-1 and Table A-2.

The deformation mode for both grids was compressive in general. Spacer B30122 had very small shear displacements (in the lateral direction in Figure A-24 and Figure A-25) of less than []. The spacer B30121 had a more systematic shear deformation, but the deformation mode is not considered as a “shear racking” mode. The reason is that the shear deformation is progressive across the spacer grid, rather than a sudden accumulation of shearing. Even with a more pronounced shear deformation, the shear displacements were less than []. If the total deformation of the guide tube is considered (specifically the resultant of the two measured direction), both spacer grids have similar maximum guide tube displacements of [] for spacers B30121 and B30122, respectively.

Considering a guide tube inner diameter of [], the maximum radial clearance between the guide tube and the rod cluster control assembly rod is [] for the [] control rod (according to the schematic shown in Figure A-23).

In conclusion, a small radial clearance is maintained between the control rod and inner guide tube diameter, even at grid deformation levels in excess of the allowable crushing load limiting deformation (according to Figure A-19 and Figure A-20, the grid deformation was []). No effect is expected on control rod friction because of the extremely small guide tube pitch change from U.S. EPR HTP spacer grid accident loads, and therefore, no effect on control rod drop times.

Figure A-23—U.S. EPR Control Rod to Guide Tube Clearance – Grid Deformed to Allowable Crushing Load at BOL



Figure A-24—Guide Tube Displacements - Spacer B30121

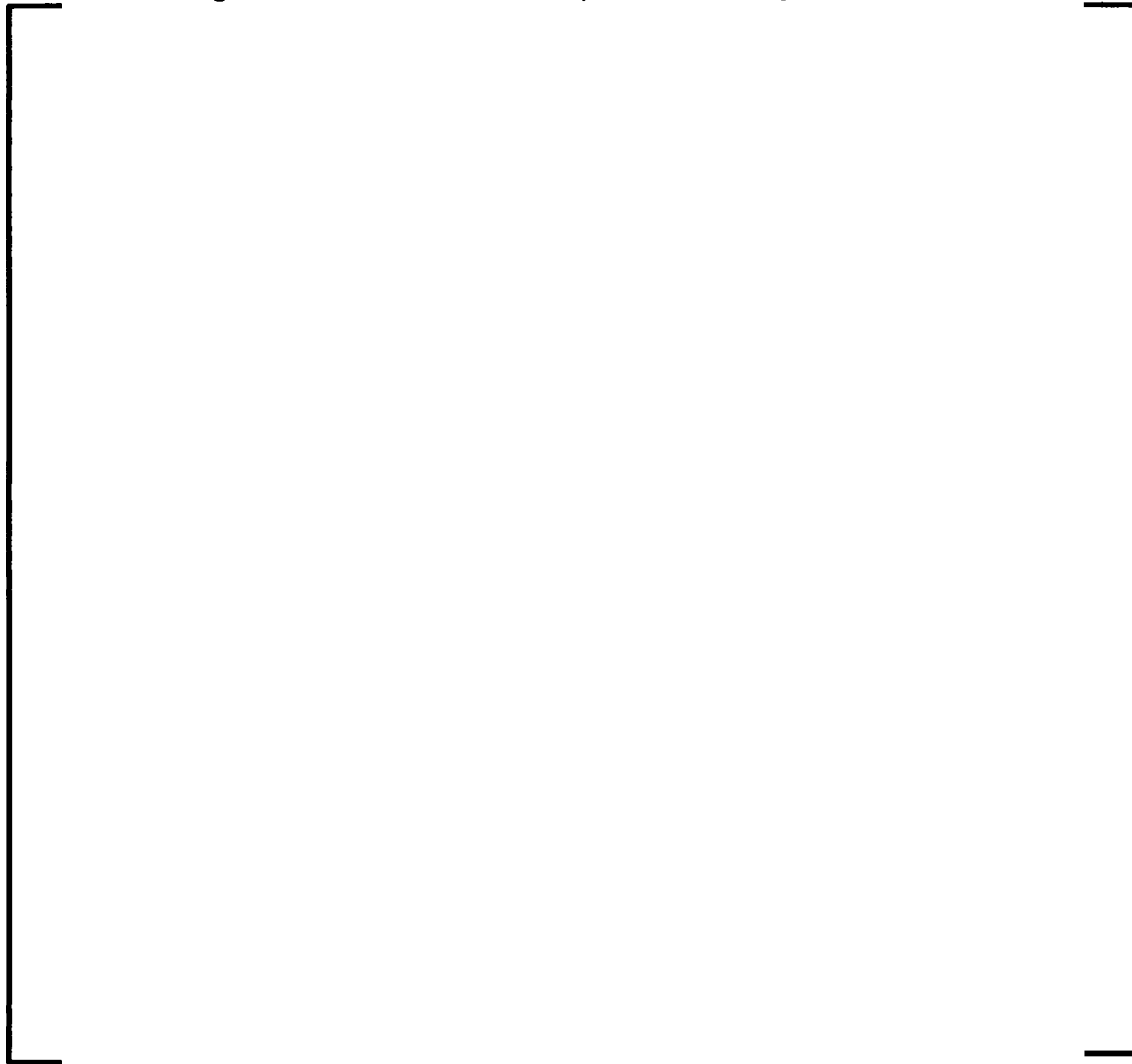


Figure A-25—Guide Tube Displacements - Spacer B30122



Table A-1—Guide Tube Displacements - Spacer B30121

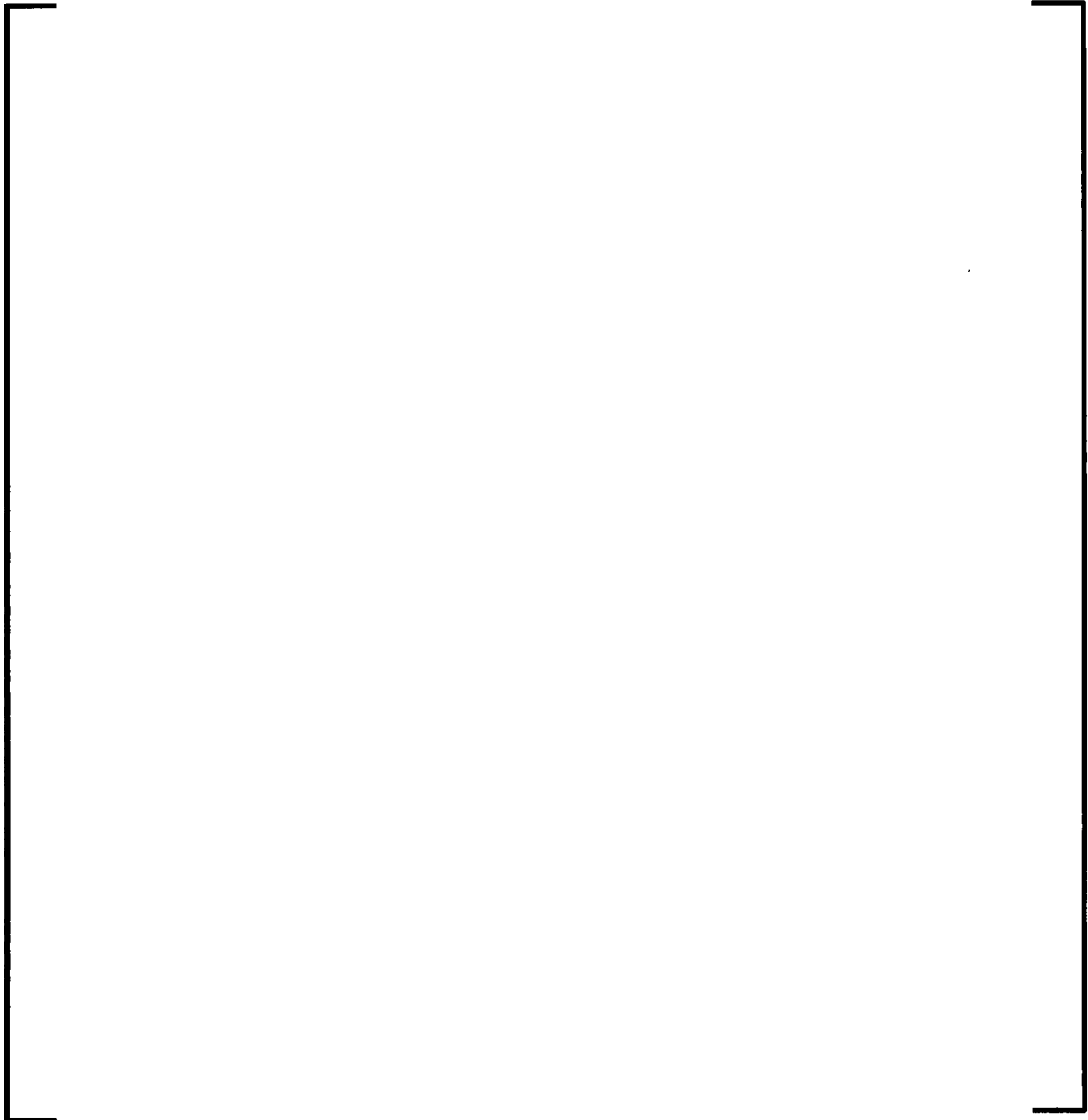
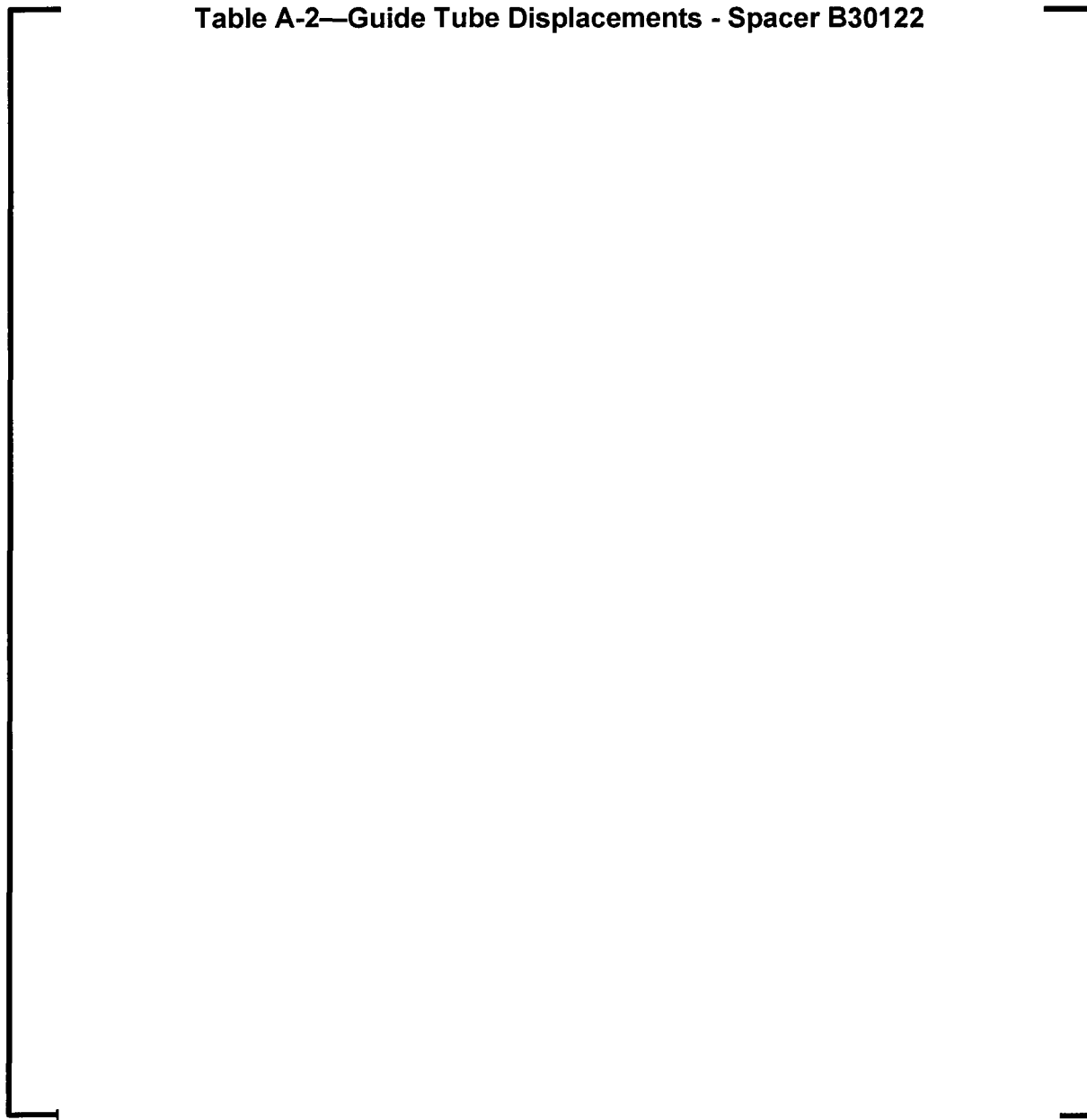
A large, empty rectangular frame with a thin black border, centered on the page. It is intended to contain the data for Table A-1, but the content is missing.

Table A-2—Guide Tube Displacements - Spacer B30122



**A.5 U.S. EPR HTP Spacer Grid – Simulated Irradiated Condition –
Comparative Grid Testing**

This section provides additional details to the discussion concerning the comparison of in-reactor irradiated spacer grid tests to the simulated irradiated condition test results in

Figure 4-32, Section 4.1.4.1.6. In that discussion, the conclusion was that the simulated irradiated test protocol produces a grid strength that follows sufficiently close to the in-reactor irradiated spacer grid strength data. A question can be raised about the variability of the in-reactor irradiated data, and the validity of the comparison with the simulated irradiated condition. This section answers this question by clarifying the source of the perceived variability of the in-reactor irradiated grid data.

For this purpose, the data in Figure 4-32 are re-plotted with more details included, in Figure A-26.

The in-reactor irradiated grid data, which are represented by green or blue squares, are plotted with the [] of the individual grid. The simulated irradiated condition grids are plotted with red triangles. It is important to note that the simulated irradiated condition grids were [

], which would correspond to the cluster of red triangle data points located on the left hand side of the plot (encircled in Figure 4-32).

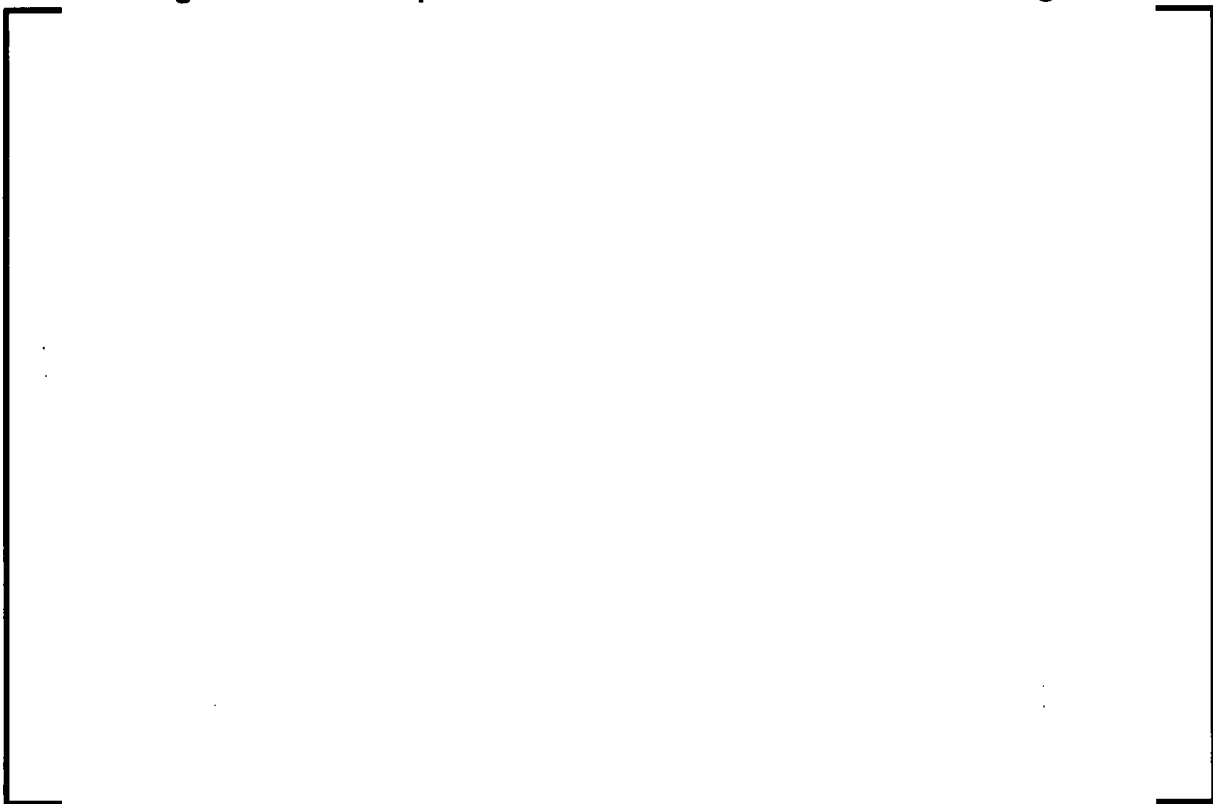
Upon examination, it is apparent that the [

]. However, the limiting grid impact loads occur in the middle of the bundle (positions 3 and above), and for these locations, the simulated fully relaxed data set constitutes a lower bound.

This corroborates the discussion on the effect of [

].

Figure A-26—Comparison of In-Reactor Irradiated Grid Strength



A.6 U.S. EPR HTP Spacer Grid – Stability under Repeated Impacts

This section provides additional details to the discussion concerning the grid stability under repeated impacts in Section 4.1.4.3.

The standard grid test protocol involves a series of impacts of monotonically increasing kinetic energy, which produce an incremental permanent deformation and a peak impact force that increases with the impact kinetic energy. The incremental permanent

deformation is an increasing function of the impact kinetic energy, while the peak impact load is proportional to the square root of the input kinetic energy. To support the use of this protocol, the effect of repeated impacts should be assessed. If each impact results in an incremental increase in deformation, then a large number of repeated impacts (even if the impacts were below the allowable limit) could increase cumulative deformation to unacceptable levels. This issue surfaced in one of the NRC public meetings during the U.S. EPR design certification process.

This section answers this question, by describing the results and conclusions from a group of tests involving different, non-standard impact loading sequences. The data

[

], using the standard test equipment described in

Section A.2. . The test hardware was manufactured through AREVA's Quality System.

The following non-standard protocol tests were performed in October 2012 on a group of [] grid strip thickness of the same design to those used for allowable crushing load testing (Section 4.1.4.1.4.2, and 4.1.4.1.6):

- [

]

• [

].

The comparison of the results from the standard protocol and the [] protocol offers a very good insight into the HTP grid behavior. Under monotonically increasing impacts the grid permanent deformation and the peak impact load increases with the impact kinetic energy (represented by red squares in Figure A-27). In addition, under this protocol, the square of the peak impact load is a linear function of the impact kinetic energy (red squares in Figure A-28).

Under [

]

On the F^2 versus $(MV^2)/2$ plot in Figure A-28, the same behavior can be analyzed from an energy transfer point of view. Under the [

]

These observations formulated support several conclusions:

- The standard test protocol conditions the grid to respond with the highest peak impact load, and the highest cumulative permanent deformation for a given impact kinetic energy.

- [

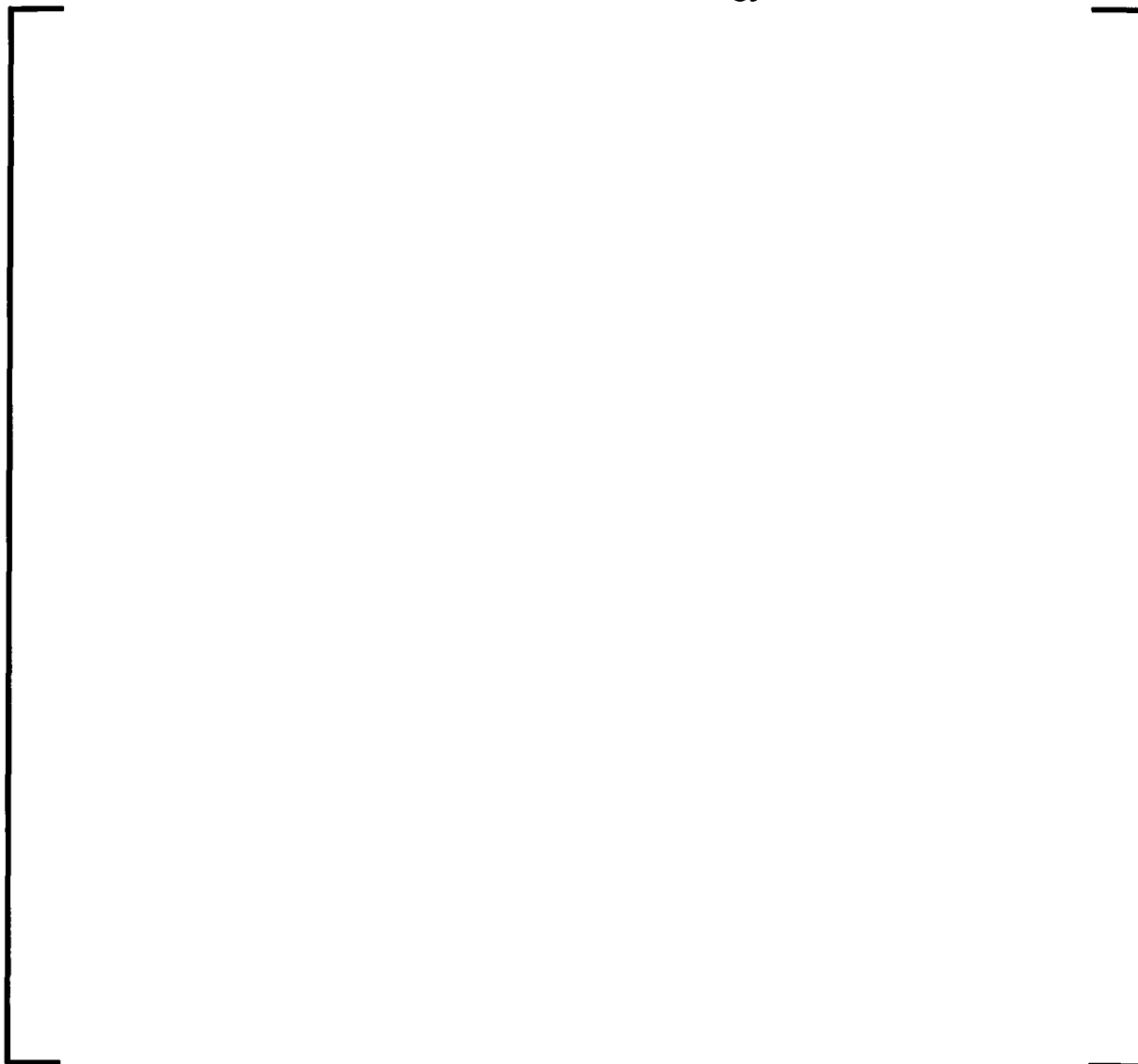
].

- The grid model stiffness benchmarked from the standard test protocol is higher, which will result in higher peak impact loads predicted by the grid element.

Therefore, the standard grid test protocol is doubly conservative. [

]

Figure A-28—HTP Grid Tests – Standard versus []
– F^2 versus Kinetic Energy



From the conclusions derived from the [

] This hypothesis was investigated through the [

]

First, the peak impact loads [

]

It is worth mentioning that the ascending impact test protocol represents a long-standing industry practice.

Another important conclusion supported by the [

] In Section 4.1.4.1 it was pointed out that the true limiting behavior of a spacer grid under impact is when the accumulated permanent deformation begins to interfere with the capability of the flow sub-channel to ensure coolability. The plot in Figure A-30 presents the loading curves for the [

] This shows that the margin derived with the methodology in Section 4.1.4.1 is conservative.

The test for the simulated irradiated condition was an ascending protocol, [

]

**Figure A-29—HTP Grid – [] Test – Loading History
and Cumulative Permanent Deformation**

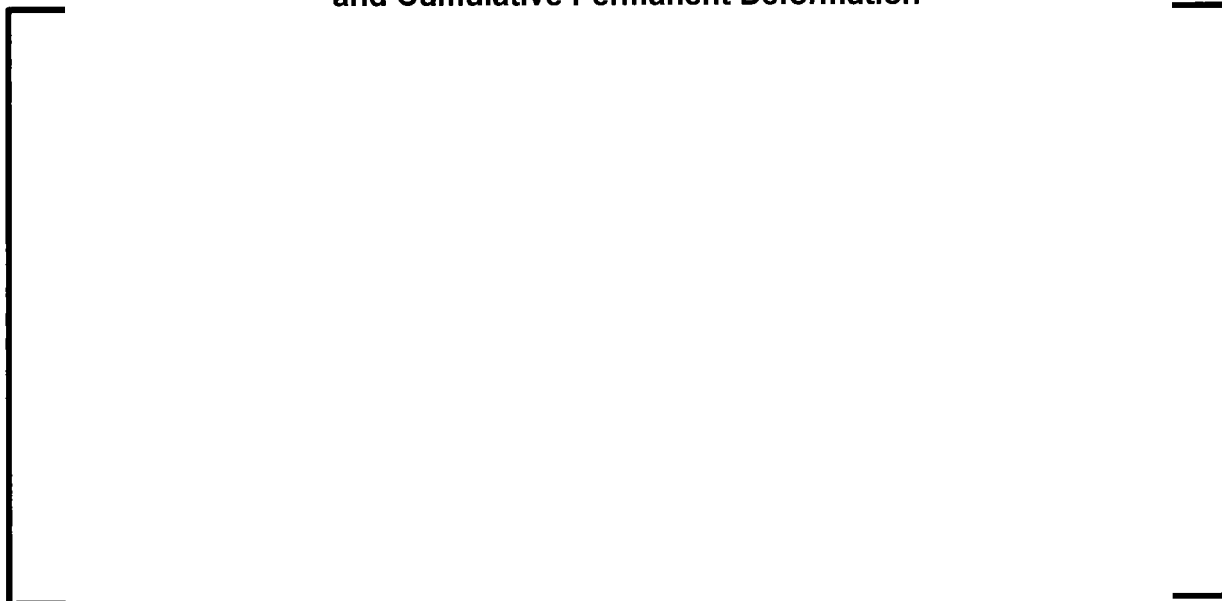


**Figure A-30—HTP Grid – Load versus Deformation Margin
Comparison**



**Figure A-31—HTP Grid Simulated Irradiated Condition – Standard
Protocol versus [] Test**



A.7 References

1. U.S. Nuclear Regulatory Commission, Information Notice 2012-09, "Irradiation Effects on Fuel Assembly Spacer Grid Crush Strength," Available in the NRC ADAMS - Accession Number ML113470490.
2. Framatome ANP, Inc., Closure of Interim Report 02-002, "Spacer Grid Crush Strength - Effects of Irradiation," August 8, 2003, Available in the NRC ADAMS - Accession Number ML032240425.

**Appendix B:
U.S. EPR Seismic and LOCA Loads – Lateral Displacement Input Time
Histories**

This appendix contains the plots of all the seismic and LOCA lateral loading time histories used in the U.S. EPR faulted analysis. Each time history was generated for the BOL and EOL cases.

B.1 BOL Case Seismic and LOCA Lateral Time Histories

Figure B-1—Lateral BOL Seismic Loading – Soil Case 1n2u



Figure B-2—Lateral BOL Seismic Loading – Soil Case 1n5a



Figure B-3—Lateral BOL Seismic Loading – Soil Case 2sn4u



Figure B-4—Lateral BOL Seismic Loading – Soil Case 4u



Figure B-5—Lateral BOL Seismic Loading – Soil Case 5a



Figure B-6—Lateral BOL Seismic Loading – Soil Case bblb



Figure B-7—Lateral BOL Seismic Loading – Soil Case bbub



Figure B-8—Lateral BOL Seismic Loading – Soil Case bbub-cr

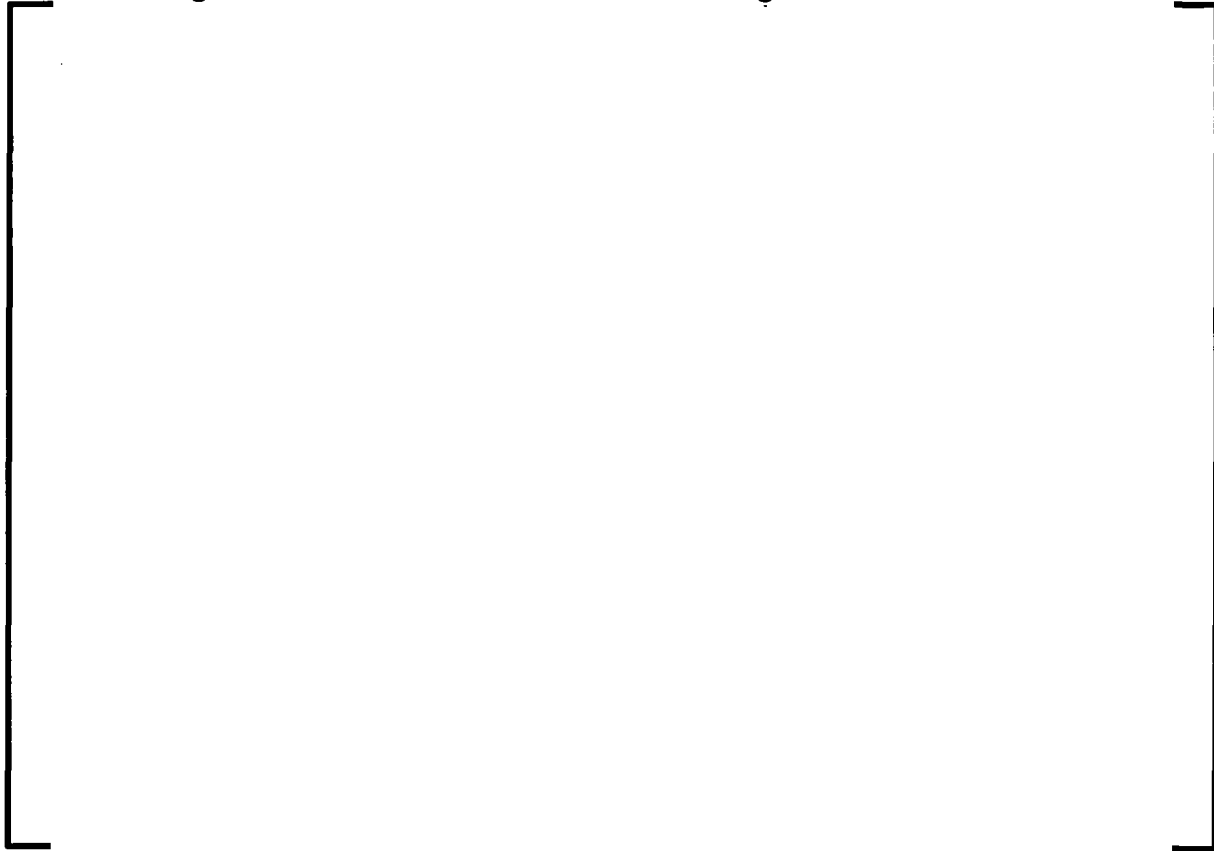


Figure B-9—Lateral BOL LOCA Loading – Case HELB-0HL



Figure B-10—Lateral BOL LOCA Loading – Case HELB-100CL



B.2 EOL Case Seismic and LOCA Lateral Time Histories

Figure B-11—Lateral EOL Seismic Loading – Soil Case 1n2u



Figure B-12—Lateral EOL Seismic Loading – Soil Case 1n5a

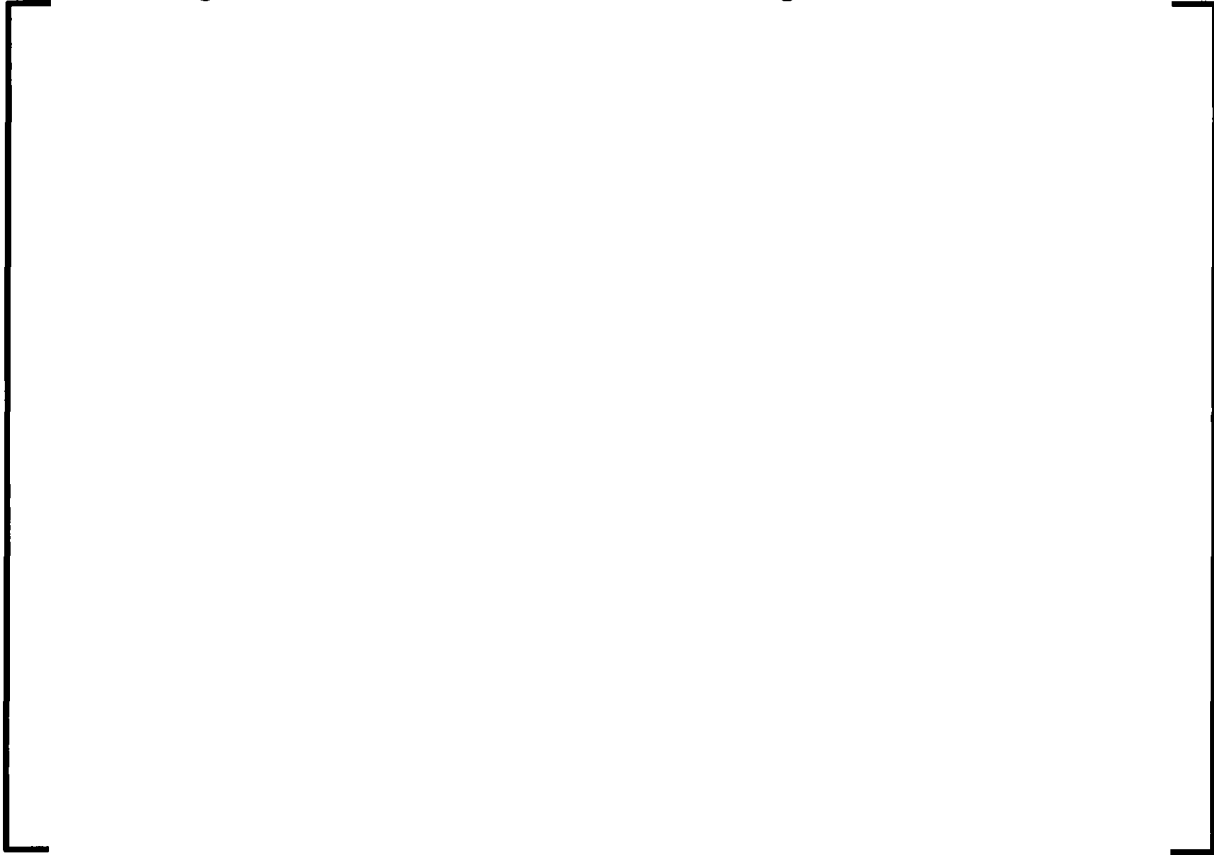


Figure B-13—Lateral EOL Seismic Loading – Soil Case 2sn4u

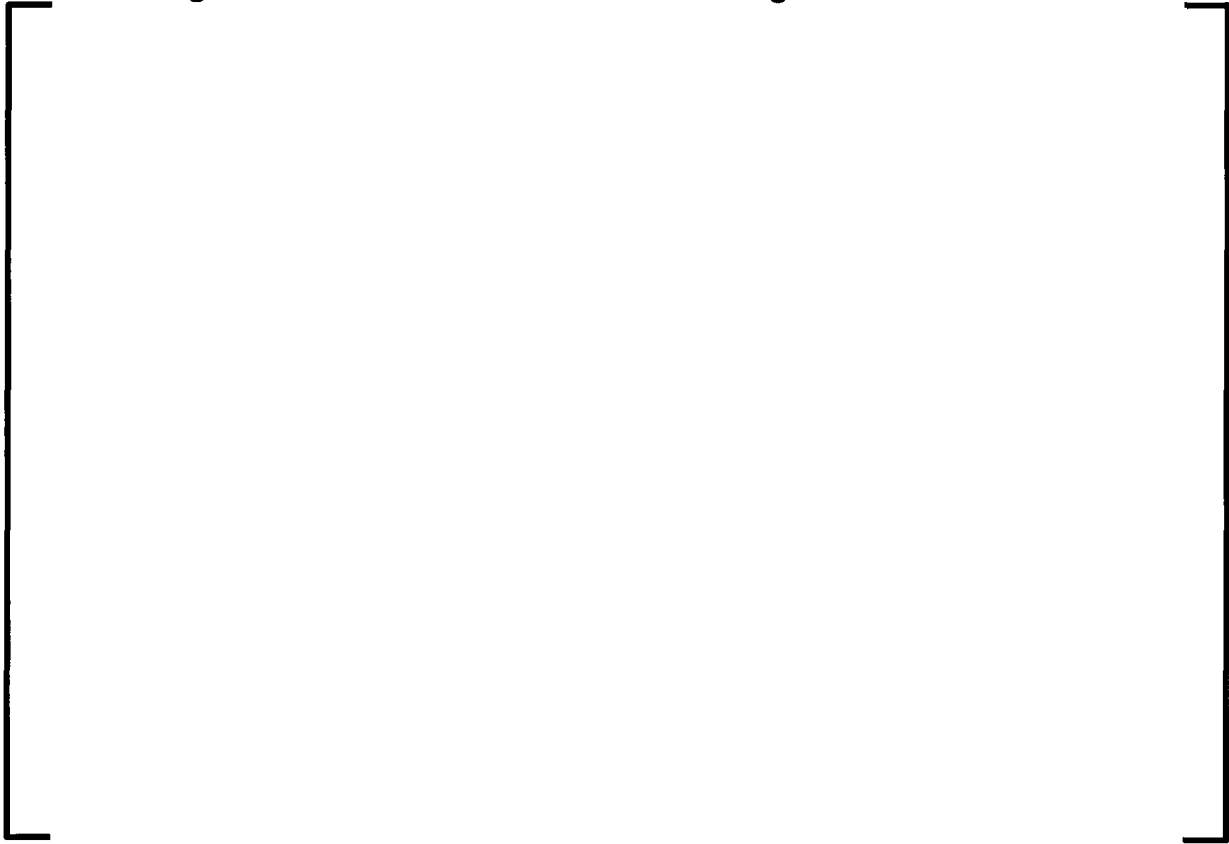


Figure B-14—Lateral EOL Seismic Loading – Soil Case 4u



Figure B-15—Lateral EOL Seismic Loading – Soil Case 5a



Figure B-16—Lateral EOL Seismic Loading – Soil Case bblb

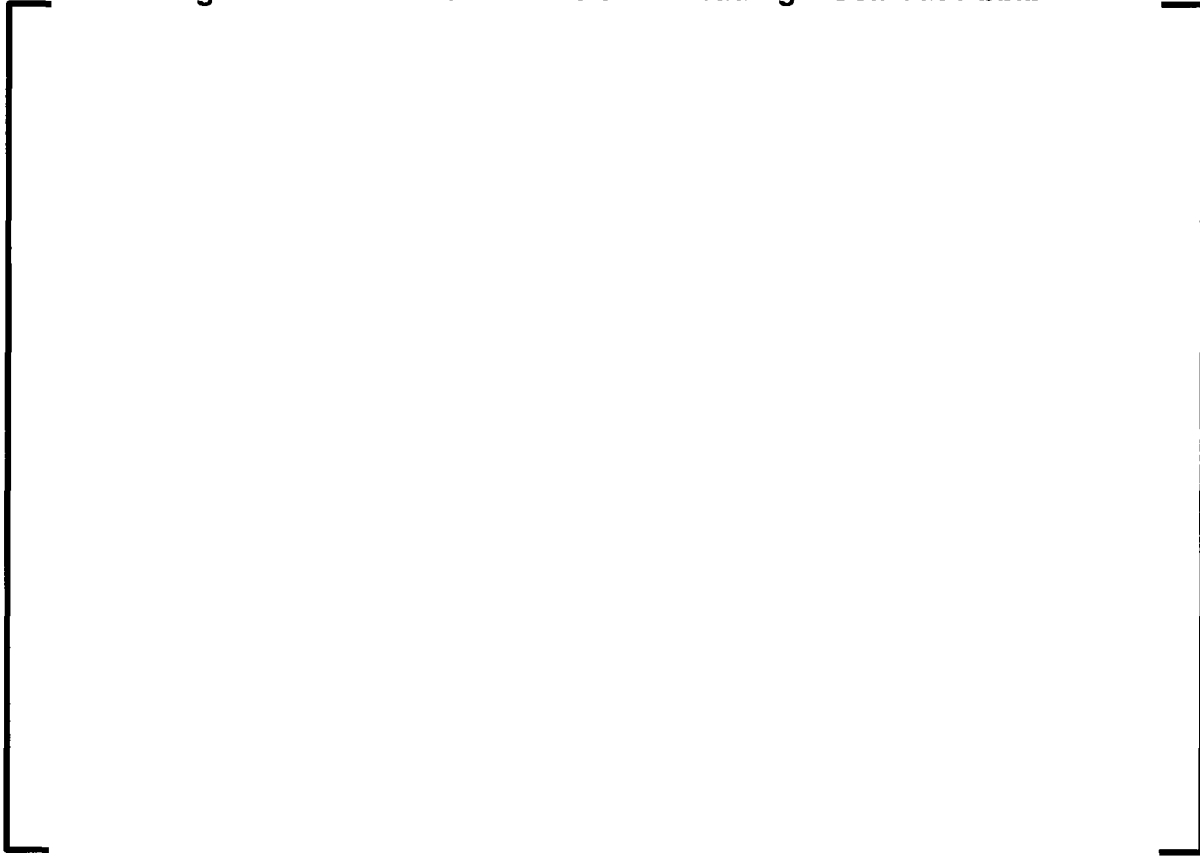


Figure B-17—Lateral EOL Seismic Loading – Soil Case bbub



Figure B-18—Lateral EOL Seismic Loading – Soil Case bbub-cr



Figure B-19—Lateral EOL LOCA Loading – Case HELB-0HL



Figure B-20—Lateral EOL LOCA Loading – Case HELB-100CL

